Three–dimensional inversion of transient electromagnetic data: A comparative study

INAUGURAL – DISSERTATION
ZUR
ERLANGUNG DES DOKTORGRADES
DER MATHEMATISCH–NATURWISSENSCHAFTLICHEN FAKULTÄT
DER UNIVERSITÄT ZU KÖLN

VORGELEGT VON
MICHAEL COMMER
AUS BONN

KÖLN 2003

Berichterstatter: Prof. Dr. B. Tezkan
Prof. Dr. K. Spitzer

Tag der mündlichen Prüfung: 12.12.2003

ABSTRACT

Inversion of transient electromagnetic (TEM) data arising from galvanic types of sources is approached by two different methods. Both methods reconstruct the subsurface three–dimensional (3D) electrical conductivity properties directly in the time–domain. A principal difference is given by the scale of the inversion problems to be solved. The first approach represents a small–scale 3D inversion and is based upon well–known tools. It uses a stabilized unconstrained least–squares inversion algorithm in combination with an existing 3D forward modeling solver and is customized to invert for 3D earth models with a limited model complexity. The limitation to only as many model unknowns as typical for classical least–squares problems involves arbitrary and rather unconventional types of model parameters.

The inversion scheme has mainly been developed for the purpose of refining a priori known 3D underground structures by means of an inversion. Therefore, a priori information is an important requirement to design a model such that its limited degrees of freedom describe the structures of interest. The inversion is successfully applied to data from a long–offset TEM survey at the active volcano Merapi in Central Java (Indonesia). Despite the restriction of a low model complexity, the scheme offers some versatility as it can be adapted easily to various kinds of model structures. The interpretation of the resistivity images obtained by the inversion have substantially advanced the structural knowledge about the volcano.

The second part of this work presents a theoretically more elaborate scheme. It employs imaging techniques originally developed for seismic wavefields. Large–scale 3D problems arising from the inversion for finely parameterized and arbitrarily complicated earth models are addressed by the method. The algorithm uses a conjugate–gradient search for the minimum of an error functional, where the gradient information is obtained via migration or backpropagation of the differences between the data observations and predictions back into the model in reverse time. Treatment for electric field and time derivative of the magnetic field data is given for the specification of the cost functional gradients. The inversion algorithm is successfully applied to a synthetic TEM data set over a conductive anomaly embedded in a half–space. The example involves a total number of more than 376000 model unknowns.

The realization of migration techniques for diffusive EM fields involves the backpropagation of a residual field. The residual field excitation originates from the actual receiver positions and is continued during the simulated time range of the measurements. An explicit finite–difference time–stepping scheme is developed in advance of the imaging scheme in order to accomplish both the forward simulation and backpropagation of 3D EM fields. The solution uses a staggered grid and a modified version of the DuFort–Frankel stabilization method and is capable of simulating non–causal fields due to galvanic types of sources. Its parallel implementation allows for reasonable computation times, which are inherently high for explicit time–stepping schemes.

ZUSAMMENFASSUNG

Im Rahmen dieser Arbeit werden zwei Verfahren für die Inversion von transient–elektromagnetischen (TEM) Daten von galvanisch gekoppelten Quellen vorgestellt. Beide Methoden rekonstruieren die dreidimensionale (3D) Leitfähigkeitsstruktur des Untergrundes im Zeitbereich. Ein wesentlicher Unterschied ist durch die Größenordnung des jeweiligen Inversionsproblems gegeben. Der erste Ansatz löst kleinskalige Inversionsprobleme und basiert auf bekannten Methoden. Die Rekonstruktion von 3D Modellen mit beschränkter Komplexität wird durch die Kombination des Marquardt–Inversionsverfahrens mit einem existierenden 3D Simulationsalgorithmus für EM Felder verwirklicht. Das Verfahren ist auf solche Anzahlen von Modellparametern beschränkt, die typisch für klassische “least–squares” Probleme sind. Daher werden eher untypische Arten von Modellparametern eingesetzt, um 3D Strukturen zu beschreiben.

Das Verfahren ist hauptsächlich dafür geeignet, das Modell einer im Vorfeld grob bekannten Untergrundstruktur durch eine Inversion zu verfeinern. Daher sind Vorinformationen eine wesentliche Voraussetzung. Sie werden herangezogen, damit die in ihrer Anzahl beschränkten Modellparameter so gewählt werden können, dass die interessierenden Strukturen abgedeckt werden. Die Inversionsmethode wird erfolgreich auf Daten einer LOTEM Messung am aktiven Vulkan Merapi (Zentral–Java, Indonesien) angewandt. Trotz der eingeschränkten Modellkomplexität in der Inversion bietet die Methode ein gewisses Maß an Flexibilität. Die Modellparametrisierung kann leicht an verschiedene Untergrundstrukturen angepasst werden. Die Interpretation der Inversionsergebnisse hat wesentlich zum Wissen über die Verteilung der Leitfähigkeit am Merapi beigetragen.

Der zweite Teil dieser Arbeit stellt ein aus theoretischer Sicht anspruchsvolles Verfahren vor. Es benutzt Techniken, die ursprünglich zur Migration seismischer Daten verwendet wurden. Die Methode ist geeignet zur Lösung großskaliger Inversionsprobleme, die durch komplizierte Modelle mit großer Parameteranzahl entstehen. Der Algorithmus verwendet das Verfahren der konjugierten Gradienten zur Minimierung eines Fehlerfunktionals. Die Gradienten ergeben sich durch Migration der Residuen von gemessenen und durch Modellannahme berechneten Daten. Ähnlich wie bei der seismischen Migration bewegen sich die Residuenfelder zeitlich rückwärts. Ihre erste Anregung erfolgt zum Zeitpunkt der spätesten Daten und wird bis zum frühesten Meßpunkt simuliert. Daten von elekrischen Feldern und zeitlicher Ableitung von Magnetfeldern werden in der Herleitung der Gradienten behandelt. Das Verfahren wird erfolgreich auf einen synthetischen Datensatz angewandt. Dabei wird eine blockförmige Leitfähigkeitsanomalie in einem homogenen Halbraum rekonstruiert. Das Beispiel beinhaltet die Lösung eines Inversionsproblems mit mehr als 376000 Unbekannten.

Die Anregung der Residuenfelder erfolgt an den Empfängerpunkten und setzt sich während ihrer Simulation fort. Für die Felder der Vorwärtssimulation und der Migration wird ein explizites Zeitschrittverfahren speziell für galvanische Sendertypen entwickelt. Die 3D Simulation beruht auf einer räumlichen Diskretisierung der Maxwell Gleichungen, die unter dem Namen ”staggered grid” bekannt ist. Außerdem wird die sogenannte DuFort–Frankel Stabilisierungsmethode benutzt. Explizite Zeitschrittverfahren zeichnen sich durch einen hohen Rechenzeitbedarf aus. Daher wird der Simulationsalgorithmus für Parallelrechner entwickelt.

Contents

List of Figures

List of Tables

CHAPTER 1

INTRODUCTION

Transient electromagnetic (TEM) methods are made to determine the electrical and properties of the earth. The methods have a well–established place in exploration geophysics, because they have the potential to provide very useful additional information for problems associated for example with mineral exploration [*Sarma et al.*, 1976; *Palacky*, 1983; *Helwig et al.*, 1994], oil exploration [*Spies*, 1983; *Strack et al.*, 1989], volcanological hazards [*Kauahikaua et al.*, 1986; *Lienert*, 1991; *Jones and Dumas*, 1993] and hydrological investigations [*Stewart*, 1982; *Mills et al.*, 1988]. An excellent review of the TEM method and its uses is given by *Nabighian and Macnae* [1991]. A collection of related publications can be found in the special TEM issue of *Geophysics*, Vol. 49 (7), 1984.

In the field of environmental geophysics, with shallow exploration depths, TEM methods have become increasingly popular [*Frischknecht et al.*, 1991]. Shallow exploration typically involves systems that employ loops as transmitting antennas with an inductive coupling to the ground. A fundamental description of the physical basis for the TEM sounding technique, with particular attention paid to a configuration where a magnetic receiver coil is located at the center of the transmitter loop (in–loop array), is given by *Fitterman and Stewart* [1986]. Loop transmitters can be deployed rapidly and more easily than grounded wires. Although the grounded wire is a more complex source, it is often used in deep soundings, because the field falls off less rapidly at large distances and generation of adequate field levels is difficult with loop sources [*Spies and Frischknecht*, 1991]. The presented work focuses on grounded–wire transmitters, which have a galvanic coupling to the ground and involve the presence of non–causal source fields. The long–offset TEM (LOTEM) technique [*Petry*, 1987; *Strack*, 1992] typically uses a long grounded wire for deep crustal studies [*de Beer et al.*, 1991; *Thern et al.*, 1996; *Hördt et al.*, 2000*b*] and has been continuously developed at the Institute for Geophysics and Meteorology of the University of Cologne.

In general, data quality and quantity arising from TEM surveys have tended to increase together with computational capabilities. Therefore, routine interpretation is likely to become multi–dimensional in character. This is important in order to enable multi–disciplinary interpretation approaches as a means to achieve earth models with minimum ambiguity in the future. However, the interpretation of TEM data containing effects from multi–dimensional conductivity structures is still non–trivial. First, TEM systems employ artificial sources, which is rather complicated to simulate due to finite source sizes and generation of fields that vary in three dimensions. Second, the solution of multi–dimensional inverse problems is usually large in scale. If arbitrarily complex earth models are taken into account, the number of model unknowns may amount to as much as several tens or hundreds of thousands in real exploration problems.

Therefore, the routine interpretation of TEM data is still based on one–dimensional (1D) earth models (e.g. *Macnae and Lamontagne* [1987]; *Nekut* [1987]; *Eaton and Hohmann* [1989]). In a 1D inversion (e.g. *Anderson* [1982]; *Raiche et al.* [1985]; *Huang and Palacky* [1991]), a least–squares problem is solved for a conductivity–versus–depth profile of a layered earth model. Different ways of parameterizing a 1D earth exist. For the interpretation of data generated by loop sources *Fullagar and Oldenburg* [1984] and *Farquarson and Oldenburg* [1993] use many more layers (with fixed thicknesses) than observations and thus solve an under–determined inverse problem. This greatly increases the non–uniqueness of the mathematical solution and thus requires imposing model smoothing constraints in order to generate a model that contains only as much structure as required to fit the data. The inversion for smooth models is also known as the Occam scheme [*Constable et al.*, 1987] and was applied to LOTEM data by *Commer* [1999]. If, on the other hand, an unconstrained over–determined least–squares problem is solved, one typically allows the variation of both resistivity and thickness of a very limited number of layers, perhaps half–a–dozen. This approach has the potential for generating a plausible representation of the underground, yet the result shows more dependence on the number of free parameters and the starting model. On the other hand, in contrast to smoothing constraints, an unconstrained model is more adequate to incorporate a priori information that may indicate a rich model structure.

In addition to the large–scale difficulties and the complicated 3D source fields, the lack of a sufficient amount of observations may also be a reason for restricting the variation of a model to one dimension. Although the high non–uniqueness problem of a large–scale 3D solution can be addressed by regularization, using smoothing constraints, it still requires an area–wide distribution of detectors above the target to guarantee a reasonable resolution. However, in many cases, only profiles of observations exist. Such situations suggest to image the lateral variation of the conductivity along the profile direction, in addition to the vertical variation, by means of 2D inversion schemes. At present 2D inversions of direct current (DC) and magnetotelluric (MT) data are common tools and are widely used, whereas the multi–dimensional inversion of TEM data has been developed slower, mainly due to the more difficult simulation of artificial sources. Because of the situation of a 3D source field in a 2D subsurface structure, such inversions for controlled–source methods are often referred to as 2.5D problems [*Hohmann*, 1988].

Recently, some progress in the solution of the 2.5D EM inverse problem for controlled source data has been made. *Torres-Verdin and Habashy* [1994] used the extended Born approximation for EM tomography. A 2.5D subspace inversion technique based on a finite–element (FE) forward modeling scheme was presented by *Unsworth and Oldenburg* [1995]. Its effectiveness was demonstrated by an application to sea–floor EM surveys. Using a fast integral equation (IE) forward modeling method, *Ellis* [1998] and *Chen et al.* [1998] demonstrated the advantage of 2.5D inversions in the interpretation of airborne EM data. *Lu et al.* [1999] developed a rapid relaxation inversion of controlled–source audio frequency magnetotelluric (CSAMT) data including the transition–field and near–field data, and *Unsworth et al.* [2000] applied this inversion to CSAMT data from a potential radioactive waste disposal site. *Mitsuhata et al.* [2002] transformed time–domain LOTEM data into the frequency domain and carried out a 2.5D linearized least–squares inversion with a smoothness constraint based upon Bayesian statistics.

The most realistic image of the Earth can be obtained if a model variation in all three Cartesian dimensions is allowed in an inversion. The development of 2D and 3D inversion schemes for controlled sources has been almost simultaneously, because both types employ 3D source fields. *Eaton* [1989] formulated an inversion procedure based on frequency–domain, volume integral equations and a pulse–basis representation for the internal electrical field. Using a Born approximation to the 3D IE, *Pellerin and Hohmann* [1993] iteratively refine a piece–wise 1D interpretation at a receiver using the data from neighbouring receivers. The EM inverse scattering problem associated with recovering a 3D conductivity model from airborne TEM data was solved by *Ellis* [1999], employing a fast IE forward modeling algorithm embedded in a regularized Gauss–Newton optimization driver. *Xie and Li* [1999] proposed an algorithm for 3D EM inversion that works with the magnetic–field IE, where both forward and inverse IE systems are discretized by the finite–element (FE) method. *Zhdanov et al.* [2002] introduced an adaption of the thin sheet method, based on an approximation of the conductivity cross–section by a set of conductive thin sheets with local inclusions.

This work presents two different 3D inversion approaches for time–domain EM data in a comparative study. The first scheme developed in Chapter 2 addresses the large–scale difficulty of full 3D inversion methods. Furthermore, it is optimized for the case when only a limited amount of field data is available for an inversion. The idea of the scheme is to apply an unconstrained least–squares inversion algorithm, usually employed for small–scale unconstrained 1D problems, to 3D problems. This implies a limitation to only as many model unknowns as typical for classical least–squares problems. Rather than defining a numerous set of cell–based unknowns given by a simulation grid's spatial discretization, as is the common approach in large–scale 3D inversions, the shape of larger volumes of constant conductivity is controlled by the model variables. Several different types of untypical model parameters will be shown in the course of Chapter 2. To allow a quick reference, the inversion scheme will also be referred to as SINV[1].

The constrained inversion scheme SINV has mainly been developed for the purpose of refining a priori known 3D underground structures by means of an inversion. Therefore, a priori information is an important requirement to design a model such that its limited degrees of freedom describe the structures of interest. Such prior information is often given by geologi-

---

[1] The strong constraints on the model complexity and the limited amount of field data to be inverted suggested to call the method a “Sparse INVersion”.

cal studies, borehole or other geophysical measurements. An example will be given by a case history from a LOTEM survey at a volcano. Both the mountain topography and lateral conductivity variations in the underground require to take 3D structures into account. Because of the mountainous terrain, the survey was made difficult by logistical problems. Therefore, a full large–scale approach is prohibited due to only a sparse distribution of the observations above the target. However, the inversion for "low–parameterized" models involves an over–determined problem and thus makes SINV a practicable tool for the data analysis.

The scheme is based on a stabilized iterative inversion scheme combined with an existing solution for the 3D forward simulation of EM fields. The widely used 3D modeling code developed by *Druskin and Knizhnerman* [1988] is employed. It has been used a number of times for the 3D simulation of LOTEM responses [*Hördt*, 1992; *Hördt et al.*, 2000*a*;*b*; *Hördt and Müller*, 2000]. The modeling algorithm is based on the spectral Lanczos decomposition method (SLDM) [*Druskin and Knizhnerman*, 1988; 1994]. The Maxwell equations are solved using Krylov subspace techniques which provides for a fast explicit 3D solver for the diffusion of EM fields in arbitrarily heterogeneous media. The modeling code will be referred to as SLDM code. Its implementation of a material averaging scheme supports the design of arbitrary model parameters. Both the fast 3D forward simulation and the small scale of the inversion problem lead to a relatively low computational effort. The computation time for an inversion is further minimized by distributing the multiple forward simulations during an iteration to several processors of a parallel computer.

In contrast to the constrained inversion scheme, the second part of this work presents a large–scale inversion approach. The scheme adapts an imaging method originally developed for seismic wavefields [*Claerbout*, 1971; *Loewenthal et al.*, 1976; *Tarantola*, 1984] and known as seismic migration to diffusive EM fields. An inversion formulation that applies migration techniques to EM data is not entirely new. *Zhdanov and Frenkel* [1983] have advanced the idea of migrating or backpropagating the scattered EM field into a homogeneous background medium in order to image the source of the scattering. *Lee and Xie* [1993] transformed low–frequency EM fields by an integral transformation into wavefields in order to apply seismic imaging methods. It was along these lines, *Wang et al.* [1994] developed the theory for solving the full non–linear 3D TEM inverse problem in the time–domain by an efficient way of a conjugate–gradient search for the minimum of an error functional. *Zhdanov and Portniaguine* [1997] introduced a new formulation of the time–domain electromagnetic migration technique, based on the minimization of the residual–field energy flow through a profile of observations.

The inversion algorithm presented in this work uses a non–linear conjugate–gradient search for the minimum of an error functional. While *Wang et al.* [1994] made much progress in proposing a tractable approach to 3D TEM imaging, they only applied their solution to 2D synthetic examples from causal sources. This involved the solution of the scalar wave equation for electric fields and neglected crucial details for implementing the technique for general 3D imaging. Here, the specifications of the cost functional gradients are formulated for the full 3D treatment of non–causal source fields arising from galvanic sources. It will become evident that the problem related to causal source fields is contained in the more general non–causal case.

The actual solution formulation of the inverse problem by means of migration techniques for diffusive EM fields is outlined in Chapter 4 and involves both forward simulation and backpropagation of the EM field. Therefore, the preceding Chapter 3 develops an adequate explicit finite–difference (FD) time–stepping scheme in order to enable the migration of EM fields, which cannot be realized by the SLDM code. It is in principle based on the FD time–domain solution for 3D modeling presented by *Wang and Hohmann* [1993]. However, mainly due to the involvement of 3D non–causal source fields, there are differences in several key aspects as will be outlined in more detail in Chapter 3. Moreover, the solution has been developed for parallel computing platforms.

Preliminary notes

For brevity, following *Goldman et al.* [1994], in all chapters the word voltage shall be used instead of both "magnetic field time derivative" or "magnetic induction time derivative". Although it may be argued that electric field measurements also effectively involve voltages, it will become clear from the context which kind of field is considered. Vectors and matrices will be represented by bold characters. Lower case characters are used for vectors, upper case letters are used for matrices.

This work treats EM fields generated by sources with a galvanic coupling to the underground. Such sources and its generated EM fields are also referred to as non–causal. This expression is chosen due to the presence of a DC electric and magnetic field in the underground before the source signal is generated by a shut–off. Inductive source types without comparable DC fields will be referred to as causal.

CHAPTER 2

A 3D CONSTRAINED INVERSION APPROACH AND ITS APPLICATION TO LOTEM DATA FROM MOUNTAINOUS TERRAIN

In the geophysical literature, a large number of examples can be found for data interpretation situations, which are characterized as follows:

1. The collected data are insufficient, in terms of the spatial covering of the target, in order to determine a numerous set of model unknowns in a large–scale inversion approach. This may have several reasons, where logistic and/or economic limitations might be dominant. In other cases, a survey may have the aim of a preliminary investigation of a target and thus involves only a limited amount of measurements.

2. There exists prior knowledge about the target. This can be given by other geophysical disciplines, geological information or borehole measurements. In many cases, TEM surveys are carried out on the basis of a priori information in order to refine the model of an a priori known target (e.g. *Taylor et al.* [1992]; *Hördt et al.* [2000*b*]).

3. Simplified 1D inversion approaches fail to take multi–dimensional effects contained in the data into account. Even if a data fit can be achieved, laterally biased interpretations can be expected when 1D methods are applied to the response of more complex structures. Examples where 1D inversions do not accurately recover 2D or 3D resistivtiy distributions are shown by *Newman et al.* [1987] and *Blohm et al.* [1991].

Without regard to the complexity of the underground, 1D inversion routines are often employed, because of the computational expense of a full 3D inversion and the current lack of available inversion codes for TEM measurements. Even with the capability of inverting for a large parameter set, the poor resolution due to insufficient data remains. Multi–dimensional forward modeling is often used alternatively (e.g. *Hördt et al.* [1992]; *Helwig et al.* [1994]). Starting from an initial guess, a model refinement can be achieved by a trial–and–error procedure. However, this method is likely to be more time–consuming, because of erroneous model guesses. Second, such an approach automatically limits the complexity of the earth model, because the manual control of a large set of unknowns is hardly feasible. Finally, a certain amount of experience with the EM responses of multidimensional structures is required.

2.1 Methodology

The inversion method presented in this chapter, also referred to as SINV, is optimized for problems characterized by the above listed aspects. The idea of the scheme is the combination of a Marquardt–Levenberg [*Levenberg*, 1944; *Marquardt*, 1963] method as a stable inversion scheme with the 3D forward modeling code from *Druskin and Knizhnerman* [1988]. The approach addresses the large–scale difficulty by limiting the number of model unkowns to as many unknowns as typical for Marquardt inversions. Inverting for a low–parameterized model involves an over–determined system to be solved. This provides for the capability of resolving multi–dimensional structures even if only a limited amount of field data is available.

The large–scale character of full 3D inversions originates from the usual practice of treating the discrete cells of a finite–difference or finite–element mesh as model unknowns. Such a fine model parameterization quickly leads to a huge set of parameters, but offers a maximum of degrees of freedom during an inversion. Here, the model variation is constrained in a way that a resistivity structure, given by the parameters of the starting model, cannot be changed to a completely new structure. To describe a 3D earth, this involves alternative types of model unknowns, which need to be adapted to the structures of interest. Therefore, it is crucial that sufficient a priori information exists to define proper model parameters. If not present at all, a trial–and–error forward modeling may be the only practical alternative to find a suitable parameterization of the underground. Examples for rather unconventional parameterizations are shown in the course of this chapter. It will be seen that even low–parameterized models can lead to relatively complex 3D structures.

2.1.1 The forward modeling code

The forward modeling code is based on the spectral Lanczos decomposition method (SLDM). The theory of this solution method is described by *Druskin and Knizhnerman* [1988; 1994]; *Druskin et al.* [1999]; a brief summary is also given by *Hördt et al.* [1992]. The solution of the 3D diffusive Maxwell equations by SLDM involves Krylov subspace techniques. Traditional Krylov subspace techniques include the conjugate–gradient method, biconjugate–gradient method, and quasiminimal residual methods [*Madden and Mackie*, 1989; *Alumbaugh et al.*, 1996; *Smith*, 1996]. These techniques are very efficient for the solution of large linear systems with a sparse matrix. The application of SLDM for solving Maxwell's equations involves approximating the equations on a spatial FD, thus yielding a system of ordinary differential equations. The system's solution is written as the product of functions of its stiffness matrix and the vector describing the initial conditions. The solution on a Krylov subspace can be thought of as a natural extension of the conjugate–gradient method to the computation of arbitrary matrix funtionals [*Druskin and Knizhnerman*, 1994].

It is crucial that the convergence characterisics of SLDM are taken into account when designing a FD discretization for a given earth model. Here, the most important aspects are outlined. A detailed and more theoretical description is given by *Druskin and Knizhnerman* [1994]. The convergence of SLDM depends on the differential equation system's condition number, that is the ratio between largest and smallest eigenvalue. The condition number depends on the aspect ratio of a FD grid. Ill–conditioning due to a large condition number is introduced by high conductivity contrasts. This results from the requirement that for the application of SLDM the grid discretization should be fine in conductive regions and coarse in more resistive regions in order to achieve a proper simulation of the attenuation characteristics of EM fields. Hence, convergence problems may occur in the presence of high contrasts if a compromising grid discretization cannot be found. Furthermore, a fine grid should be used to ensure accurate results at early times, whereas low frequency fields need coarse spacings for a quick convergence. Therefore, the simulation of late times also decrease the convergence due to large FD grid aspect ratios.

The forward simulation code allows to define the material properties of the earth, i.e. electric conductivity and magnetic permeability, by means of rectangular blocks. Both conductivity and magnetic permeability do not vary over the block volume. The corners of the blocks are not required to be confined to the cells of the FD grid. However, conductivity contrasts between adjacent blocks should be taken into account when designing the FD grid. The inverse interpolation of the distribution of material properties onto the FD grid is realized by a material averaging scheme described by [*Moskow et al.*, 1999]. This scheme allows to define arbitrary model parameters by the composition of one or more blocks such that they form volumes of constant resistivity.

2.1.2 The Marquardt–Levenberg inversion scheme

The Marquardt–Levenberg inversion scheme (e.g. *Jupp and Vozoff* [1975]; *Lines and Treitel* [1984]; *Hördt* [1989]) represents a stable iterative method in the presence of ill–posed inversion problems, where small changes in the data can lead to large changes in both the solution and in the process that finds the solution. First consider the classical least–squares approach for inverting a set of observed data for a given earth model parameterization $\mathbf{m}$ [*Jackson*, 1972]. Basically, this involves minimizing the cost functional ϕ, quantified as the difference between the vectors of the observed and predicted measurements $\mathbf{d}^o$ and $\mathbf{d}^p$, respectively,

$$\phi(\mathbf{m}) = (\mathbf{d}^o - \mathbf{d}^p)^T (\mathbf{d}^o - \mathbf{d}^p), \tag{2.1}$$

which is also called the Gauss–Newton approach [*Lines and Treitel*, 1984]. The cost functional is connected with a model guess by the implicit dependence of the predicted data on $\mathbf{m}$. In order to treat the non–linearity of minimization problems related to TEM inversion problems, the model response

$$\mathbf{f}(\mathbf{m}) = \mathbf{d}^p$$

is typically assumed to be a linear function of the parameters such that a perturbation of the model response about a given starting model $\mathbf{m}_0$ can be represented by a first–order Taylor expansion

$$\mathbf{f}(\mathbf{m}) \approx \mathbf{f}(\mathbf{m}_0) + \mathbf{J}\delta\mathbf{m},$$

with $\delta\mathbf{m} = \mathbf{m} - \mathbf{m}_0$ defining the model perturbation. The matrix $\mathbf{J}$ represents the partial derivatives of the predicted data with respect to the model parameters,

$$\mathbf{J}_{ij} = \left.\frac{\partial f_i}{\partial m_j}\right|_{\mathbf{m}=\mathbf{m}_0}, \qquad i = 1, ..., N; \;\; j = 1, ..., M, \tag{2.2}$$

and is also referred to as parameter sensitivity matrix or Jacobian. The size of $\mathbf{J}$ is $N \times M$, given by the number of observed data points and the number of model unknowns, respectively. For the solution of Equation (2.1) it follows [*Lines and Treitel*, 1984]

$$\delta\mathbf{m} = (\mathbf{J}^T\mathbf{J})^{-1}\mathbf{J}^T\delta\mathbf{d}, \tag{2.3}$$

where $\delta\mathbf{m}$ now represents the parameter change vector that has to be applied to a model guess $\mathbf{m}_0$ in order to decrease the data misfit $\delta\mathbf{d} = \mathbf{d}^o - \mathbf{d}^p$. The linear approximation of the non–linear forward function $\mathbf{f}$ involves a step–wise minimum search by evaluating the Gauss–Newton solution (2.3) in an iterative manner, starting from the initial model guess.

The unconstrained least–squares solution (2.3) has the undesirable property of being unstable in the presence of a singular or nearly singular matrix $\mathbf{J}^T\mathbf{J}$. Therefore, the basic strategy of the Marquardt–Levenberg scheme consists of adding a further constraint to the least–squares problem (2.1). To reduce the difficulties with a singular matrix $\mathbf{J}^T\mathbf{J}$, a Lagrange multiplier problem is solved subject to the constraint of a bounded energy of the parameter change, specifically

$$\phi(\mathbf{m}) = \delta\mathbf{d}^T\delta\mathbf{d} + \beta(\delta\mathbf{m}^T\delta\mathbf{m} - \delta m_0^2), \tag{2.4}$$

where δm_0^2 is a finite quantity. The minimization of this functional leads to the so–called damped least–squares solution for the model update [*Jupp and Vozoff*, 1975]

$$\delta\mathbf{m} = (\mathbf{J}^T\mathbf{J} + \beta\mathbf{I})^{-1}\mathbf{J}^T\delta\mathbf{d}, \tag{2.5}$$

where the matrix $\mathbf{I}$ denotes the identity matrix. The potential singularity of $\mathbf{J}^T\mathbf{J}$ is thus relieved by adding a constant to its main diagonal[1]. The degree of damping is controlled by the parameter β. As common practice in Marquardt schemes, for the inversions shown in this work a threshold level is raised by the damping parameter in the first iteration so that only the basic features of the model will be resolved. A gradual decrease of β accounts for less resolved model parameters at later iterations. To define a stopping criteria for an inversion, a lower treshold for the relative error functional decrease, with respect to the previous iteration, is chosen in advance.

---

[1] This can also be understood as adding a DC level to the eigenvalues of $\mathbf{J}^T\mathbf{J}$ such that none of the eigenvalues can vanish.

The presence of data errors assigned to the observations $\mathbf{d}^o$ is addressed by incorporating a weighting matrix $\mathbf{W}$ into the minimization problem (2.4). Usually, $\mathbf{W}$ is a diagonal matrix, where its entries are the reciprocal values of the standard deviations of $\mathbf{d}^o$ [*Jackson*, 1972]. Incorporating the data weighting changes the solution in (2.5) to [*Hördt*, 1989]

$$\delta\mathbf{m} = (\mathbf{J}^T\mathbf{W}^2\mathbf{J} + \beta\mathbf{I})^{-1}\mathbf{J}^T\mathbf{W}^2\delta\mathbf{d}. \tag{2.6}$$

The types of model parameters and its small number do not require a further regularization using smoothing constraints (e.g. *Tikhonov and Arsenin* [1977]; *Constable et al.* [1987]; *DeGroot-Hedlin and Constable* [1990]). However, bounding only the energy of the parameter change may still lead to physically unreasonable parameter contrasts. This becomes more severe with the presence of parameters that are poorly resolved by the data. Therefore, the model parameters have to be chosen such that an ill–posedness through irrelevant parameters is avoided. Generally, there is a limit to the number of well defined or important parameters that may be resolved from the data [*Jupp and Vozoff*, 1975].

Information about the resolution of a model parameter can be obtained from the spectral decomposition of the Jacobian [*Jackson*, 1972; *Jupp and Vozoff*, 1975]. *Hördt* [1989] and *Petrat* [1996] describe the derivation of the so–called importance values from the inversion statistics resulting from the Singular Value Decomposition [*Lanczos*, 1958] of the Jacobian. Importances represent a means of estimating a model parameter's degree of resolution and thus help to find the optimal number of parameters. Such importance estimations are employed for the later presented data analysis. Here, it shall only be recapitulated that importances vary between 0 and 1, which means a minimal and maximal resolution of a parameter, respectively.

The calculation of the sensitivity matrix $\mathbf{J}$ is usually the most time–consuming part of an inversion procedure, because this requires calculating the variation in the data produced by a change in the model parameters at each iteration. If a perturbation method is employed, each model parameter requires a separate forward simulation for its perturbed quantity. More efficient possibilities exist to calculate parameter sensitivities. *McGillivray et al.* [1994] calculate sensitivities for inversion of frequency–domain data using an adjoint equation method. A time–domain equivalent for LOTEM data is presented by *Hördt* [1998]. The principles of the adjoint method will be described in detail in Chapter 4. The method is appropriate for a numerous set of unknowns in the form of cell–based grid elements. Here, both the limited number and the types of model parameters suggest the classical perturbation method for calculating the sensitivities.

Data and model parameter transformation

Diffusive EM fields have widely different amplitudes at different times and receiver locations. To reduce the dynamic range of the data, transformations are preferable in order to equalize the influence of each datum. Otherwise, the error functional of Equation (2.4) may be dominated by high amplitude data points, thus deteriorating the convergence in an inversion [*Meju*, 1994]. A simple logarithmic transformation [*Jupp and Vozoff*, 1975] can be used if all data points possess the same sign. However, TEM measurements over 3D structures often involve sign reversals over the measurement time range, thus requiring to distinguish between positive and negative data. Different methods exist to take both large amplitude variations and different signs into account. For example, *Wang et al.* [1994] use a logarithmic transformation with a linear scale straddling amplitudes near zero and a discrimination between positive and negative logarithms of data values. The transformation scheme realized in SINV is described by *Scholl* [2001] and is based upon the Area–Sinus–Hyperbolicus function. The funtion has a logarithmic behaviour for arguments $\gg 1$ or $\ll -1$ and a linear one for arguments close to zero. This transformation has proven to be suitable for the 1D inversion of LOTEM data containing sign reversals [*Scholl*, 2001]. Depending on the LOTEM transmitter–receiver geometry and the type of the field component, sign reversals can occur over a 1D earth [*Petry*, 1987].

An important constraint on model parameters such as electrical conductivity or layer thickness is that they must be positive quantities. To enforce this constraint on the inverse solution, a logarithmic transformation is applied to the parameters for all inversions presented in this chapter. A discussion about alternative transformations for parameters describing model features that can involve negative values will be given at a later stage.

It needs to be taken into account that both data and model parameter transformations carry over to the calculation of the Jacobian in Equation (2.2). Furthermore, the data transformation affects the data errors and thus the weighting matrix **W**. *Scholl* [2001] outlines these aspects in great detail for different types of transformations.

Parallel implementation

To update the Jacobian at each iteration makes up the majority of the computational effort for an inversion. It needs one forward simulation for each perturbed model parameter plus one extra simulation for the unperturbed model. The case history in Section 2.3 will show that the forward modeling procedure with the SLDM code may involve more than one FD simulation grid. In this case, the number of forward computations for the model perturbation has to be carried out for each grid.

Calculating the Jacobian can be highly accelerated if a parallel computing platform is used. As the forward simulations for the perturbed model parameters are carried out independently from each other, they can be distributed among several processors. The optimum number of processors would therefore equal the number of forward simulations required for one iteration. This would reduce the computation time by a factor of that number in an ideal case. No inter–processor communication is needed and thus a serial version of the forward modeling code can be used. Communication between the forward simulation code and the inversion algorithm is done via temporary disk files. This way of parallelizing SINV represents not an optimally coded program, because a parallelized version of the SLDM code may be more efficient. However, the implementation is simple achieving a significant gain in computation time. Moreover, as shown by *Scholl et al.* [2002], this parallelization scheme is also suitable for several stand–alone computers connected by a network.

In a test inversion run, altogether 264 forward simulations were required. A single simulation needed an average of 2.5 minutes real computation time on a single node of a SUN^{TM} Fire 6800 compute server which would sum up to a total time of approximately 11 hours. Using 8 processors this time could be decreased to 2.5 hours.

2.2 Synthetic data examples

In the following SINV is tested on different model parameterizations. Concerning the aspects related to the convergence of SLDM, a stable FD grid for the SLDM code could easily be found, because no excessively high resistivity contrasts are involved in the shown examples. A more thorough discussion about the preliminary procedure of finding a proper FD grid discretization will be given in Section 2.3. There, designing a stable grid becomes far more difficult due to higher resistivity contrasts. All synthetic data to be inverted for the tests is created by another 3D code presented later in Chapter 3. No artificial noise is added to the data, because here only the case of an optimal data quality shall be treated. The stopping criteria is fulfilled in the case of a relative data misfit decrease dropping below 1 %, relative to the previous iteration. In order to avoid that the inversion finishes too early due to a low relative misfit decrease, a minimum of 4 iterations is enforced.

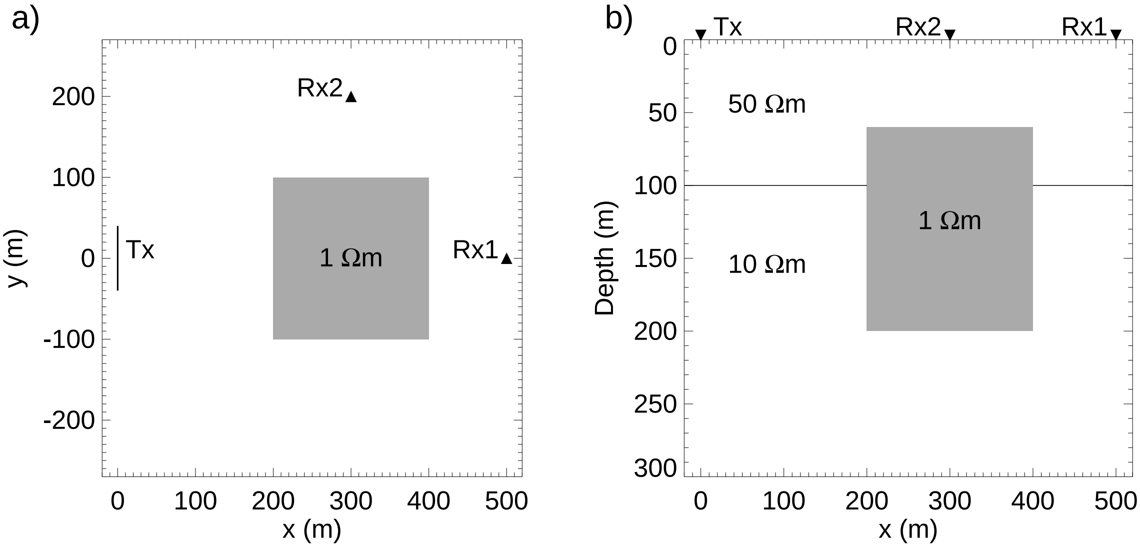

Figure 2.1: *Model of a 3D conductive body embedded in a two–layered host used to invert for different examples of model parameterizations. (a) Plan view, (b) vertical section.*

Consider the 3D model in Figure 2.1. The model represents a 1 Ωm conductive cube embedded in a two–layered half–space. The horizontal dimensions of the body are 200 m on a side with a vertical size of 140 m and its depth starting at 60 m. The thickness and resistivity of the upper layer are 100 m and 50 Ωm, respectively, above a 10 Ωm basement. A horizontal grounded–wire source of length 80 m is located at 200 m distance to the block. The example shall demonstrate that SINV is suitable for problems with smaller dimensions of the field–setup than exemplified in the later shown case history. The data simulated at the receivers comprises the electric field component in a direction parallel to the source orientation and the time derivative of the vertical magnetic induction $\frac{\partial}{\partial t}b_z$ (voltage).

2.2.1 Inverting for layered background and block resistivity

The model parameterization of the first series of inversions assumes the true position and geometry of the block as known in advance and as fixed. Also, the existence of a two–layered background without its exact structure shall be given as a priori information. The free parameters are thus given by the layer parameters, these are the resistivities ρ_1 and ρ_2 of both layers and the thickness z_1 of the top layer. The fourth parameter is represented by the block's resistivity ρ_b. Altogether 6 inversions are carried out, each one using a different input data set in terms of the receiver position and the data type, where both separate and combined sets are involved.

For each inversion, the input data originates from only a single receiver location in order to simulate the case of a sparse data covering of the target. The inversion results numbered by 1–6 are summarized in Table 2.1. The first and the second line of the table contain the parameters describing the true case and the chosen initial model, respectively. For these examples, all resistivities are initialized to a value of 50 Ωm and the top layer's thickness is set to a starting value of 50 m. Two different receiver positions are chosen (Figure 2.1), the first one (Rx1) located at a distance of $x = 500$ m from the source without offset along the source axis, the second one (Rx2) at $x = 300$ m and $y = 200$ m. According to *Petrat* [1996] and *Schneider* [2000] these receiver positions do not provide for an optimal resolution of the block anomaly. Thus, the example will also demonstrate that in addition to the sparse amount of inverted data, a reconstruction is still possible with a less optimal receiver configuration.

With the receiver placed at Rx1 and the inversion fed by the electric field data, the true model can be reproduced closely within 12 iterations. The deviation from the true model amounts to only a few percent for each parameter. The voltage data result reveals a worse reproduction of the top layer's parameters, whereas the basement resistivity is matched. Starting from a value of 50 Ωm, the conductive block is well approximated by a resulting value of $\rho_b = 1.7$ Ωm. The combined data inversion leads to the most exact final model. Apart from a relative difference of approximately 10 % between the true and the reconstructed top layer resistivity, all other parameters show relative errors below 1 %.

In general, inverting the data originating from receiver Rx2 shows larger deviations from the true model. This follows from a worse resolution of the anomalous block, compared to the receiver placed at Rx1. Still a satisfying reproduction of the true underground is achieved by inverting the electric field data during 17 iterations, where also the block resistivity is approximated. However, the voltage data inversion fails to find most of the real model features, with the exception of the basement resistivity. Compared to result 4, the combination of both data types (result 6) produces a similarly good layer model, however with a more erroneous block resistivity.

The electric field data sets of both receivers are sufficient for a reasonable resolution of the true parameters and are now used in order to exemplify the influence of an erroneous model

Result	Rec. pos.	Data type	Iterations	ρ_1 (Ωm)	z_1 (m)	ρ_2 (Ωm)	ρ_b (Ωm)
True model				50	100	10	1
Initial model				50	50	50	50
1	Rx1	E_x	12	50.8	104.0	9.4	1.1
2	Rx1	$\dot{B}_z$	7	63.9	79.1	10.1	1.7
3	Rx1	$E_x + \dot{B}_z$	10	54.5	100.8	9.9	1.0
4	Rx2	E_x	17	49.0	103.1	8.5	2.4
5	Rx2	$\dot{B}_z$	4	243.6	56.1	12.2	39.1
6	Rx2	$E_x + \dot{B}_z$	8	53.2	96.6	9.3	8.7
7	Rx1	E_x	5	175	101.1	32.6	13.8
8	Rx2	E_x	10	35.7	55.9	31.1	29.2

Table 2.1: *Inversion results for different data receiver positions and data types. The model parameterization involves the layer unknowns ρ_1, z_1 and ρ_2 and the block resistivity ρ_b. Results 1–6 involve a conforming block geometry, results 7 and 8 a nonconforming geometry.*

Result	Iterations	ρ_1 (Ωm)	z_1 (m)	ρ_2 (Ωm)	z_2 (m)	ρ_3 (Ωm)	ρ_b (Ωm)
Initial model		50	100	50	100	50	50
1	6	61.8	35.6	39.6	74.3	9.4	1.0
Initial model		100	100	100	100	100	50
2	14	56.7	85.1	59.2	11.9	9.8	1.2

Table 2.2: *Inversion results for the data computed at Rx1 from the model shown in Figure 2.1. In addition to the block parameter ρ_b, three layer unknowns are allowed to describe the two–layered background.*

parameterization. Using the input data produced by the original model shown in Figure 2.1, the model guess is now characterized by a nonconforming block geometry. Instead of a volume of $200 \times 200 \times 140$ m^3, the block is assumed to have a fixed volume of $300 \times 300 \times 200$ m^3, where its center position is kept. Due to the larger volume, erroneous results are obtained for each inversion as shown in the results 7 and 8 in Table 2.1. However, except for the top layer's final resistivity of each result, all parameters show a trend towards the correct solution, with respect to the starting model. Even the true thickness of the overburden is found by inverting the data of Rx1. Compared to the real values, the larger block volume causes increased values for the resulting block resistivity.

Another test for a less conforming model parameterization involves the assumption of a three–layered background, thus inverting for 5 layer parameters. An additional unknown is again represented by the cube's resistivity with the true geometry given. The joint data set of Station Rx1 generated by the two–layered model in Figure 2.1 is used for this test. All initial resistivities are set to a value of 50 Ωm. Both layer thicknesses start with values of 100 m. First, it can be seen from Table 2.2 (result 1), that the block resistivity is matched exactly. However, both final layer resistivities ρ_1 and ρ_2 differ by approximately 10 Ωm from the true case, despite correct initial values. Nevertheless, the two–layered background can be recognized. The sum of both thicknesses z_1 and z_2 shows the original vertical location of the basement's beginning with a deviation of 10 %. Its true resistivity of $\rho_3 = 10$ Ωm is closely matched.

A similar inversion (result 2) uses the initial resistivities of 100 Ωm for ρ_1, ρ_2 and ρ_3. In general, the final model result is better than given by the previous inversion. However, both resistivity values ρ_1 and ρ_2 still show differences of 13 % and 18 %, respectively, from the true value of 50 Ωm. The overburden thickness is reconstructed by the sum of z_1 and z_2 with an error of only 3 %. The resistivity ρ_3 of the layer below the overburden and the block's resistivity ρ_b are reproduced to a satisfying degree as well.

2.2.2 Inverting for block position and resistivity

The following two inversions involve a model parameterization that is different from the more common types of parameters given by layers or blocks. The combined data of electric field and voltage at Station Rx1 is inverted. It is generated from a 50 Ωm homogeneous half–space with an embedded anomalous block as the one shown in Figure 2.1. No layer parameters are defined for these inversions, thus a fixed 50 Ωm background shall be assumed in the inversion. In addition to the block's resistivity ρ_b, the model parameters are now represented by its center coordinates x, y and z along each cartesian axis, thus four unknowns exist. The starting model for the first inversion example assumes a 50 Ωm block with its true size also known.

As shown by the plan view and vertical section of Figure 2.2a, the initial model (dashed rectangles) is characterized by a 100 m offset from the true position for both horizontal coordinates x and y and a 40 m offset from the true depth. The solid lines mark the resulting block location after 8 iterations. The inversion moves the initial block towards the original location (shaded rectangle) such that a good agreement along both the x axis and the vertical axis is achieved. The only significant deviation of approximately 20 m from the true position occurs along the y axis. The block's resistivity of 1 Ωm is reproduced exactly in this example. For both data components Figure 2.2b shows the synthetic data generated by the original model in comparison with both the initial response and the response calculated from the solution. Apart from slight deviations at the latest times of the electric field data, both predicted data curves show a good agreement with the original data.

In order to exemplify another inversion with a less conforming parameterization, the block's geometry is now assumed to be 50 m larger along each dimension, as illustrated by the dashed rectangle in Figure 2.2c. Also, the starting position is shifted farther away from the true position, such that its center coordinates differ by values of $\Delta x = 225$ m, $\Delta y = 225$ m and $\Delta z = 265$ m from the true center point coordinates. The final model result reveals a successful inversion, because the real block is enclosed by the borders of the larger block after 9 iterations. Similar to the previous example involving a nonconforming block geometry (results 7 and 8 in Table 2.1), the larger block volume causes a trend towards the resistivity of the background. The initial block resistivity of 50 Ωm is decreased to a value of 7.2 Ωm. To

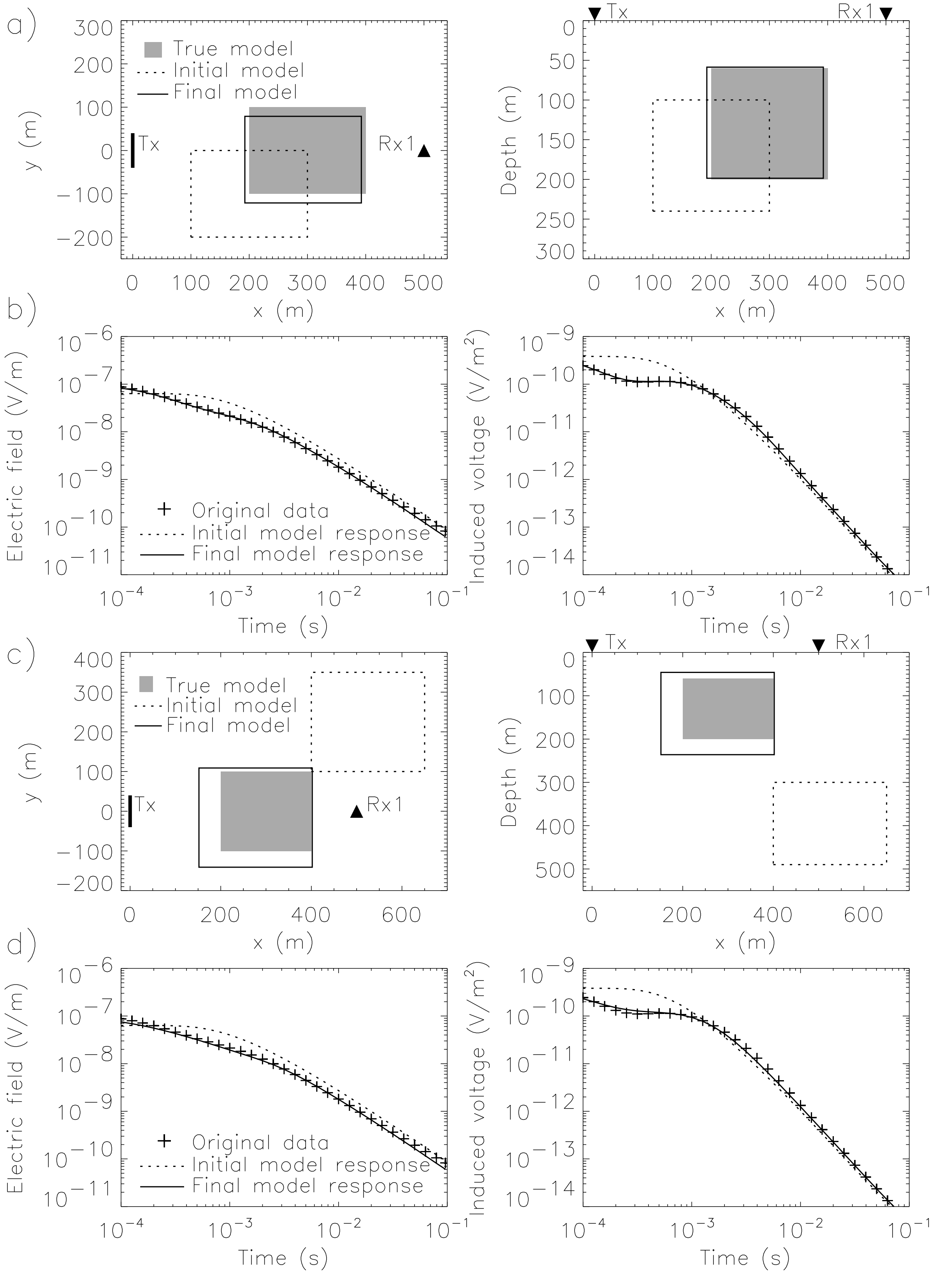

Figure 2.2: *Synthetic data inversion for the resistivity and position of a block embedded in a homogeneous half–space. (a) Plan view and vertical section of the true (shaded rectangle), initial (dashed lines) and final (solid lines) block position of an inversion with conforming block geometry. (b) Synthetic data at Station Rx1 in comparison with initial and final model response for both inverted data sets. (c) Initial and final model results for an inversion with nonconforming block geometry and (d) corresponding data fits.*

compare, this yields a conductance (product of conductivity and volume) of $1.65 \cdot 10^6$ Sm^2, whereas the true block's conductance is $5.6 \cdot 10^6$ Sm^2. Figure 2.2d shows a good agreement between the synthetic data and the response of the inversion result. In contrast to Figure 2.2b, one observes a slight misfit in the early time range of both data types.

2.2.3 Conclusions

The synthetic data examples show the versatility of the scheme in terms of the model parameterization. The restriction to a very limited number of model parameters is somewhat compensated by the capability of defining arbitrary kinds of unknowns. It may be argued that the structural information contained in the parameters, representing given a priori information, is quite detailed for the shown examples. Nevertheless, it shall be emphasized that cases, where other geophysical measurements provide such knowledge, are not rare. An example is given by the following case history. Moreover, the inversions involving nonconforming parameterizations show that a trend towards the real situation is likely to be indicated. By scrutinizing the kind of data misfits and checking the question of how realistic a solution appears, less satisfying model results can still be used for a parameter refinement. This is also exemplified in the case history. Other a priori information, if available, also represents a valuable help in order to judge an inversion result. In addition, varying starting models are suggested to investigate the uniqueness of a solution.

If no prior knowledge about 3D structures is available for the analysis of real field data, 1D inversions can be used in order to obtain information about the background structure, as for example accomplished by *Hördt et al.* [2000*b*]. This requires the existence of data without distortions due to multidimensional structures. Also, 3D forward modeling can be carried out until a satisfying model is found which can be further refined in an inversion, requiring, however, a certain amount of expertise with multi–dimensional modeling. The more favorable approach is enabled by the inversion scheme's given flexibility of defining arbitrary model parameters. Although this may still be regarded as a trial–and–error procedure, inverting for different types of unkowns represents a more efficient way of investigating multi–dimensional structures.

A question to be further investigated is the kind of model parameter transformations used for such unconventional parameters as the position of an anomaly. Here, a logarithmic transformation was kept for all parameters and led to satisfying results. Therefore, in order to avoid negative numbers for the position parameters of the moving block (Section 2.2.2), the model domain was internally shifted to the positive FD grid axes. A linear treatment [*Scholl*, 2001] can be expected to be more adequate for position parameters, because they do not involve such large ranges as usually covered by resistivities.

2.3 Case history: Inversion of LOTEM data from Mount Merapi, Indonesia

The case history shows the inversion of LOTEM data from a survey conducted at the active volcano Merapi. Both lateral resistivity variations in the underground and effects caused by the mountain topography allow the employment of 1D inversion schemes only to some limited extent. A priori information from other disciplines and an earlier LOTEM survey [*Müller*, 2000*b*] exist about the 3D target. The information allows to define suitable model parameters which are then further refined by the inversion method.

Mount Merapi is a basalt to basaltic andesite volcanic complex with a maximum altitude of 2911 m. It is located in the eastern part of Central Java, Indonesia. Merapi's topography is characteristically bell–shaped with a mean dip angle of 5° up to 1300 m, 15° up to 1700 m and 26° up to the summit [*Berthommier*, 1990]. Formation and stratigraphy of the present cone is characterized by a succession of pyroclastic deposits and several violent and partial collapses [*Newhall et al.*, 2000]. According to *Camus et al.* [2000], the growth of the volcano was interrupted several times by violent magmatic to phreatomagmatic eruptions and a Mount St. Helens type edifice collapse in the south–western section. The base of Merapi consists of a sequence of basaltic andesite lavas and intercalated pyroclastic deposits of an eroded older volcanic edifice [*Newhall et al.*, 2000]. This so–called Old Merapi is overlain by the deposits of the modern Merapi which is presently characterized by relatively moderate pyroclastic flows and lahars accompanying growth and collapse of the active summit lava dome.

The LOTEM project at Merapi is a part of a multidisciplinary cooperation of the German Science Foundation (DFG) and the Volcanological Survey of Indonesia (VSI). *Zschau et al.* [1998] presented an overview of all activities. Since the LOTEM technique covers the range between shallow TEM soundings and deeply penetrating MT, an important gap in volcanological investigations is filled [*Müller et al.*, 2002]. Measurements were made during surveys in the years 1998, 2000 and 2001 and are described by *Müller* [2000*b*] and *Commer et al.* [2003] in more detail. The steep topography of the survey area was the main reason for logistical difficulties, thereby prohibiting a fast buildup of the receiver stations. Hence, instead of an area–wide covering of the target, measurements were made at single stations and along a limited number of profiles, where an access was possible. Furthermore, the data quality suffered from a high portion of noise at some stations, thus requiring long recording times in order to obtain satisfying signals by a sufficient number of stacks. Other problems, such as frequent rainfall, also led to a deteriorated data quality at some stations. These difficulties are the reason for a limited amount of available data with sufficient quality for a 3D inversion.

2.3.1 The inverted LOTEM data

The transmitter and receiver positions of the data comprise a subset of all three LOTEM surveys and are shown in Figure 2.3. The receivers were located on the northern, western and southern flanks and at the summit region. All inverted transients are the time derivatives of the magnetic induction and will again be referred to as voltage data. The surveys at Merapi

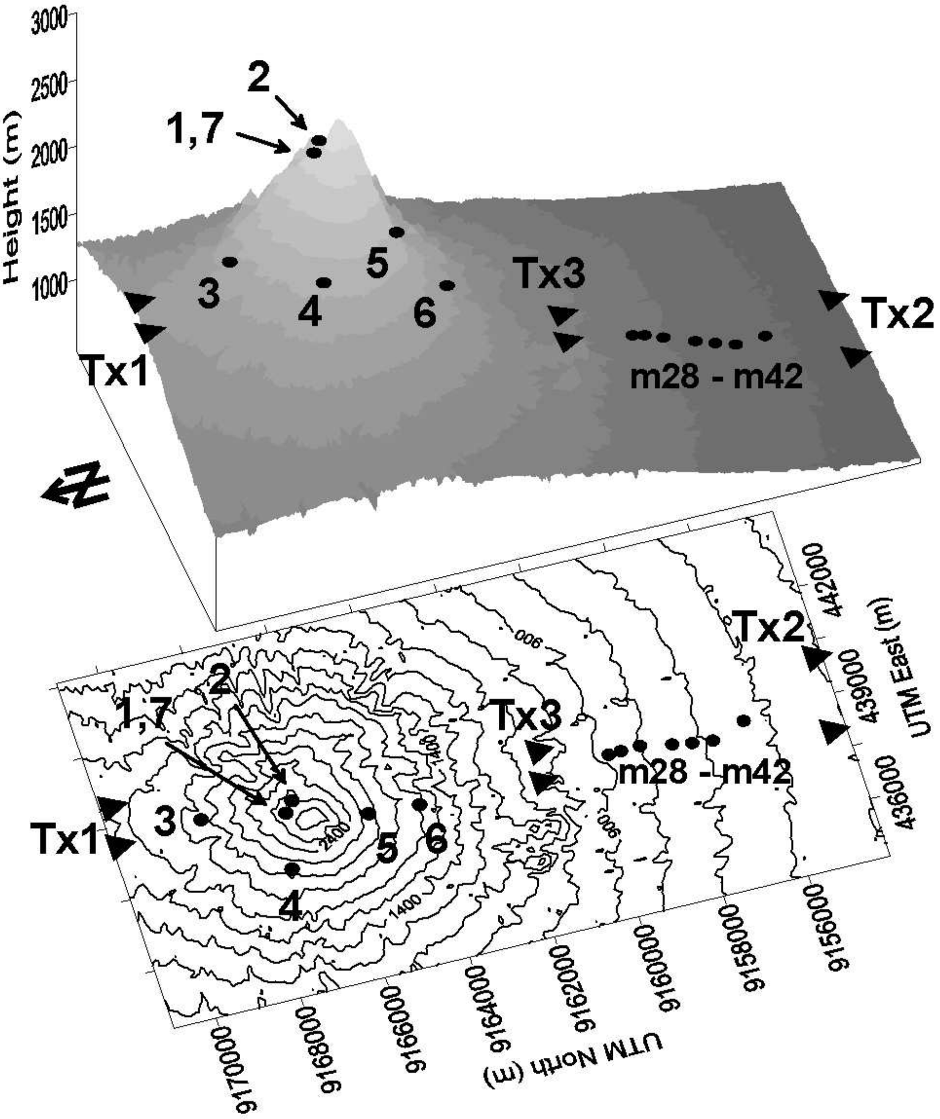

Figure 2.3: *Digital elevation model and contour map of the survey area. Triangles mark the transmitter electrode points, circles mark receiver positions.*

also involved the measurement of electric fields. Unfortunately, most of the electric fields recorded at the stations shown in Figure 2.3 were characterized by a poor quality. Electric fields are very susceptible to a poor galvanic coupling of the sensor electrode pairs (*Helwig*, pers. comm.). This caused significant distortions, because most of the stations in the summit region and along the upper flanks were located on a dry and rocky ground.

The transmitter Tx1 used for Stations 1–6 has a bipole length of approximately 1 km and is located in the North at approximately 4 km distance from the summit at an elevation of 1500 m above sea level. Station 7 was measured at the same position as Station 1 using a different transmitter (Tx2) of 2 km length located at 530 m elevation and 12.8 km distance south from the summit region. The data of the Stations m28–m42 on the southern flank was generated by the transmitter Tx3. This is a 800 m long bipole located at an altitude of approximately 1000 m.

Vertical voltage components are available at all shown receiver positions. In addition, horizontal components with sufficient data quality were recorded at Stations 4–6. By convention, horizontal components are named according to the orientation with respect to the transmitter, where x and y will denote a parallel and perpendicular direction of the magnetic field, respectively. Two different types of sensors were employed for recording the voltages. The summit region with a relatively large plateau allowed recording the vertical field with wires arranged in a horizontal square loop of 40×40 m^2 at Station 1. Second, smaller ferrite core magnetic induction coils (type Zonge TEM–3) were used for the horizontal components. These sensors were also used for the vertical components in the more rugged terrain on the flanks, although a wire loop is preferable due to a larger effective coil area. A detailed study about the application of the TEM–3 sensors for recording the time derivative of the horizontal magnetic induction at Merapi was given by *Stahl* [1999].

The usage of different sensors requires that each simulated transient needs to be processed individually in order to compare it with the measured one. This results from the effect of the so–called system response, which is a combination of the effects caused by analogue low–pass filters in the recording units, deviations of the transmitter input waveform from an ideal step and sensor characteristics [*Hördt et al.*, 2000*b*]. It causes a distortion of the early times and is measured in the field by placing a receiver so close to the transmitter that the earth response can be considered as an impulse [*Strack*, 1992]. Deconvolution of the system effects in the time domain is numerically unstable [*Hanstein*, 1992]. Hence, to avoid the loss of early time information by truncating distorted data, the 3D model responses of the SLDM algorithm are convolved with the corresponding system response of each simulated transmitter–receiver setup.

The field setup in Figure 2.3 clearly shows that topography has to be considered in order to account for the high altitude differences of some field setups. Moreover, depending on the transmitter–receiver geometry, the electromagnetic coupling between the mountain and deeper–lying structure causes effects, which would not be observed over a flat surface [*Hördt and Müller*, 2000]. For example, such effects could be clearly identified in the vertical voltage responses at Stations 5 and 6, as will be shown below.

2.3.2 A priori information

Among many geophysical disciplines, results from the first LOTEM survey, DC resistivity imaging and magnetotelluric (MT) measurements were used in order to define a suitable model parameterization for the inversion attempts including Stations 1–7 and transmitters Tx1 and Tx2 (see Figure 2.3). *Müller et al.* [2002] merged 1D LOTEM inversion results into a 2D pseudo–section originating from measurements along the northern and southern flank, including a single summit station. A predominant feature in this section was the presence of a conductor with downwards decreasing resistivities. Minimum values range from 6 Ωm below the summit to approximately 20 Ωm below the flanks. The upper edge of the conductor was located in a roughly constant depth of 500–1000 m from the surface. The results also suggested a southward extension of the conductor beyond the southern flank.

Friedel et al. [2000] found that the isoresistivity lines from DC resistivity measurements along the south and west flanks nearly follow the topography. A gradual resistivity decrease with depth is observed, where resistivities below 30 Ωm occured below 500–1000 m from the surface. MT measurements [*Hoffmann-Rothe et al.*, 1998] suggested a 1D resistivity model of 2–10 Ωm at a depth of 1 km below a location on the western flank (1300 m above sea level) and indicated that the conductor is not confined to the central part of the volcano. This was in accordance with results from a regional MT profile across Central Java [*Ritter et al.*, 1998] where similar conductors were found. *Müller* [2000*a*] mentioned that a rise of the conducting layer below Merapi's summit was confirmed by the magnitude of the induction vectors from MT sites located at the altitude range of 1700–2000 m. Their 3D MT forward modeling results including topography are shown in Figure 2.4. A major conclusion is that the best fit to the observed induction vectors with periods from 0.1–10 seconds is achieved by a model with a rising 10 Ωm conductor located in the volcano's center (letter D). This structure is shaped roughly following the terrain structure with its upper boundary between 1–1.6 km below the surface. However, it might be a simplification of a gradual resistivity decrease with depth [*Müller*, 2000*a*]. To explain the induction vectors for periods above 10 seconds, the good conductor is extended downwards with even higher conductivities of 0.1–1 Ωm (letters B,C,F).

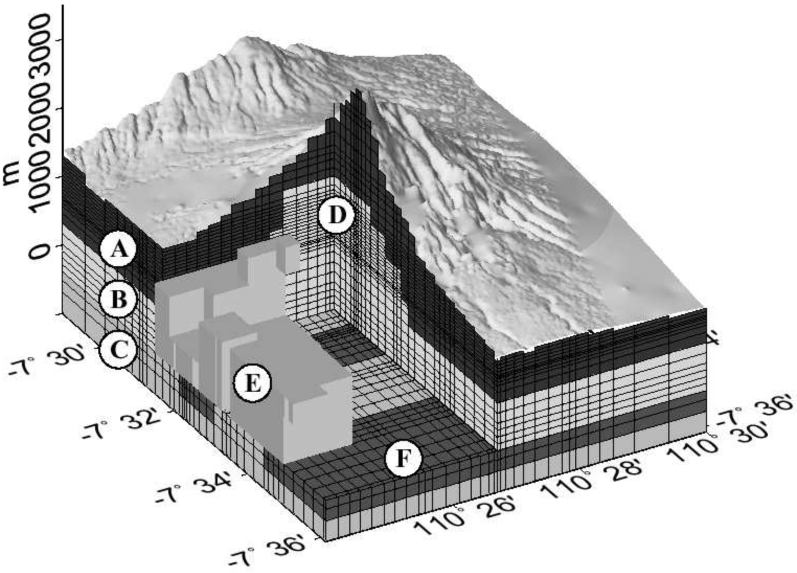

Figure 2.4: *Final 3D resistivity model obtained from MT measurements (after Müller, A., pers. comm.). Here, Merapi is viewed from a SW point. Each letter indicates a region of different resistivity: (A) upper layer, 100 Ωm, (B) intermediate conducting layer, 10 Ωm, (C) conducting layer, 1 Ωm, (D) central conductor, 10 Ωm, (E) SW–anomaly, 1 Ωm, (F) two 2D extended conductors, 0.1 Ωm.*

Although mainly the flanks were covered by the described a priori data, the results supported the hypothesis of a conductive system in the volcano's interior, according to *Zimmer and Erzinger* [1998] probably caused by hydrothermal activity. For the first 1000 m below the surface of the volcanic edifice, the a priori information suggests a somewhat layered resistivity structure, where the layer boundaries follow the mountain topography. Furthermore, a monotonous resistivity decrease was observed by all mentioned disciplines. At depths below 1000 m, low resistivities with values around 1 Ωm seem to dominate. In this work the inversions of Stations 1–7 will hence involve a layered volcanic edifice. The model parameters are represented by both layer thicknesses and resistivities.

The inversion of the southern flank profile data (Stations m28–m42) involves a different earth model parameterization. This profile comprises 7 stations, where vertical voltages were measured. Each transient is characterized by multiple sign reversals, indicating strong effects by 3D structures. A first interpretation approach by means of 3D modeling has been carried out by *Müller* [2000*b*]. Although no quantitative fit of these stations was achieved, a conductive block close to the surface at the northern end of this profile seems to be the most likely explanation in order to obtain a qualitative fit of the sign reversals. This result will be used as a starting basis for an inversion attempt, where the vertical and lateral position of a conductive block serve as variable model parameters.

2.3.3 Constrained mountain model and FD discretization

As mentioned before, designing the mountain model by rectangular blocks is in principle not confined to the given FD grid. *Hördt and Müller* [2000] use this flexibility to simulate mountainous terrain by piling up conductive blocks in a highly–resistive fullspace, which approximates the surrounding air space. However, in order to combine the modeling of topography with varying model parameters, a more versatile scheme is needed. The approach presented here approximates the terrain by vertical columns as illustrated in Figure 2.5a. Every column represents a rectangular block overlaying the FD grid, which is not shown here. The material property of a block is inversely interpolated onto the FD grid by a material averaging scheme [*Moskow et al.*, 1999]. To understand the practical realization of the column model, the illustration has to be viewed in a somewhat reversed way: in practice, each column extends from the upper vertical end of the model domain, i.e. the air space border, down to the actual air–earth interface and is assigned to a resistivity value approximating air. Averaged data from a given digital elevation model (DEM) [*Gerstenecker et al.*, 1998] is used to determine the vertical position of each column's lower end. In the vicinity of the receivers, small–diameter columns are used in order to approximate the rough terrain of the volcanic cone. At greater distances the column model becomes coarser.

A variety of possibilities exists to further structure the underground. For example, arbitrary shapes can be designed by including single or multiple extra blocks that form volumes of constant resistivity. The column model is particularly useful if vertical conductivity changes dominate over lateral ones, as is the case for layered structures. Such is indicated by the given a priori information. Therefore, the columns are extended downwards (into the earth) and sectioned according to vertical parameter variations. Similar to 1D inversions, the model parameters are represented by thicknesses and resistivities of a layered structure. The following inversion attempts will involve two kinds of layerings. A first mountain model will be characterized by horizontal layers. Apart from lateral resistivity changes due to the topography, this model type only allows for vertical variations below the surface. The second tin Figure 2.3ype is constrained by using the DEM data such that the layers follow the topogra-

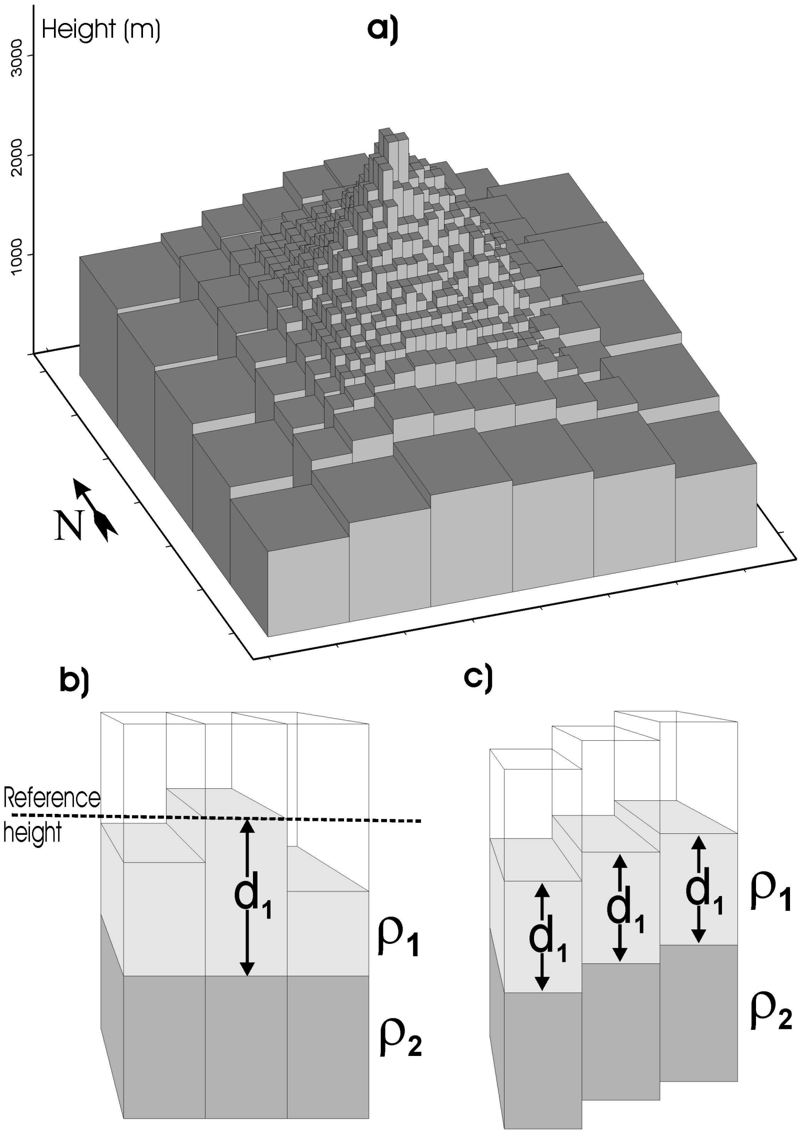

Figure 2.5: *(a) Modeling of the terrain structure of Mount Merapi with a vertical column model. (b) Design of horizontal layering. (c) Design of a layering which follows the topography.*

phy. This model type shall also be referred to as “dome–shaped”.

When inserting the mountain model into the simulation grid, the only fixed parameter of each column is its topographic height; here it is chosen relative to the transmitter height. In order to model topography with a horizontally layered underground, each column is constrained such that its division according to the given thickness parameters starts from a vertically fixed reference position. This is illustrated in Figure 2.5b for a two–layered earth. The reference height represents the top of the layering and is equal to the highest topographic elevation of the mountain. The second type of layering is realized by constraining every column such that the division starts from the vertical position of its air–earth interface. As illustrated in Figure 2.5c, this constraint reproduces the shape of the surface terrain at each layer interface, thus leading to a layered structure that follows the topography.

The later shown inversion attempts with real field data will involve other model features in addition to the layered background. The realization may become complicated, because the SLDM code does not allow the overlap of the rectangular blocks describing a model. There exist two ways for including additional block structures into the column model. First, the space filled by an additional block can be kept free during creation of the column model. This involves scanning the geometry and position of each column section in order to omit the volumes reserved for other shapes. Then the volume can be assigned to an extra parameter, which describes a conductivity and is independent from the layered background. Another approach chosen here is to further split up the columns that intersect a predefined volume such that it is built by a group of adjacent column pieces assigned to the same resistivity of the additional structure. Arbitrary additional shapes can be described by both methods.

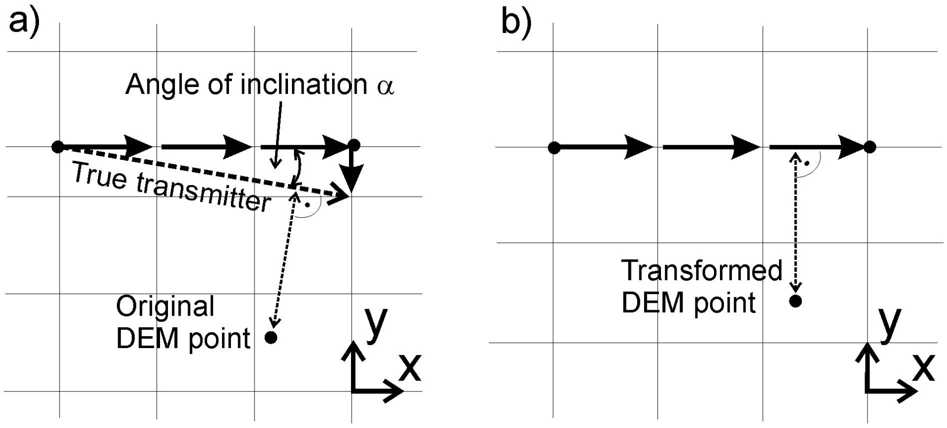

Figure 2.6: *Illustration of the approximation scheme used to simulate nonconforming (to the FD grid) and elongated sources (see Druskin and Knizhnerman [1994] for further details). (a) Small inclination angles require appropriately small grid spacings in order to simulate the correct source orientation with respect to given geographical data included in the FD grid. (b) With an appropriate transformation of the geographical data, this can be avoided.*

As mentioned earlier, large FD grid aspect ratios may cause a poor convergence of the SLDM code and thus wrong late time responses. Although there is a lower limit imposed by the resistivity contrasts in a model, the aspect ratio can be optimized to some level by avoiding that a grid becomes more dense than required by both the resistivity distribution and the simulated measurement time interval. The first thing to achieve this is the careful discretization of the transmitter bipole. Consider the case of a bipole orientation with an inclination to one of the horizontal FD grid axes. The SLDM code allows to piece together an extended transmitter bipole by several dipole elements, where the size of these elements is defined by the grid spacings; see also *Hördt* [1992] for practical examples of transmitters rotated in a FD grid. Figure 2.6a illustrates how a transmitter with a small inclination to the FD grid's x axis is composed by three bipole elements along this axis plus one additional perpendicular element. The vector sum of all elements represents both length and orientation of the true transmitter to be simulated. The smaller the inclination of the transmitter to the grid axis, the smaller the perpendicular dipole element has to be, and this in turn requires a small grid spacing. This way of simulating a given field setup is usually chosen in order to orient the borders of extended 2D or 3D bodies along a grid axis. Otherwise, a rectangular block rotated with respect to the transmitter needs to be approximated by a possibly large number of smaller blocks.

The capability of simulating sources not conforming to the FD grid becomes useful if geographical information is incorporated into the earth model design. For a 3D forward modeling of Merapi's topography, *Müller* [2000*b*] aligns the axes of the Cartesian mesh defined by the FD grid parallel to the axes given by the Universal Transverse Mercator (UTM) coordinate system. This has the advantage that DEM information, needed for the modeling of topography, can be used without further transformation. On the other hand, a needlessly small grid spacing would be required in order to simulate the orientation of the transmitters shown in Figure 2.3, because they are all characterized by a small inclination to the WE–direction. To avoid this, it is preferable to carry out a transformation of the complete DEM such that one of its horizontal axes conforms to the transmitter orientation. For the example given in Figure 2.6a, this involves a rotation of each DEM point around the left source electrode point, where the rotation angle is given by the inclination α to the x axis. Afterwards, the x axis of the transformed DEM is parallel to the transmitter orientation. Creating the column model from the DEM now allows for a coarser FD grid as shown by Figure 2.6b.

Another type of difficulty is related to the vertical grid discretization at the receiver side, because the SLDM code allows the sampling of fields only on actual vertical grid levels. In the vicinity of the summit, the modeling of the resistive air space requires a coarse grid interval. It is actually much coarser than the vertical spacing given by the altitude differences of the summit stations and thus cannot be matched with the receiver positions. Nevertheless, importance was attached to sampling the fields at the exact vertical receiver positions in order to simulate the topography effects correctly. To achieve this, the fields at the true receivers are calculated by trilinear interpolation [*Press et al.*, 1992], incorporating a cube of eight surrounding grid nodes in which the desired position falls. A drawback may be seen in the interpolation errors caused by a linear assumption for the field variation inside of the cube. However, tests showed that the interpolation errors are not significant, compared to errors caused by an otherwise wrong vertical sampling.

2.3.4 Stability checks

Although SLDM allows for very fast solution times, the convergence characteristics described in Section 2.1.1 have to be taken into account, because an inversion scheme without smoothing constraints may produce models with high contrasts. Moreover, high contrasts are introduced by modeling the air layer. Hence, the grid design needs to come along with stability checks to provide accurate simulation results for varying models during an inversion. As will be shown below, the vertical voltage data measured at Station 1 (Figure 2.3) contains the largest measurement time range of approximately three decades. Therefore, this station turned out to be the most critical, because no compromise between the grid requirements imposed by the convergence characteristics of SLDM could be found. The solution of this problem involves joining the FD responses of two different grids, i.e. a fine one for the early part of the time range and a coarser one for the later times. All other stations could be simulated using a single FD grid.

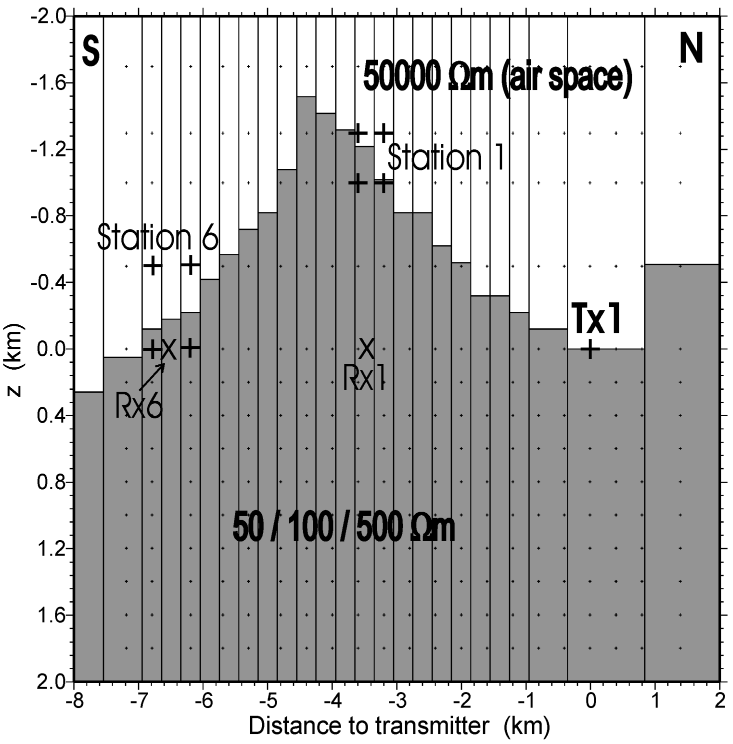

Figure 2.7: *North–south oriented section of a homogeneous mountain model through the summit. In order to verify FD grid stability, the 3D responses for different mountain resistivities are calculated at Stations 1 and 6 and are compared with the corresponding analytical solutions without topography at the positions Rx1 and Rx6, respectively.*

The stability checks described in this section comprise two parts and shall be demonstrated at the field setup of Stations 1 and 6. Together with Station 5, these stations show the strongest influence due to topography. First, it is tested for Station 1 whether the SLDM results converge in the presence of progressively higher contrasts for both of the employed FD grids. A homogeneous mountain model proved to be sufficient since the highest contrast occurs at the air–earth interface. The air resistivity is approximated by a value of 50000 Ωm. Figure 2.7 shows a north–south oriented vertical section of the mountain through the summit. First, the figure illustrates once more the model concept of vertical columns for the topography. To model a homogeneous mountain, every column section below the air–earth interface is assigned to the same resistivity. The vertical FD grid used for simulating the earlier measurement time range is represented by dotted lines in Figure 2.7. Note the fine spacing inside of the volcano (below $z = 0$ km), designed to account for the high conductivities expected from a priori information, in comparison with a coarser spacing for the air space above the transmitter. The corresponding grid spacing for the later time interval (not shown here) is approximately twice as large. Also shown is one side of the cube of nodes, indicated by the four plus signs, that contribute to the interpolation of the fields at the receiver positions.

Figure 2.8a contains the 3D model responses at Station 1 in the form of early time apparent resistivities [*Petry*, 1987], represented by solid lines (for now, ignore the dashed lines). The three simulated transients correspond to different resistivities for the mountain, 500 Ωm, 100 Ωm and 50 Ωm and thus the resistivity contrasts between air and earth of 100:1, 500:1

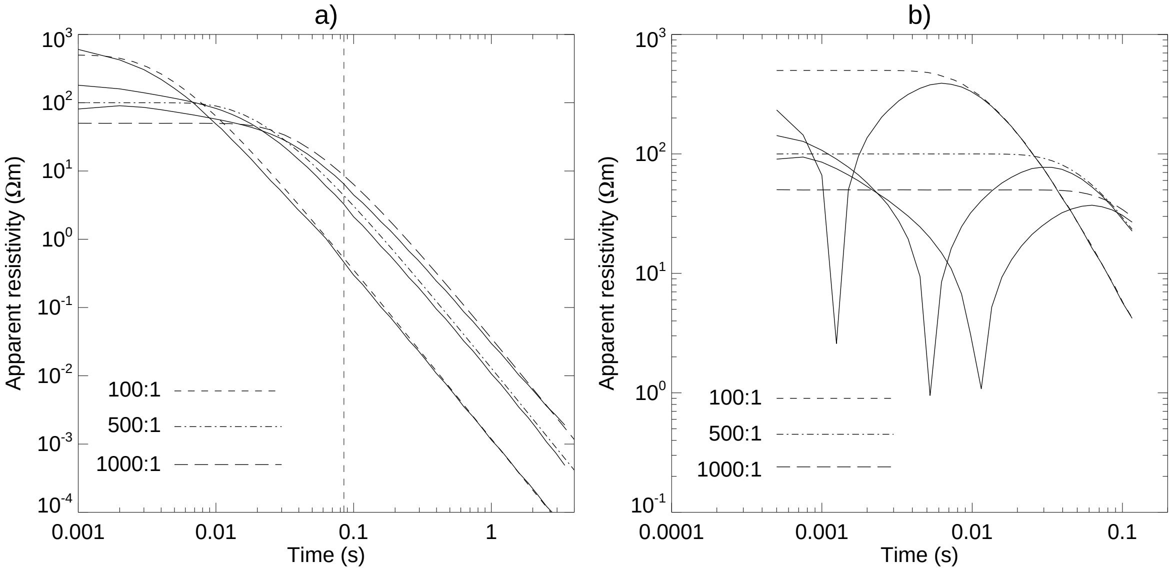

Figure 2.8: *Grid verification results of the 3D volcano model for different resistivity contrasts between a homogeneous mountain and the air space (*$5 \cdot 10^4$ Ω*m) for (a) station 1 and (b) station 6. Solid lines are SLDM solutions, dashed lines are analytical solutions over a flat surface. The three curve pairs in each plot correspond to a mountain resistivity of* 500 Ω*m (contrast 100:1),* 100 Ω*m (contrast 500:1) and* 50 Ω*m (contrast 1000:1).*

and 1000:1, respectively. Each curve is obtained by joining the responses of both employed FD grids, where the vertical line at 0.08 seconds marks the connecting time point. For each contrast, convergence of the SLDM code is achieved. Otherwise, one would observe a significant deviation from the constant decay rate at the latest simulated times for one or both of the employed grids, which would probably occur shortly before 0.1 s or before 3 s.

For the second part of the grid test, the results are controlled to make sure that topographic effects are correctly modeled. In Figure 2.8a each 3D response forms a pair with a dashed curve, which belongs to an analytical half–space response. The half–space resistivity is the same as used for the homogeneous mountain of the corresponding 3D result. The analytical responses are computed at the receiver position Rx1 (Figure 2.7) over a flat surface at an offset corresponding to the horizontal offset of Station 1. According to *Petry* [1987] the late time decay rate of the 1D response shows a time dependence of $t^{-5/2}$. At Station 1 the 3D effect due to topography is an amplitude increase at early times, compared to the 1D curve. This is a combination of the station elevation effect with the response of the conductive mountain [*Hördt and Müller*, 2000]. At later times the amplitude of the 3D curve is decreased compared to the response over a flat surface with a convergence towards the 1D decay rate. Both these effects at early and late times can be observed for each contrast, indicating that both grids model the topography correctly.

This procedure of verifying responses has to be carried out for all FD grids contributing to the forward calculations during an inversion. In the presence of high contrasts it is actually difficult to find a single grid that produces accurate responses for multiple spaciously separated receivers. Thus, in order to maintain stability and accuracy in an inversion of data including multiple separated stations, a separate grid is assigned to each region of the mountain. In practice, in addition to the two grids for the summit stations, three more grids are optimized for the northern, southern and western flanks. The field setup corresponding to Station 7, with its data generated by transmitter Tx2, needs another separate grid. This is due to both the separate transmitter and a different column model with more stress on the approximation of the southern flank's topography, compared to the ones for Stations 1–6. Note that the additional computation time caused by multiple grids represents no major obstacle if a parallel platform is employed in the way described in Section 2.1.2.

As a matter of course, when verifying the grid responses, it has to be taken into account that the topography effects vary between the different receiver stations. In fact, in addition to the summit stations, only Stations 5 and 6 show a significant influence due to topography. For these stations, the mountain is located between transmitter and receiver. The vertical voltage measurements of such a field configuration are usually characterized by a sign reversal as shown by *Hördt and Müller* [2000]. The mountain acts as a conductive anomaly in the air space between the northern transmitter and the southern flank, thereby causing a current concentration with an antisymmetric magnetic field on either side of the anomaly [*Newman*, 1989]. Such signal types cannot be simulated with 1D models, affirming the inevitable modeling of topography.

In Figure 2.8b the grid verification results for Station 6 are compared with the analytical solutions without topography calculated at the location Rx6 in Figure 2.7. Again, the first criterion is fulfilled for each 3D response (solid lines), because no erroneous decay rate can be observed at late times. For a 500 Ωm resistive mountain (contrast 100:1), the sign reversal occurs at the earliest time, compared to the other contrasts. After the reversal, the curve converges to the corresponding analytical solution and decays equally. This is in accordance with the analysis of *Hördt and Müller* [2000] for such a field geometry. The convergence at late times between both 3D and analytical result can also be observed for a 100 Ωm resistive mountain (contrast 500:1), whereas for 50 Ωm (contrast 1000:1) it is only indicated due to the late sign reversal. For this example, the highest contrast 1000:1 thus also represents a border for verifying the 3D response by comparison with the corresponding 1D response.

It can be concluded that the FD grids for the different regions of the mountain yield stable and reasonable responses. In particular the regions with the largest topography effects are crucial for a correct simulation of combined 3D effects due to both the surface terrain and underground structures. The verification of the results for a contrast up to 1000:1 ascertains that stability is maintained for varying models during an inversion.

2.3.5 Results

The inversion scheme's versatility to define arbitrary model parameters led to a variety of inversion attempts in terms of the model parameterization and the number of input data components. The data analysis includes inversions of a single transient measured at the summit (Station 1) and inversions of combined data sets comprising measurements from spaciously separated locations (Stations 1–7). The combined inversions shall be referred to as joint inversions[2], because different magnetic field components are involved. The last inversion is applied to a combined data set, including vertical voltage measurements from the southern flank profile (Stations m28–m42). The goodness of fit of the model predictions d_i^p to the actual data values d_i^o is assessed with the usual weighted least–squares criterion [*Jackson*, 1972]

$$\chi = \sqrt{\frac{1}{N}\sum_{i=1}^{N}\frac{(d_i^o - d_i^p)^2}{\sigma_i^2}},$$

where σ_i is the standard deviation of the ith datum.

Single inversion for horizontal and dome–shaped type of layering

Among the summit measurements, the vertical voltage transient recorded at Station 1 reveals the best data quality together with the longest measurement time range. The transient is characterized by a slow decay in the late–time data, indicating the presence of a good conductor in the underground. The inversion has the main purpose of verifying the existence of a dome–shaped kind of layering with downwards decreasing resistivity, as indicated by the a priori information. For this station, good data fits were achieved with a 1D model [*Müller et al.*, 2002], which also showed the main feature of a resistivity decrease with depth. Hence, the first 3D inversion was carried out under the assumption of a horizontally layered model including topography, as described in Section 2.3.3. The transient was inverted for four layers, thus 7 parameters are involved and define the resistivities and thicknesses of the upper three layers and the basement resistivity. From several test inversions and importance estimations, which are not shown here, it could be concluded that this represents an optimum in terms of data fit and number of important parameters. More layers introduce less resolved parameters; less layers produce a worse data fit.

Figure 2.9a shows the resulting model in a NS–oriented vertical section through the summit. All starting layer resistivities were set to values of 100 Ωm and the initial thicknesses were set to values of 300 m, 600 m and 500 m for the top, middle and lower layer, respectively. Unlike the referenced 1D model, the resulting structure shows no monotonous downwards decrease of the layer resistivities. A low basement resistivity of 1.3 Ωm results from the inversion. Although the initial model response can be improved by the inversion, the final data fit in Figure 2.9b does not reach a satisfying degree. Different values for the starting parameters were used in order to reduce the chance that the result represents a local minimum. However, no further improvements could be achieved. This indicates that the parameterization in the form of a horizontally layered model is not appropriate if topography is taken into account.

The same initial model parameters as for the previous inversion are kept in the second of the above described types of layering, where the layers form a dome–shaped structure. For this and all subsequent inversions, the word layering will refer to such a curved structure. Again, it turned out that four layers are adequate in order to avoid unimportant parameters. Figures 2.9c and d show the resulting model and data fit, respectively. In comparison with Figure 2.9b, the superior data fit indicates that this model parameterization is more adequate

---

[2] The term joint inversion has originally been shaped by *Vozoff and Jupp* [1975] and is typically used for the inversion of data originating from different methods, such as for example MT and DC resistivity soundings.

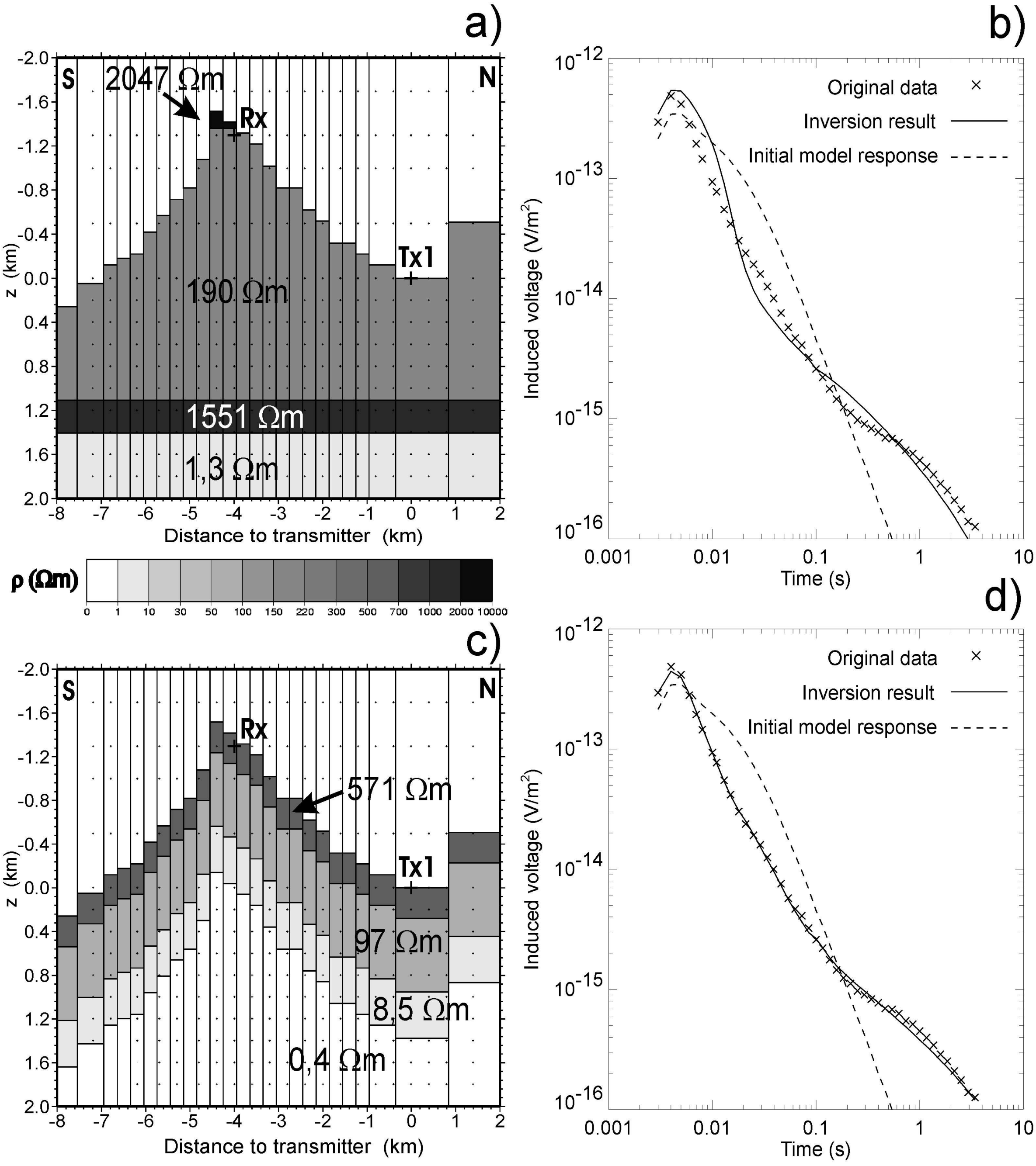

Figure 2.9: *Inversion of a single vertical voltage transient recorded at Station 1. (a) and (b) Resulting model and data fit for a horizontally four–layered mountain, respectively. (c) and (d) Resulting model and data fit for four layers which follow the terrain shape.*

for the underground structure in the vicinity of the summit. In accordance with the a priori information, the resistivity structure is characterized by a strong decrease with depth. The good conductor starts at approximately 950 m depth below the surface with a resistivity of 8 Ωm and a further decrease to 0.4 Ωm at 1380 m.

Joint inversion for a layered structure

With a dome–shaped conductivity structure favored by the previous inversion results, the same parameterization is now used to invert a combined data set. It includes 9 voltage transients distributed over the receiver positions 1–6. An overview of the involved stations is given by Figure 2.10a. Vertical voltages were recorded at all positions. In addition, horizontal voltage components parallel to the transmitter exist for Station 4 and perpendicular to the transmitter for Stations 5 and 6. Figures 2.10b and c show the resulting model and the data fit, respectively. In spite of the small number of model parameters and the large area covered by the receivers, a good data fit is obtained. The vertical components at Stations 1 and 2 and the horizontal component at station 4 are reproduced to a high degree, whereas the other stations are fit in a more qualitative sense. An outstanding result is the reproduction of the sign reversal in the vertical component data of Stations 5 and 6, marked with plus and minus signs in Figure 2.10c. The early time solution for the vertical component at Station 6 is in good agreement with the observed data. However, rather large late time misfits exist for both components of Station 6 and the vertical voltage of Station 5.

For the starting model, each layer thickness is set to an initial value of 500 m, and a homogeneous mountain (100 Ωm) is assumed. The total error χ of the combined data set can be decreased from a value of 53.8 down to 10.3 during 9 iterations. Afterwards, no further relative misfit decrease can be achieved. To generate predicted data for all stations, five different FD grids are employed in order to account for the spacial receiver separation and the late recorded times of Station 1.

From the data fit, it can be concluded that the simple model explains the most important features of the data and represents a good approximation of the resistivity structure over a rough scale outlined by Stations 1–6. The resulting model shows the beginning of the conductive zone at approximately 940 m below the surface. It is very interesting, that both the integrated conductivity of the first two beds and the parameter values below the second layer are in very good agreement with the single inversion result in Figure 2.9c. By means of model variations, involving an extra fictitious layer at the basement, it can be estimated that the highly–conductive zone of 0.4 Ωm is resolved to a depth of approximately 500 m below the beginning of the basement. Because no local deviations from the layered structure are taken into account by this parameterization, the fact that no quantitative data fit is achieved for all transients shows that more information is contained in the data. In particular the slower decay of the observed late time vertical voltages at Stations 5 and 6 indicates a locally more complex conducting underground. Hence, the following inversion attempts assume a layered background with additional model features added.

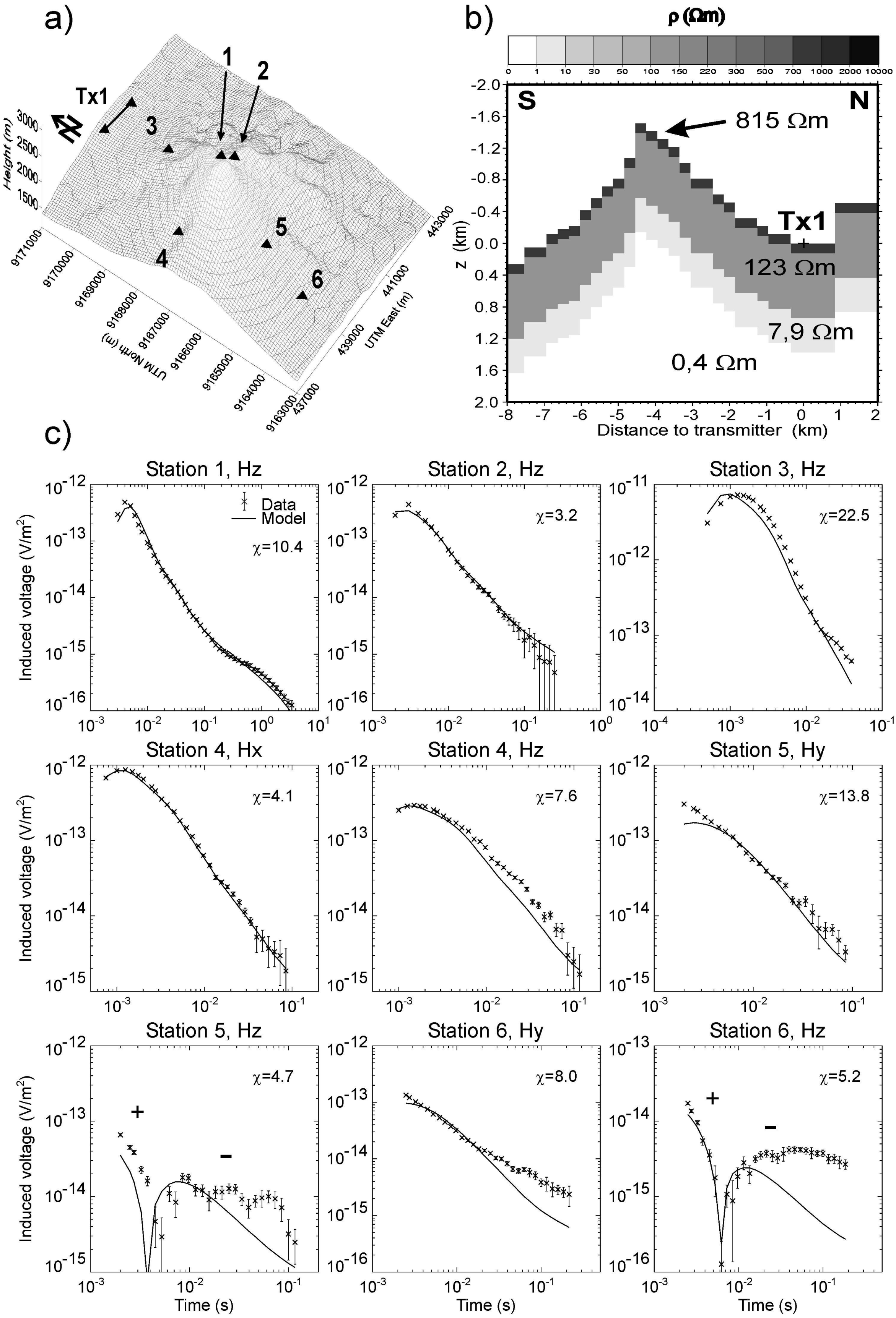

Figure 2.10: *Joint inversion of the combined data set including Stations 1–6 for a dome–shaped four–layered mountain model. (a) Transmitter and receiver positions of the combined data set. (b) Resulting mountain model. (c) Final data fits. The transients are named by the station location and the magnetic component.*

Joint inversion for a layered structure and an additional conductive block

In addition to the parameters describing the four–layered background of the mountain, a rectangular block below the summit is defined in each of the following inversions. The block's position and geometry is kept fixed and its resistivity is treated as another model parameter. Again, the combination of 9 transients is used as input data.

The first inversion attempt is carried out under the assumption of a vertical conduit below the summit. The presence of such a pipe–like structure with a distinguished resistivity is justified by the volcano's permanent activity with a present effusion rate of about 10^5 m^3 per month [*Siswowidjoyo et al.*, 1995]. The conduit is represented by a column–shaped block with a fixed geometry, embedded in the four–layered background and extends downwards beyond the estimated border of resolution. Its horizontal extension is 1×1 km^2. The layer parameters are neither initialized to the values of the previous inversion result nor kept fixed, because the additional structure is likely to influence the layered background during the inversion. For the layers, the same starting parameters as in the previous inversion are used. The additional model parameter, the block's resistivity, is initialized by a value of 10 Ωm in order to account for an assumed higher conductivity due to (partial) melts. The final model is shown in both a NS–oriented and a WE–oriented section in Figure 2.11a. A resistivity of 52 Ωm results for the additional pipe. The layered background below a depth of approximately 1000 m under the surface is similar to the result in Figure 2.10b. No increased data fit compared to the combined inversion without an additional block can be achieved. The result produces an error of $\chi = 11.7$, where no visible differences to Figure 2.10c for each separate component exist. The relative misfit decrease converges to zero after 6 iterations.

The second inversion attempt of this kind involves a block representing a superficial magma chamber at approximately 500 m below the summit. Its existence is suggested by the seismological investigations of *Ratdomopurbo and Poupinet* [1995], who show a zone with anomalously high attenuation of seismic waves 1–2 km below the summit. Also, according to *Camus et al.* [2000], the eruption history of the period starting at the end of the 18th century suggests such a reservoir. First, the more or less continuous growth of summit domes interrupted by collapses and phases of quiescence would match the idea of a continuously depleted and refilled magma reservoir at a small depth. Second, the absence of large ignimbrite[3] eruptions renders the alternative of a large deep reservoir instead of a shallow one less possible [*Camus et al.*, 2000]. The block geometry is chosen to be $2 \times 2 \times 2$ km^3 and is initialized to a value of 10 Ωm. The resulting model in Figure 2.11b reveals a rather resistive reservoir. Similarly to the previous result, no real improvement of the data fit can be achieved by this approach. Here, a final error of $\chi = 11.5$ results after 10 iterations, using the same starting parameters as before. Another attempt not shown here placed the block 1 km southwards from the position shown in Figure 2.11b, yet no further misfit decrease could be achieved as well.

---

[3] The rock formed by the widespread deposition and consolidation of ash flows and Nuees Ardentes. It is characterized by an inhomogeneous composition in terms of the grain size of its constituents [*Matthes*, 1990].

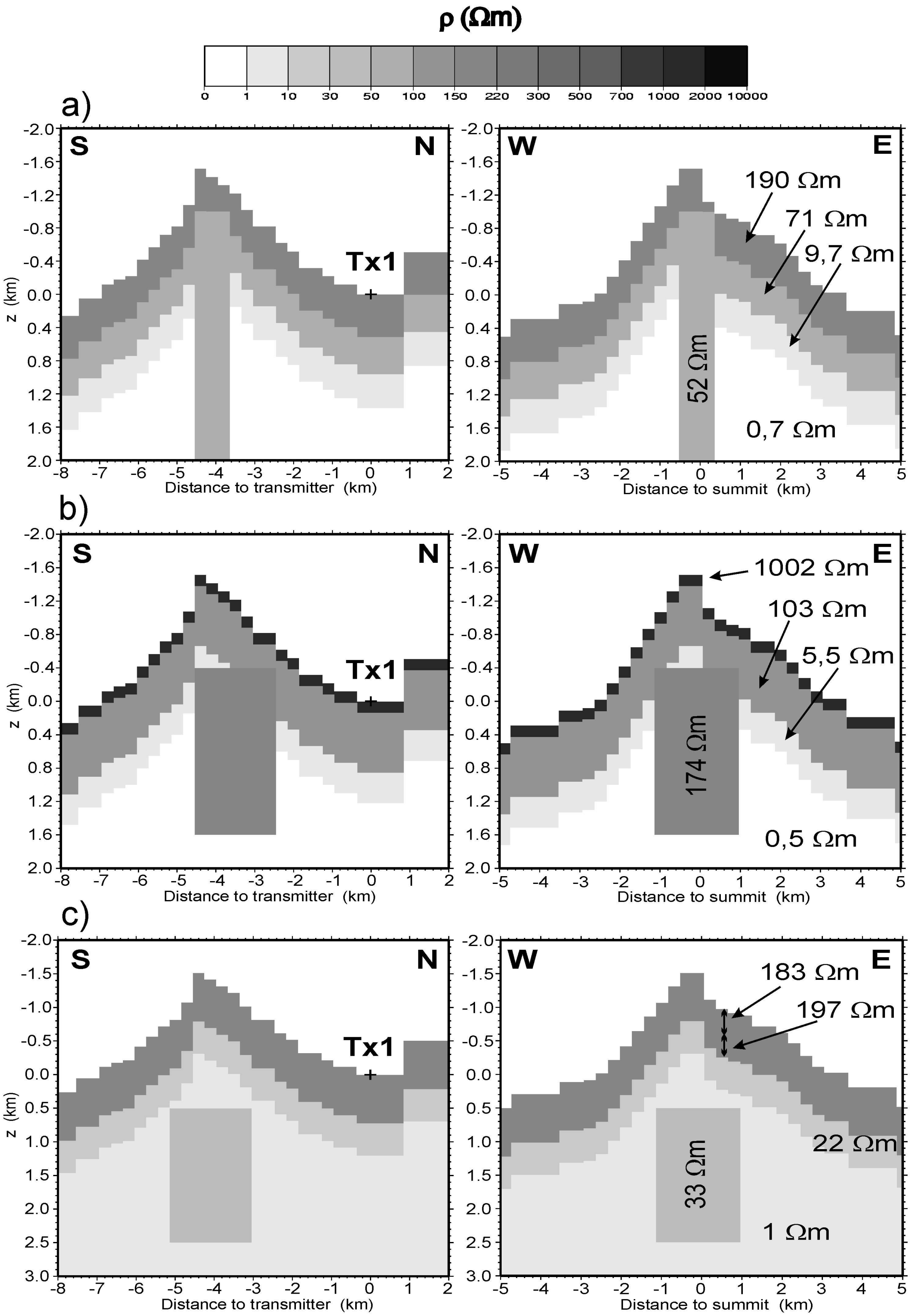

Figure 2.11: *Model results from joint inversions of the combined data set (Stations 1–6) for a dome–shaped four–layered mountain model and an additional block below the summit. The block represents (a) a vertical conduit, (b) a shallow magma reservoir and (c) a deep magma reservoir. Note the larger vertical scale in (c).*

In the last inversion, a $2 \times 2 \times 2$ km^3 extended block is placed at a depth of approximately 2 km below the summit. Such a deep structure is likely to be hidden by the conductive basement of the volcano, which has been confirmed by all previous inversions. Nevertheless, this attempt is carried out in order to investigate, if a deep reservoir with conductivities different to the basement can improve the data fit. This could be interpreted as a deep magma reservoir. However, like in the preceding attempts, the inversion result shown in Figure 2.11c, obtained after 6 iterations, does not provide an improved data fit. The final block resistivity of 33 Ωm contrasts with the 1 Ωm basement. Compared to all previous joint inversion results, the error of $\chi = 12.2$ reveals a slightly worse fit, yet again with no significant difference to Figure 2.10c for the misfit of each separate transient.

All three inversions confirm the monotonous decrease of the resistivity with depth. However, there exist rather large differences between the parameters for the upper two layers. In contrast, the third layer's thickness and resistivity and the basement resistivity are similar for each inversion result. This indicates a higher resolution of these layer parameters, compared to the upper two layers. Further, it can be concluded that the additional blocks are not relevant for an enhancement of the data fit, although this does not negate the existence of a shallow or deep reservoir. Due to the constant activity of Merapi, it is likely that regions of (partial) melts exist below the summit. However, the block resistivities resulting from all three inversions appear too large for molten material, because this should involve values known to be in the range of approximately 1–20 Ωm [*Lénat*, 1995]. Either the assumed reservoirs cannot be distinguished by resistivities contrasting with the background or the spatial distribution of melts inside of the volcano is far more complicated than represented by such simple block models.

Joint inversion for a layered structure with fault

The following inversion involves an additional vertical voltage transient measured at Station 1 yet produced by the southern transmitter (Tx2 in Figure 2.3), thus the joint data set now includes 10 transients. The additional data component, referred to as Station 7, expands the resolution of the inversion domain into the southern direction. Its inclusion in the joint data set is motivated by the question whether data from the southern transmitter can also be reproduced by a four–layered model. The inversion involves a separate FD grid for the simulation of Station 7, in addition to the five grids used for Stations 1–6, in order to account for the different transmitter and the proper modeling of the southern topography. Figure 2.12a shows the model of the inversion result. Figures 2.12b and c show the observed and predicted data for Station 7 and Stations 1–6. Comparing the errors χ for each separate data component with the corresponding data fits resulting from the inversion without Station 7 (Figure 2.10c), one observes a slightly worse data fit for the majority of Stations 1–6. In particular the horizontal component of Station 4 shows a much worse fit in the early time part. Moreover, the data of Station 7 cannot be reproduced to a satisfying degree. Other attempts with varying starting model parameters also failed to achieve a better data fit as shown in Figure 2.12. It is obvious that the number of parameters is too small for the enlarged inversion domain. The poor data fit of Station 7 suggests a more complicated resistivity structure below the southern flank.

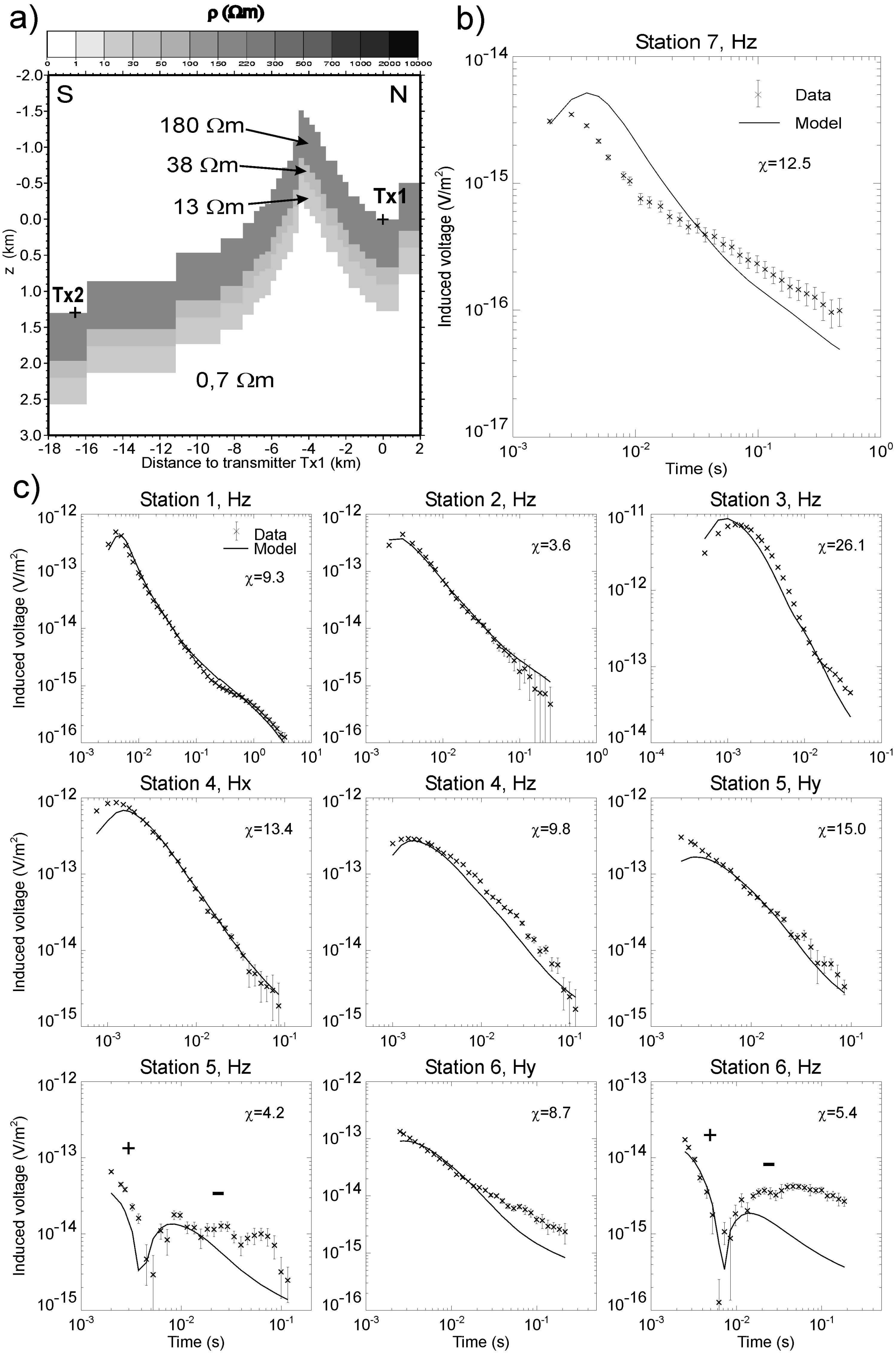

Figure 2.12: Model results from a joint inversion of the combined data set including Stations 1–7 for a dome–shaped layered mountain model with four layers. (a) Final model result. (b) Final data fit for Station 7. (c) Final data fit for Stations 1–6.

In order to define appropriate additional model parameters, 1D inversion results of both LOTEM and in–loop measurements on a profile on the southern flank are employed. A 2D pseudo–section obtained from 1D LOTEM joint inversion results [*Kalscheuer*, 2003] is shown in Figure 2.13. It reveals a clear transition between the UTM coordinates 9159 km and 9160 km to a more shallow good conductor on the southern part of the profile. Evidence for such a strong lateral resistivity change close to the UTM coordinate 9159 km was also given by the more shallow 1D resistivity sections obtained from in–loop data [*Koch*, 2003]. However, it can be expected that the 1D inversions provide only poor a resolution of the lateral structure. Nevertheless, the layer parameter set is extended by introducing a WE–oriented fault plane below the southern flank. The plane divides the inversion domain into two separate layered sections and is chosen to be located at the northern UTM coordinate 9159 km (Figure 2.13). This is approximately 7.5 km south of Merapi's summit. North of the plane, the four–layered structure is kept, whereas three layers are used for the southern model section. The combination of 10 voltage transients are thus inverted for altogether 12 layer parameters.

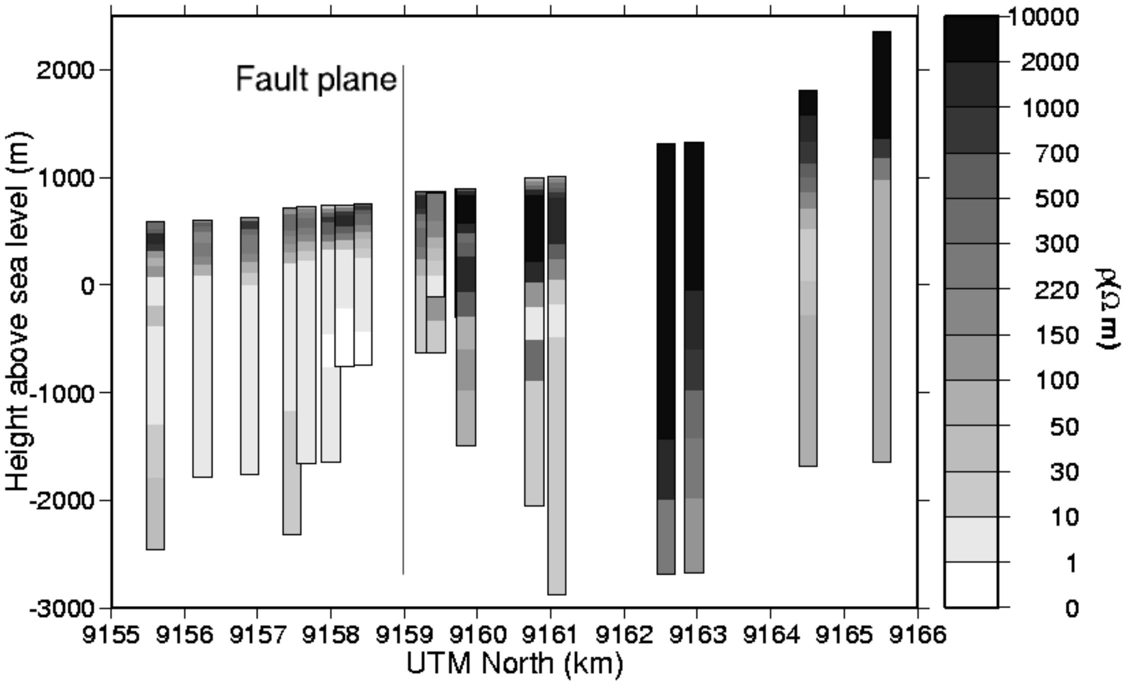

Figure 2.13: *2D pseudo section from 1D inversion results of a southern flank profile [Kalscheuer, 2003]. The 1D Occam inversion results are shown for each station with respect to its elevation on the profile.*

Figure 2.14a both illustrates the parameterization and shows the inversion result. First, a very distinct difference between the resulting model sections can be observed, indicating the necessity of the additional parameters. Comparing the northern section with the inversion result in Figure 2.10b, one observes only minor differences below the second layer, whereas larger deviations can be seen for the upper two layers. Nevertheless, the monotonous resistivity decrease with depth down to a value of 0.7 is in good agreement with all previous inversion results. A minor decrease in the goodness of fit can be revealed from comparing the separate

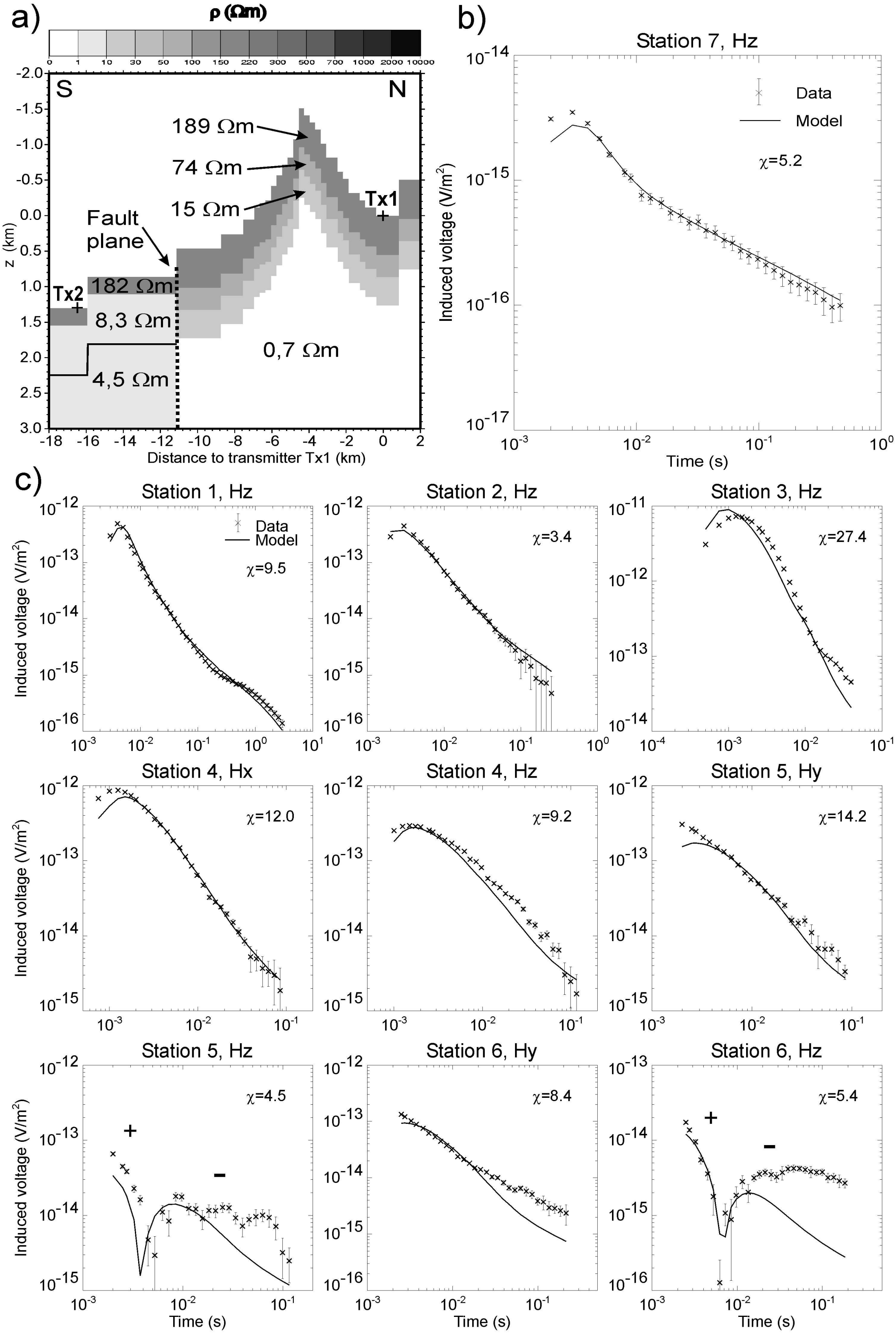

Figure 2.14: Model results from a joint inversion of the combined data set including Stations 1–7 for a dome–shaped layered mountain model with a fault plane below the southern flank. (a) Final model result. (b) Final data fit for Station 7. (c) Final data fit for Stations 1–6.

data fits and its errors χ in Figure 2.14c with the corresponding fits in Figure 2.10c. Here, a total error of $\chi = 12.0$ (previously $\chi = 10.3$) results for the entirety of data belonging to Stations 1–6. This is mainly caused by a worse early time data fit for Station 3 and the horizontal component of Station 4. Due to its distance, the direct influence of the fault can be expected to be very small on both Stations 3 and 4. The poorer fit is thus caused by the altered upper layers of the northern section. The poor vertical component's late time data fit of Stations 5 and 6 is not improved by the additional model parameters.

Compared to the previous approach without a fault structure (Figure 2.12), the inversion result represents a high improvement due to the superior data fit of Station 7 (Figure 2.14b). The only significant misfit can be observed at the earliest times. Probably, the early time fit could be improved by a more resistive overburden, similar to the one shown in Figure 2.10b. This is suggested by comparing the horizontal component's data fit of Station 4 in Figure 2.10c with the corresponding fit in Figure 2.14c, where a similar early time misfit can be observed due to the less resistive overburden.

The inversion result includes two important aspects. *Mitsuhata et al.* [2002] showed that the joint use of synthetic data generated by a left–side source and a right–side source significantly improves the resolution of the underground between both sources. This could also be confirmed by comparing 2.5D joint inversion results of field data generated by such a transmitter setup with the results from a single source. A better agreement with a model obtained by a MT survey could be observed when inverting the data from both sources. In the case of the presented inversion, the two transmitters are located similarly with respect to the inversion domain below the volcanic edifice. Hence, an increased resolution of the four–layered part of the model is given compared to the joint inversions involving a single transmitter. This makes the result in Figure 2.14a more important. The presence of a highly conductive zone (< 1 Ωm) below a layer of intermediate conductivity, here it is 15 Ωm, is confirmed because of the good agreement with the inversion result from Figure 2.10b, where only the northern transmitter is involved.

Another outstanding result is the very good agreement of the southern model section with the resistivity structure derived from 1D joint inversions. The southern section of the inversion result is characterized by a more shallow conductive layer below an approximately 250 m thick overburden. The small difference between the resistivities of the intermediate layer and the basement indicate a two–layered structure in the southern section. This is in accordance with the pseudo section in Figure 2.13, where the two–layered structure south of the UTM coordinate 9159 km is dominated by a shallow conductor with resistivities mainly below 10 Ωm.

Inversion for the position of a conductive block in a homogeneous half–space

The data inverted in the following originate from the southern flank profile given by Stations m28–m42 and the transmitter Tx3 (see Figure 2.3), also called the "Kaliadem"[4] profile. A closer view of the field setup is shown in Figure 2.15. First, it needs to be emphasized that the following inversion is a rather experimental approach without the primary aim of achieving a realistic earth model. This has several reasons. Earlier interpretation attempts for these measurements were made by *Müller* [2000*b*] using 3D forward modeling. His results indicate a far more complicated resistivity structure than can be taken into account by the limited model complexity allowed by SINV.

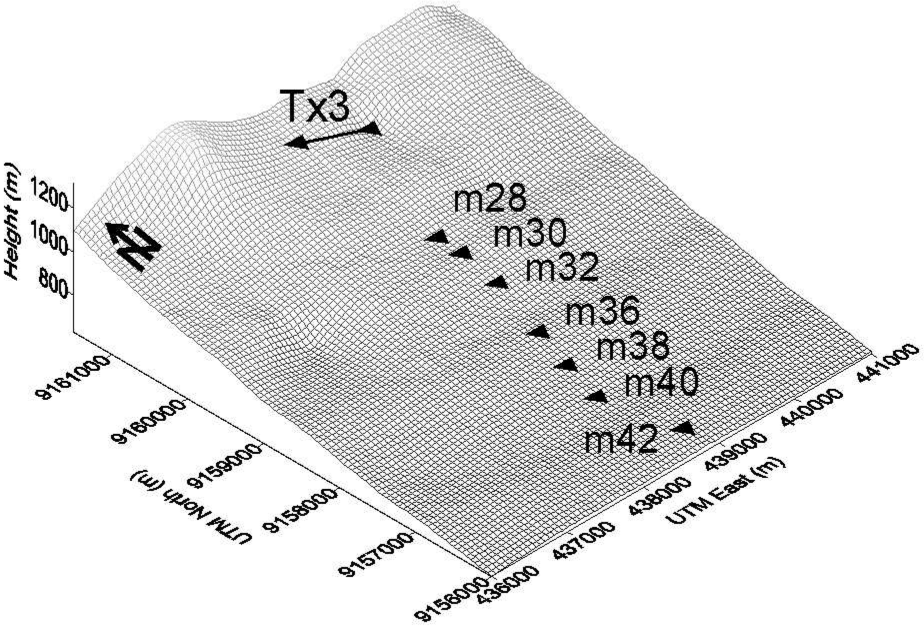

Figure 2.15: *Transmitter and receiver positions of the stations m28–m42 located on Merapi's southern flank.*

Another reason which makes the inversion of the Kaliadem data a challenging task is the data quality. Unfortunately, the profile was located in a region with a very high noise influence due to the local power supply. Therefore, even after applying rather sophisticated filter techniques [*Scholl*, 2001] to the recorded transients, the processed data from this region is still characterized by a significant portion of noise [*Müller*, 2000*b*; *Kalscheuer*, 2003]. The measurements are vertical voltages and are shown by the cross symbols in Figure 2.16. It can be seen that the noise influence appears in the form of sharp deviations of single data points from an otherwise smooth transient.

All stations are characterized by double sign changes, with the exception of Station m28, where a single reversal exists. The sign of the measurements is indicated by either '+' or '-' above the data curves in Figure 2.16. The determination of the correct sign of the data can become difficult if this is not correctly taken into account during the survey. Unfortunately,

---

[4] The transmitter Tx3 (see Figure 2.3) was located in the small village of Kaliadem on the southern flank.

the axis orientation (upwards or downwards) of the wire loop used for measuring the vertical voltage was not considered during the measurements. Hence, the correct sign of the data cannot be determined. Following *Müller et al.* [2002], each transient is assigned to the same sign at early times, because the reversals show a consistent behaviour in the sense that there are no rapid variations in shape along the profile.

One notices that no data errors are shown in Figure 2.16. Because of the poor data quality, the data processing reveals a high average value for the standard deviations. The errors are even above the average for the data points belonging to the sign changes. Weighting the data by the original standard deviations leads to inversion results that do not reproduce the sign reversals, because of a too small influence of the corresponding data points. Therefore, the presented inversion involves an equal weighting by assuming a relative error of 1 % for each datum. As mentioned in Section 2.1.2, a data transformation using the Area–Sinus–Hyperbolicus function is employed in order to account for the changing sign. Refer to *Scholl* [2001] for a description about the corresponding transformation of the data errors.

The consistent sign reversals at all stations indicate strong effects due to 3D structures. The first 3D modeling attempts tried to explain the reversals by the topography [*Müller*, 2000*b*]. The local terrain is dominated by approximately 50–100 m deep canyons located roughly parallel on either side of the profile. *Müller* [2000*b*] investigated the influence of the canyons by approximating them with 3D blocks. However, neither a very resistive canyon due to the air space nor a conductive canyon, based on the assumption of fluid concentrations in the valleys, could reproduce any sign changes. Approximating the profile's topography with the more accurate vertical column approach could also not reproduce any sign reversals. Moreover, including the topography showed only a marginal influence on the predicted data. Hence, the following analysis involves an earth model without topography.

The starting model used for the inversion is based on the 3D modeling results from *Müller* [2000*b*]. Although no quantitative fit to the data could be achieved, he concluded that a 1 Ωm conductive WE striking block close to the surface in the northern part of the profile seems to be the most likely explanation for the observed reversals (see also *Müller et al.* [2002]). The anomaly is located between Stations m30 and m32 which is supported by MT measurements [*Haak*, 1998] on this profile. The induction arrows for a period of 0.2 seconds point northward north of Station m30 and southward south of Station m30, indicating a good conductor below the station. The anomalous block reaches the surface with a vertical extent of 100 m and a width along the profile of 1 km and a lateral extent of 4 km. The 500 Ωm background has an additional conductive layer of 20 Ωm with a thickness of 1000 m at 500 m depth. With that model, a single and a double sign reversal can be simulated at Stations m36 and m40, respectively.

The presented inversion attempt starts from a similar model guess. Here, importance is attached to the question whether a single 3D structure can cause the consistent sign reversals over the profile. Therefore, without intending to model the true background resistivity structure, a homogeneous 500 Ωm background is assumed. According to the 1D joint inversion results from *Kalscheuer* [2003] shown earlier in Figure 2.13, the southern flank reveals no such resistive background below the Kaliadem profile. Furthermore, the inversion result of Figure 2.14a is in contrast to a homogeneous background.

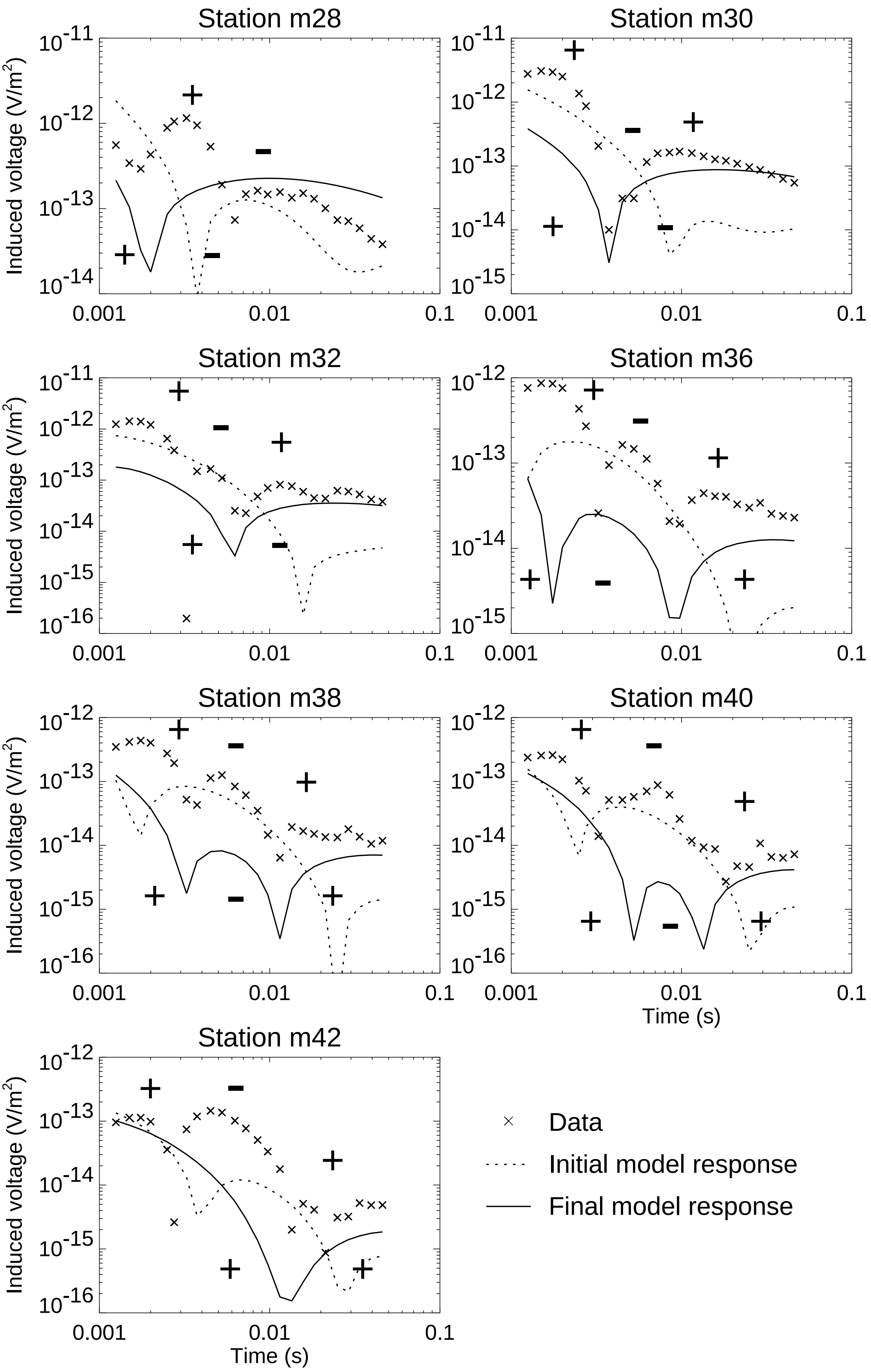

Figure 2.16: *Combined inversion of Stations m28–m42. Observed data with both initial and resulting model response. The upper and lower signs correspond to the signs of the observed and predicted data, respectively.*

Figures 2.17a and b show the block's geometry and position in a plan view and in a profile–versus–depth section, respectively. For simplicity, the transmitter's angle of inclination (approximately 10°) to the WE direction is neglected. The dashed lines represent the initial model and the solid lines represent the block's position after an inversion, where both resistivity and geometry remain fixed, yet the position is variable. The size of the 1 Ωm conductive block is chosen to be $4 \times 0.5 \times 4.8$ km^3 for the WE, NS and vertical extension, respectively. The vertical extension is much larger than assumed by *Müller* [2000*b*] and is based on the observations of the mentioned MT study. Sign reversals can be simulated at each station by the initial block position, although the time of occurrence is not matched for most of the stations.

Two free position parameters are allowed. The first parameter defines the position on the axis parallel to the NS direction, and the second one describes the vertical position. In the initial model the block starts at a depth of 150 m below the surface, and the northern edge is at a distance of 500 m south from the transmitter. Compared to the initial position, the inversion shifts the block 50 m closer to the surface and approximately 200 m closer to the transmitter. Due to the strong constraints on the model complexity, a data fit increase could be achieved within only two iterations.

In Figure 2.16 the solid curves show the data calculated from the inversion result and the dashed curves show the initial model response. Both initial and final model response fail to reproduce the correct amplitudes for most of the data. This is likely to be caused by a wrong assumption about the background resistivity. Another aspect to be considered are amplitude shifts due to possible local near–surface conductors below the grounded–wire source. As described in detail by *Newman* [1989], a conductor close to the transmitter causes a shift from the voltage amplitude level arising from the host. Depending on the location of the transmitter with respect to the near–surface conductor, the response that is observed can be shifted above or shifted below the host response. *Newman* [1989] shows that such effects can be removed to a large degree by scaling the amplitude of the predicted data by an adequate constant. Therefore, if an erroneous amplitude is assumed to be caused by a conductor close to the transmitter, the amplitude deviations are less critical.

More crucial is the question whether the times of the sign reversals are matched by the predicted curves, because this is influenced by the conductive block between transmitter and profile. In Figure 2.16 the lower signs in each plot mark the sign of the predicted data. The small parameter change between initial and final model has a relatively strong impact on the simulated data. At Station m28 the inversion moves the sign change of the initial model towards earlier times. This might be enforced by the observed early time data. It is characterized by a strong amplitude decrease during the first data points, yet without changing the sign. The double sign reversal at Stations m30 and m32, with a narrow intermediate negative data part, cannot be reproduced. However, for both stations the simulated single reversal occurs at a time that is in more agreement with the observed data than the reversal time of the initial response. The occurrence of the predicted double sign changes at Stations m36, m38 and m40 are in much better agreement, compared to the initial response. However, for Station m42 the two sign reversals, already reproduced by the initial model, vanish for the new position of the block. In general, the inversion result produces an improved data fit. The

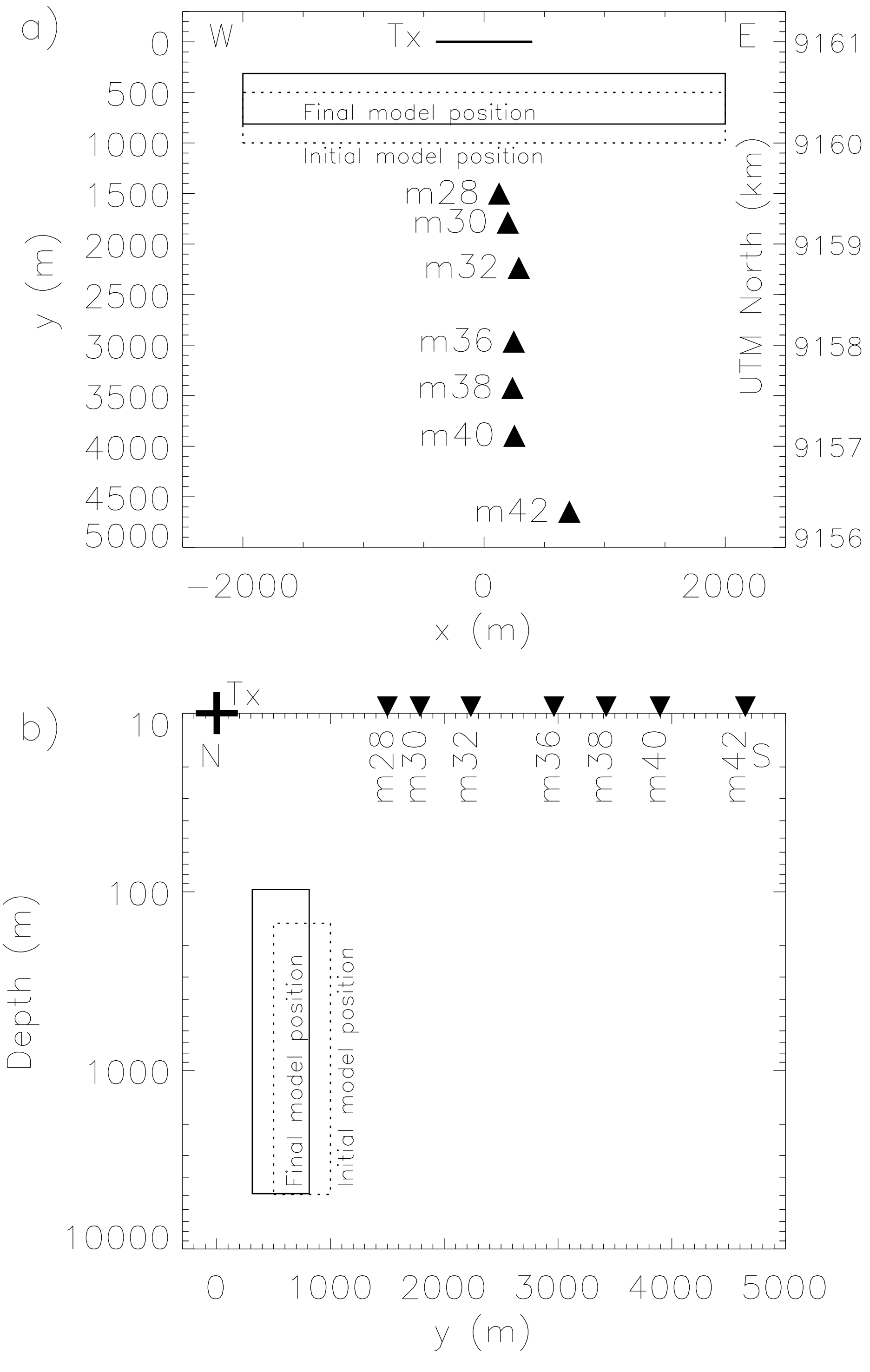

Figure 2.17: *Initial and final model producing the corresponding responses in Figure 2.16. The model parameters are represented by both the lateral and vertical position of the WE–oriented conductive block. The initial and final model are shown in (a) a plan view and (b) a vertical section along the profile.*

total error is decreased from an initial value of $\chi = 73.7$ to a final value of $\chi = 21.7$ during the inversion. This mainly results from the shift of the predicted sign changes towards the observed reversal times.

To draw a conclusion, the inversion attempt successfully demonstrated the versatility of SINV by the capability of adapting the model parameterization to difficult inversion problems. The simplified model of a complex structure can be enhanced if an appropriate parameterization is chosen. However, the inversion result fails to reproduce both the correct number of reversals for Stations m30, m32 and m42 and the exact shape of the curves for all stations. This shows that the real resistivity structure is much more complicated, perhaps a more complex system of several conductors interacting with each other. Inverting for such a model would require a much larger number of parameters.

More complications might arise from the presence of pipelines in the survey area, used for the local water supply. Their existence had been confirmed by the local inhabitants during the measurements. However, mapping the true positions turned out to be too difficult due to the lack of sufficient information. Most pipelines are oriented in a NS direction and a few are oriented in a WE direction. To study pipeline effects with EM forward modeling codes, one usually uses blocks or thin sheets such that the product of conductivity and area of the block's cross section approximates the corresponding product for a highly conductive pipe [*Kriegshäuser*, 1991; *Hördt*, 1992; *Tezkan*, 1993]. Here, no sign reversals could be reproduced for any station by placing an elongated conductive block, representing a pipe, in a direction perpendicular to the transmitter. Different locations on the WE–oriented axis were tried for such a pipe model. *Kriegshäuser* [1991] showed that strong distortions in the form of sign reversals are due to pipelines with an orientation parallel to the transmitter and located close to the receiver. Such could also be the case on the Kaliadem profile, although two reasons negate the assumption that the data is dominated by pipeline effects. First, the above mentioned MT study, employing a period of 0.2 seconds, indicates a conductive anomaly in a much larger depth than typical for pipelines. Second, sign reversals usually occur if the receiver is located very close to a pipe, as also shown by *Hördt* [1992], which is unlikely to be the case for each receiver of the profile.

2.3.6 Interpretation and conclusions

In comparison with both MT [*Müller*, 2000*a*] and DC geoelectrical measurements [*Friedel et al.*, 2000], the LOTEM data provides a greater insight into the underground below the volcanic edifice due to a better data covering of the summit region. Also, the exploration depth fills the gap between large–scale MT and shallow DC resistivity soundings. The general structural resistivity image of the volcanic edifice, obtained from the presented inversions, is in good agreement with the trends indicated by both mentioned disciplines.

The most important result is the confirmation of the existence of an extensive conductive zone below the volcanic edifice. The volcano models were constrained such that the layered beds closely follow the topography. Probably there exist deviations from this simplified structure, because some data components show significant misfits or can only be explained to a qualitative degree. However, an upwards–directed curvature in the resistivity structure can be regarded as confirmed. In particular the superior data fit of the summit Station 1 that is obtained with a dome–shaped layer structure, compared to the fit given by horizontal beds, affirms an upwelling of conductivity sources below the summit. In order to obtain a rough error estimation of the parameters characterizing the conductive zone, the presented inversion results involving a curved layered background are compared. This reveals a constant image for the lower conductive zone below the volcano. To quantify, mean values and its standard deviations are used. The bed of intermediate resistivity (the third layer) starts at a depth of 918 ±50 m with a thickness of 407 ±23 m and a resistivity of 9 ±3 Ωm. The basement resistivity has a mean value of 0.5 ±0.1 Ωm. The upper layer parameters reveal the largest differences between each other, because the LOTEM data does not provide measurements at times which are early enough to resolve the shallow structure. Nevertheless, a strong monotonous resistivity decrease, starting from a rather resistive overburden, can be concluded with some ambiguity from the different inversion approaches. This is also a major conclusion drawn from DC resistivity imaging along the volcano's flanks [*Friedel et al.*, 2000]. *Müller et al.* [2002] propose a 1000 Ωm resistive basement below the good conductor, based on 1D inversions of data measured during the first LOTEM survey in 1998. However, the monotonous resistivity decrease affirmed by the presented results rather indicates a connection with a local anomaly of low conductivity below Merapi observed on a regional scale by a MT survey across Central Java [*Ritter et al.*, 1998].

The results support the existence of a large hydrothermal system inside of the volcano, because fluids seem to be the main cause for the extensive region of high conductivity. The alternative explanation by a large magma reservoir is unlikely if one takes the measurements of other disciplines into account. First, tilt and DGPS[5] data give no evidence for a large magma chamber in altitudes higher than 1000 m below Merapi's surface [*Rebscher et al.*, 2000]. Also, large amounts of magma would not match density estimations obtained from gravimetric measurements [*Gerstenecker*, pers. comm]. The other possibility of sea water intruding from the ocean is not supported by the regional MT profile across Central Java [*Ritter et al.*, 1998]. Moreover, the isotopic analysis of the fumarolic water at the summit shows that the main water component is rainwater with a small magmatic fraction [*Zimmer and Erzinger*, 1998].

Müller et al. [2002] assume fluid resistivities of 0.2–1 Ωm in order to obtain estimated porosity values ranging from 10 to 20 % for the conductive zone below the flanks. Such high porosities are indeed supported by gravity observations [*Setiawan*, 2002]. However, they cannot be the cause for the high conductivities below depths of 900 m, because this would require even higher porosities. Actually, the contrary effect of a downwards increased resistivity should occur due to the bulk porosity decreasing with depth by compression of cracks and pores [*Ryan*, 1987]. *Lénat* [1995] mentions departures from Archie's law in connection with experiments on Hawaiian and Icelandic basalts, where lower than expected resistivities are explained by the presence of hydrated minerals such as clay minerals or zeolites. Even if not clearly identified by geophysical observations, (partial) melts must be present due to Merapi's constant activity. Hence, the heat is likely to generate a circulation of hydrothermally altered fluids with concentration processes in the volcano's central part. The significant upwelling of conductivity sources derived from the inversion results supports the idea of a vertical fluid transport.

There exist contrary views about the existence of a shallow magma reservoir. As mentioned

---

[5] Differential GPS (Geo Positioning System).

before, *Camus et al.* [2000] relate the quasi–steady magma output to the presence of a small superficial reservoir. Also, the seismological observations of *Ratdomopurbo and Poupinet* [1995] support an aseismic zone related to a shallow magma chamber. On the other hand, other seismic data [*Wassermann et al.*, 1998] and deformation measurements [*Westerhaus et al.*, 1998; *Beauducel and Cornet*, 1999] do not show a clear indication of an aseismic zone. The presented LOTEM data analysis neither supports a vertically extended conduit nor a shallow or deep reservoir distinguished by a very low resistivity. However, since the resistivity of molten lava is known to range from about less than 1 to 20 Ωm [*Lénat*, 1995], a reservoir below the zone of high conductivities, approximately 900 m, might well be hidden in the layered host. This however would be beyond the resolution capabilities of the LOTEM method. Apart from the presented block–like model ideas for the structure of a possible reservoir, a more complicated distribution of the melts over a system of dykes may exist in reality.

The clear transition to a different resistivity structure below the foothills of the southern flank indicates that conductivity sources may be different compard to the summit area. At greater distances from the summit, fluids that must not be directly related to the hydrothermal system and thus not enriched by hydrated minerals may be the most likely cause for the shallow conductivities. The mentioned regional MT study revealed other shallow conductors of this kind at several places in Central Java. The shown inversions involve an approximation of the transition by a vertical fault. The question about its true structure is especially worth further investigation in conjunction with the known southern conductivity anomaly observed over the Kaliadem profile. This anomaly has been observed by LOTEM measurements [*Müller et al.*, 2002], CSAMT[6] data [*Supriadi et al.*, 2000] and Central–Loop data [*Koch*, 2003] and coincides spatially with the assumed position of the vertical fault in Figure 2.14a.

The analysis of the Kaliadem profile demonstrates that TEM measurements with strong distortions in the form of sign reversals represent a highly complicated inversion problem. Because of the limitation of the spatial data distribution to a profile instead of an area, a 2D inversion capable of inverting for a finely parameterized underground is a more appropriate approach for this kind of data. The further analysis of the Kaliadem profile is the subject of ongoing research [*Kalscheuer*, 2003]. A final clarification about the anomaly's geometry and interaction with the background resistivity structure would be possible with an area–wide distribution of measurements available, thus enabling the application of a large–scale inversion as presented in Chapter 4.

---

[6] Controlled Source Audio Magnetotellurics.

CHAPTER 3

A PARALLEL FD SCHEME FOR 3D TEM MODELING WITH NON–CAUSAL SOURCES

The previous chapter demonstrated how an efficient data analysis can be realized using 3D earth models with a low degree of complexity. A great advantage is given by the fact that no large amounts of data distributed over the target are required. On the other hand, sufficient prior knowledge about the target is needed in order to define appropriate parameters of a model such that its main structural features can be refined by an inversion. In many cases, no such prior knowledge might be present. As a consequence, an extensive data acquisition with an area–wide distribution of sensors cannot be avoided in order to provide a sufficient resolution of the underground. Such cases are typical in mineral exploration [*Nabighian and Macnae*, 1991], hydrological and hazardous waste site characterization [*Pellerin and Alumbaugh*, 1997] or general geological mapping.

The inversion of large data sets collected over a 3D earth with an unknown and extremely complicated structure leads to the necessity of adequately fine model parameterizations. Such an imaging scheme will be developed in the course of the following two chapters. It will be outlined in more detail in Chapter 4 how the scheme is based on the principles of seismic wavefield imaging methods, also known as migration. For now, it shall only be emphasized that migration techniques involve the evolution of causal source fields induced simultaneously by multiple spatially distributed sources, where both electric and/or magnetic source types are considered. Furthermore, the source excitation continues during propagation of the EM fields over the whole simulation time range. These fields will later be referred to as residual fields and cannot be simulated by the SLDM code of *Druskin and Knizhnerman* [1988].

Therefore, an explicit finite–difference (FD) 3D time–stepping scheme for the simulation of EM fields is developed in this chapter. FD schemes have been used extensively, for their great simplicity in solving multidimensional time–domain modeling problems for controlled sources. Among the first approaches for EM modeling, *Goldman and Stoyer* [1983] addressed the simulation of time–domain responses in a simplified axially symmetric media with an implicit and 2D FD formulation. Later a quasi–3D approach, where 3D shapes were realized by a straight circular cylinder embedded in a 2D background, was presented by *Tabarovsky and Rabinovich* [1988]. A simulation of TEM surveys over thin vertical conductors embedded in a half–space with overburden was described by *Oristaglio and Hohmann* [1984]. Their numerical method for solving the 2D transverse electric mode of Maxwell's equations is based on an explicit FD scheme originally proposed by *DuFort and Frankel* [1953] and generalized to inhomogeneous models and irregular grids. *Adhidjaja and Hohmann* [1989] attempted to develop a direct time–domain, FD solution for the EM response of 3D models. Their solution is formulated in terms of secondary magnetic fields to avoid dealing with a discontinuous normal component of the electric field, yet faces problems with discontinuous conductivity gradients at interfaces. *Wang and Hohmann* [1993] presented an explicit 3D FD scheme for loop sources that employs a modified version of the DuFort–Frankel method. The solution incorporates analytical impulse responses from an assumed homogeneous earth model as initial conditions. Their scheme employs a staggered grid, which was originally described by *Yee* [1966] and represents a suitable method for the spatial discretization of Maxwell's equations.

The development of the presented FD algorithm involves reviewing the theory of Maxwell's equations for 3D heterogeneous media and the time–stepping scheme of the equations by using a staggered–grid in conjunction with a modified version of the DuFort–Frankel method. The time–stepping scheme and stability criteria are based upon the solution presented by *Wang and Hohmann* [1993]. However, there are differences in several key aspects. First, the algorithm is extended to provide the capability of simulating non–causal source fields. Furthermore, the capability of simulating field responses due to multiple electric and/or magnetic sources is provided by the algorithm. This is required by the migration techniques involved in the inversion presented in Chapter 4. Second, the initial conditions are computed for an arbitrarily complex geological media. This involves the solution of a 3D Poisson problem prior to the time–stepping process in order to account for the presence of a non–causal DC electric field arising from the galvanic source. The third major difference is also related to the initial conditions. Because this work focuses on data types given by the time derivative of the magnetic induction (voltage) instead of the magnetic field, the explicit computation of the initial DC magnetic field can be avoided. This is accomplished by advancing voltages instead of magnetic fields in the time–stepping algorithm. The modifications to the time–stepping scheme involve a divergence–free condition on both the electric current density and the voltage to ensure accurate results at late times. At last, the algorithm is designed to perform on parallel computing platforms in order to address the high computational demand of an explicit time–stepping scheme.

3.1 Methodology

In order to simulate the propagation of the total electric and magnetic field intensities $\mathbf{e}(\mathbf{r},t)$ and $\mathbf{h}(\mathbf{r},t)$, respectively, as a function of the position vector $\mathbf{r} = (x,y,z)$ and time t in a 3D earth, the governing Maxwell's equations[1] in the time domain are reviewed,

$$\begin{aligned} \nabla \times \mathbf{e} + \mu \frac{\partial \mathbf{h}}{\partial t} &= -\mathbf{m}^s, && (3.1a) \\ -\nabla \times \mathbf{h} + \sigma \mathbf{e} + \gamma \frac{\partial \mathbf{e}}{\partial t} &= -\mathbf{j}^s, && (3.1b) \end{aligned}$$

where σ is the conductivity and μ is the magnetic permeability of the earth. In Equation (3.1b) γ represents a fictitious displacement, which is explained further below. Equations (3.1) are inhomogeneous, because regions containing external sources are taken into account, where $\mathbf{j}^s$ and $\mathbf{m}^s$ are the impressed electric and magnetic current source fields, respectively. The magnetic current $\mathbf{m}^s$ can be described by means of a magnetic polarization vector $\mathbf{m}^p$ (*Ward and Hohmann* [1988], p. 144)

$$\mathbf{m}^s(\mathbf{r},t) = \mu(\mathbf{r}) \frac{\partial}{\partial t} \mathbf{m}^p(\mathbf{r},t). \tag{3.2}$$

This way of representing magnetic types of sources assumes $\mathbf{m}^p$ to be an integrated surface current. While being an useful artifice, Equation (3.2) is a purely theoretical construct as it demands the existence of magnetic monopoles in order to satisfy the continuity condition for magnetic charges [*Ward and Hohmann*, 1988].

The source field generated by the primary galvanic transmitter is further defined by

$$\mathbf{j}^s(\mathbf{r},t) = I\delta(\mathbf{r})u(t),$$

where I denotes the electric current, δ is Dirac's delta function, and the function $u(t)$ describes the source waveform after switching off the constant transmitter signal. Further needed are the conditions

$$\begin{aligned} \nabla \cdot \mathbf{b} &= 0, && (3.3a) \\ \nabla \cdot \mathbf{j} &= 0, && (3.3b) \end{aligned}$$

and the identities

$$\begin{aligned} \dot{\mathbf{b}} &= \mu \frac{\partial \mathbf{h}}{\partial t}, && (3.4a) \\ \mathbf{j} &= \sigma \mathbf{e}, && (3.4b) \end{aligned}$$

where $\dot{\mathbf{b}}$ will be referred to as voltage and $\mathbf{j}$ represents the total conduction current density.

The proper field simulation requires an adequate scheme for the discretization of the spatial differences given by the curl and divergence terms in Equations (3.1) and (3.3). The actual propagation of the EM field with progressing time is inherent in the discretization of the time derivatives in Equations (3.1). Both is accomplished by means of the staggered grid outlined in the following sections.

---

[1] In MKS system of units.

3.1.1 The staggered grid

The staggered grid [*Yee*, 1966] for discretizing Maxwell's equations in three dimensions is illustrated in Figure 3.1. The indices i,j and k are used to number the grid point locations in the x,y and z directions, respectively. Electric fields are sampled on the center of cell edges and magnetic fields on the center of cell faces. For example, to specify the sampling of the horizontal electric field in the x direction for a given grid node (i,j,k), the notation $e_x(i+\frac{1}{2},j,k)$ will be used. The corresponding magnetic field in the same direction is specified by $h_x(i,j+\frac{1}{2},k+\frac{1}{2})$.

The staggered grid is useful for the discretization of the curl operations in Maxwell's equations by means of elementary electric and magnetic loops [*Wang and Hohmann*, 1993]. Figure 3.1a illustrates how each electric field component is surrounded by an elementary loop of four magnetic components. As exemplified by the dashed rectangle around $e_x(i+\frac{1}{2},j,k)$, the axis of the magnetic loop is given by the edge where the electric field is sampled. The electric field components are assumed to be constant along the edges. For example, the field $e_x(i+\frac{1}{2},j,k)$ is constant along the edge between the nodes (i,j,k) and $(i+1,j,k)$. The elementary electric loops intertwine with magnetic loops, because a loop of four electric components on the borders of a cell face curls around each component of the magnetic field as shown in Figure 3.1b. The magnetic fields are oriented perpendicular to the face where they are sampled and are assumed to be constant over its area.

Each FD grid cell represents an element of the earth model with different material properties σ and μ, which are assumed to be constant over the cell. Following *Wang and Hohmann* [1993], each electric and magnetic field component is assigned to a directional electric conductivity and magnetic permeability, respectively. A directional conductivity is evaluated by averaging the weighted conductivities of the four prisms connected by the corresponding magnetic loop. This accounts for the continuity of conductivity across cell edges. For example, $\sigma_x(i+\frac{1}{2},j,k)$ is the average of the four cell conductivities $\sigma(i,j,k)$, $\sigma(i,j-1,k)$, $\sigma(i,j,k-1)$ and $\sigma(i,j-1,k-1)$. Each cell conductivity is weighted by the ratio of the face area cut by the magnetic loop to the total area of the loop. Instead of the arithmetic averaging scheme for magnetic permeabilities used by *Wang and Hohmann* [1993], geometric averaging is used as will be specified below.

3.1.2 Time–stepping of the EM field for causal sources

With the concept of the spatial sampling of the EM field in place, now the implementation of the space and time derivatives of Maxwell's equations is outlined. *Wang and Hohmann* [1993] describe a leap–frog scheme for advancing Equations (3.1) in time for causal source fields, arising from loop sources with an inductive coupling to the ground. It shall be recapitulated here in order to understand the modifications that will be made for the treatment of fields with a non–causal source excitation. Also, the time–stepping scheme for causal fields will be used for the propagation of the residual fields mentioned in the introduction of this chapter. The principle difference in both schemes is that time–stepping non–causal fields will be based on the time derivative of the magnetic induction (voltage) instead of magnetic fields.

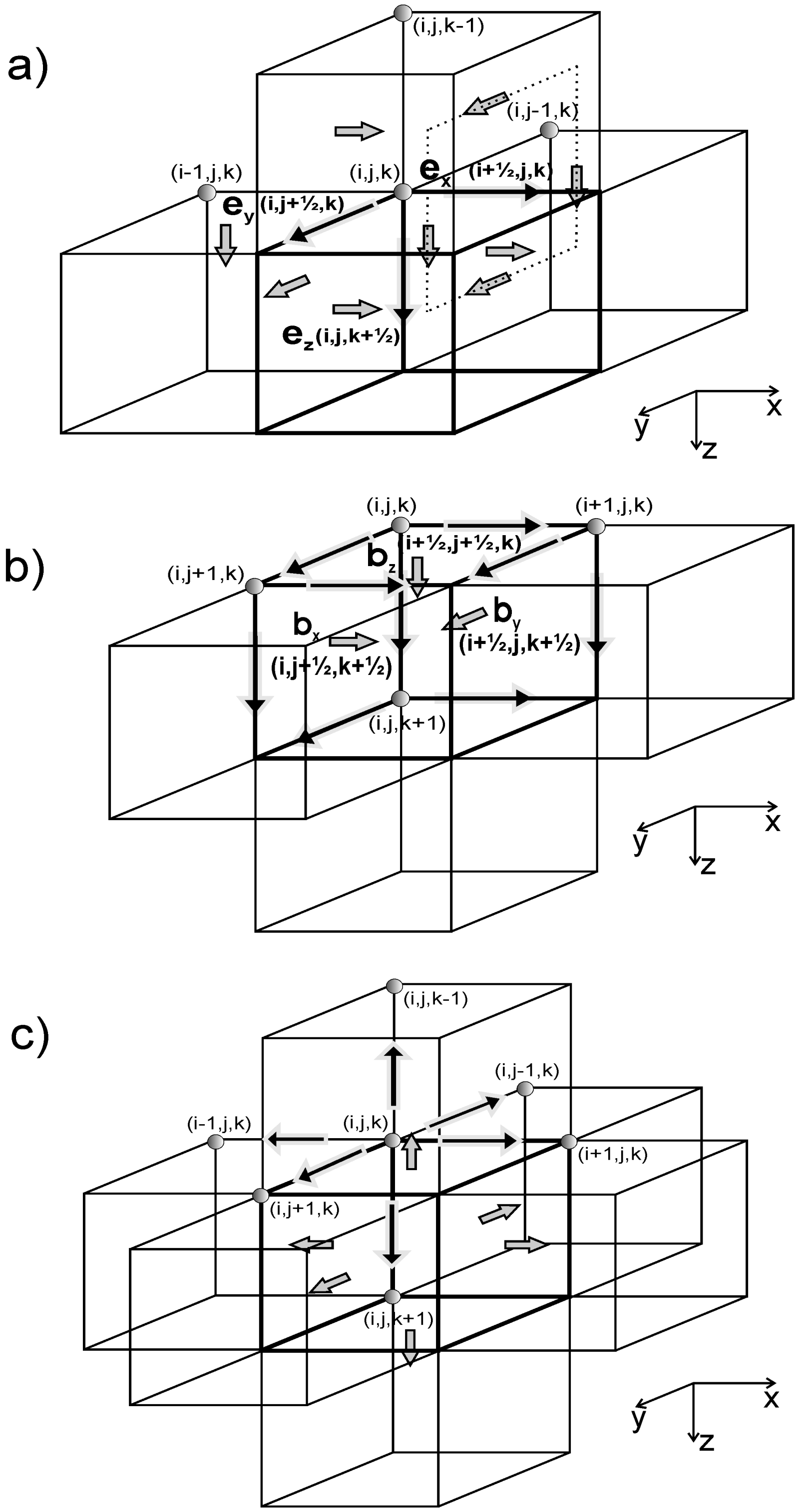

Figure 3.1: *The 3D staggered grid as used for discretizing Maxwell's equations. The electric field is sampled at the centers of the prism edges, and the magnetic field is sampled at the centers of the prism faces. (a) Elementary magnetic loops curl around electric fields, (b) elementary electric current loops curl around magnetic fields. (c) Realization of the discrete divergence for magnetic fields or voltages for a given cell (i,j,k) using the six components of the surrounding cell faces. The corresponding divergence of the current density incorporates the six components of the surrounding cell edges. (a)–(c) also illustrate the communication scheme for the parallel implementation of the field update explained in detail in Section 3.1.6.*

Approximating Equations (3.1) involves the discretization of the derivatives in space and time by finite differences. This introduces the spatial lengths Δx_i, Δy_j and Δz_k of a given grid cell (i,j,k), where for example Δx_i denotes the distance from node (i,j,k) to $(i+1,j,k)$. These quantities will be needed for discretizing elementary electric loops. Elementary magnetic loops run across cell edges and thus its sizes along each Cartesian direction are given by

$$\begin{aligned}\overline{\Delta x_i} &= \frac{\Delta x_{i-1}+\Delta x_i}{2},\\ \overline{\Delta y_j} &= \frac{\Delta y_{j-1}+\Delta y_j}{2},\\ \overline{\Delta z_k} &= \frac{\Delta z_{k-1}+\Delta z_k}{2}.\end{aligned}$$

The time derivatives involve the discrete time step Δt_n, where the indices $0,1,...,n-1,n,n+1$ are used to represent the time instants $t_0,t_1,...,t_{n-1},t_n,t_{n+1}$ with $t_{n+1}=t_n+\Delta t_n$. The time t_0 is defined to be the time of the current switch–off in the transmitter. Similar to the spatial sampling of the fields on the staggered grid, the electric fields are sampled at integer time indices $t_n+\Delta t_n$, and the magnetic quantities are sampled at intermediate time indices $t_n+\frac{\Delta t_n}{2}$. This way of sampling the fields indicates the leap–frog fashion of the time–staggering scheme.

The FD representations of Equations (3.1) are exemplified for the x component of the different fields. No magnetic sources are considered for now, because an external loop or grounded–wire transmitter only involves an electric current source field. First, Equation (3.1a) is discretized, starting with the component form

$$\frac{\partial b_x}{\partial t} = -\frac{\partial e_z}{\partial y} + \frac{\partial e_y}{\partial z}.$$

The approximation of the left–hand side at an integer time level n involves a central difference

$$\left(\frac{\partial b_x}{\partial t}\right)^n \approx \frac{b_x^{n+\frac{1}{2}} - b_x^{n-\frac{1}{2}}}{\Delta t_n}.$$

Then it follows for the updated magnetic induction [*Yee*, 1966]

$$\begin{aligned} & b_x^{n+\frac{1}{2}}(i,j+\tfrac{1}{2},k+\tfrac{1}{2}) = b_x^{n-\frac{1}{2}}(i,j+\tfrac{1}{2},k+\tfrac{1}{2}) \\ & -\Delta t_n \left[\frac{e_z^n(i,j+1,k+\frac{1}{2}) - e_z^n(i,j,k+\frac{1}{2})}{\Delta y_j} - \frac{e_y^n(i,j+\frac{1}{2},k+1) - e_y^n(i,j+\frac{1}{2},k)}{\Delta z_k} \right], \end{aligned} \tag{3.5}$$

where Δy_j and Δz_k are the extensions of the grid cell (i,j,k) in the y and z direction, respectively. The next step involves the computation of the magnetic field by

$$h_x^{n+\frac{1}{2}}(i,j+\tfrac{1}{2},k+\tfrac{1}{2}) = b_x^{n+\frac{1}{2}}(i,j+\tfrac{1}{2},k+\tfrac{1}{2})/\mu_x^{avg}(i,j+\tfrac{1}{2},k+\tfrac{1}{2}).$$

Following *Alumbaugh et al.* [1996], the permeability μ^{avg} is computed using a geometric average of the two neighbouring cell permeabilities connected by the magnetic field, thus for the x component

$$\mu_x^{avg}(i,j+\tfrac{1}{2},k+\tfrac{1}{2}) = \frac{(\Delta x_{i-1}+\Delta x_i)\mu(i-1,j,k)\mu(i,j,k)}{\Delta x_{i-1}\mu(i,j,k)+\Delta x_i\mu(i-1,j,k)}.$$

This accounts for the continuity of the magnetic induction that is normal to a cell face and connects the two cells involved in the average. After completion of the magnetic field update for all components, the electric fields are advanced. Again, start with the component form of the electric field in the x direction, derived from (3.1b),

$$\gamma \frac{\partial e_x}{\partial t} + \sigma e_x = \frac{\partial h_z}{\partial y} - \frac{\partial h_y}{\partial z} - j_x^s.$$

To sample both terms on the left–hand side at the same time instant $n + \frac{1}{2}$ of the updated magnetic field, a central difference for the time–derivative is again used,

$$\left(\frac{\partial e_x}{\partial t} \right)^{n+\frac{1}{2}} \approx \frac{e_x^{n+1} - e_x^n}{\Delta t_n},$$

and a simple average for the other term,

$$e_x^{n+\frac{1}{2}} \approx \frac{e_x^n + e_x^{n+1}}{2}.$$

This leads to the following expression for the updated electric field:

$$\begin{aligned} e_x^{n+1}(i+\tfrac{1}{2}, j, k) = {} & \frac{2\gamma - \Delta t_n \sigma_x(i+\frac{1}{2}, j, k)}{2\gamma + \Delta t_n \sigma_x(i+\frac{1}{2}, j, k)} e_x^n(i+\tfrac{1}{2}, j, k) + \frac{2\Delta t_n}{2\gamma + \Delta t_n \sigma_x(i+\frac{1}{2}, j, k)} \\ & \cdot \left[\frac{h_z^{n+\frac{1}{2}}(i+\frac{1}{2}, j+\frac{1}{2}, k) - h_z^{n+\frac{1}{2}}(i+\frac{1}{2}, j-\frac{1}{2}, k)}{\overline{\Delta y}_j} \right. \\ & \left. - \frac{h_y^{n+\frac{1}{2}}(i+\frac{1}{2}, j, k+\frac{1}{2}) - h_y^{n+\frac{1}{2}}(i+\frac{1}{2}, j, k-\frac{1}{2})}{\overline{\Delta z}_k} - j_x^n \right], \end{aligned} \tag{3.6}$$

where $\overline{\Delta y}_j$ and $\overline{\Delta z}_k$ specify the size of the elementary magnetic loop around e_x. The electric current source field impressed by the transmitter is given by j_x^n.

3.1.3 Numerical stability

A FD scheme is said to be stable if the difference between the theoretical and numerical solutions of the difference equation remains bounded for all grid nodes (i, j, k) as the simulation time increases [*Alford et al.*, 1974]. Unstable solutions are characterized by numerical dispersion, that is the improper simulation of high–frequency fields. Therefore, the first thing to ensure is the adaption of the spatial sampling Δ to the highest frequencies of the field. An estimation of the smallest number of gridpoints N per wavelength is given by *Wang and Hohmann* [1993]

$$N \leq \frac{\lambda_{min}}{\Delta},$$

where λ_{min} is the minimum wavelength. The approximation of the spatial finite differences in Section 3.1.2 by incorporating the fields of two adjacent prisms represents a second–order scheme. *Alford et al.* [1974] conclude that a number of $N = 10$ is adequate for a second–order scheme and that this number can be decreased by using a higher order scheme. In the course of this work, a fourth–order scheme has also been realized for the presented FD algorithm.

In principle, the approximation of the difference $\frac{\partial f}{\partial x}$ at a given grid node $i+\frac{1}{2}$ involves four adjacent grid nodes such that

$$\left(\frac{\partial f}{\partial x}\right)_{i+\frac{1}{2}} \approx c_{-1} f_{i-1} + c_0 f_i + c_1 f_{i+1} + c_2 f_{i+2},$$

where $c_{-1},\dots,c_2$ are functions of the grid geometry [*Wang and Hohmann*, 1993]. However, it turned out that the additional computation time due to the larger number of multiplication and division operations during time–stepping outruns the benefits of the fourth–order scheme.

Adaptive time–stepping

Another risk causing numerical dispersion occurs with an improper choice of the time steps. In principle, for a given spatial cell size of a FD grid, the size of the time step must be limited such that over one time increment the EM field does not change significantly. *Yee* [1966] derives a restriction for a constant time step in order to retain computational stability for an equidistant FD grid. For the presented algorithm, a gradual adaption of the time step to the rate of diffusion of the EM field is employed, because it allows for higher computational efficiency.

For the treatment of TEM fields, the diffusive approximation of Maxwell's equations, i.e. without displacement currents, needs to be considered. Hence, the term involving the variable γ in Equations (3.1) represents a fictitious displacement current. It is artificial and changes the equation from a diffusive form into a damped wave form, which represents a modified version of the DuFort–Frankel method [*DuFort and Frankel*, 1953; *Oristaglio and Hohmann*, 1984; *Adhidjaja and Hohmann*, 1989; *Wang and Hohmann*, 1993]. In fact, the variable γ is much larger than the true displacement current, but still small enough to allow an accurate simulation in the diffusive approximation. It is outlined in detail in Appendix A.1 that its incorporation allows the use of larger time steps than with a conventional Euler type scheme applied to the diffusive forms of Equations (3.1). Therefore, it allows to address the attenuation of high frequency components of the EM field with time by a gradual increase of the time step Δt_n in Equations (3.5) and (3.6) with progressing simulation time. This reduces the computation time to some extent, where the benefit is significant for very late time field simulations. However, both the initial and subsequent time steps are limited by the condition (see also Appendix A.1)

$$\Delta t_n \ll \sqrt{\frac{\mu_{min}\sigma_{min} t}{6}}\Delta_{min}, \tag{3.7}$$

where μ_{min}, σ_{min} and Δ_{min} are the minimum values of magnetic permeability, conductivity and FD grid spacing, respectively. This ensures the domination of diffusion after the earliest measured time t, otherwise spurious wave–like modes dominate the behaviour of the simulated fields. In practice, a maximum time step of

$$\Delta t_{max} = 0.1\sqrt{\frac{\mu_{min}\sigma_{min} t}{6}}\Delta_{min}$$

has proven to be adequate for the presented algorithm.

Both the time step and the minimum grid spacing control the fictitious permittivity γ by the Courant–Friedrichs–Levy criterion for the wave velocity c of a wave-like equation [*Richtmeyr and Morton*, 1967; *Oristaglio and Hohmann*, 1984]

$$c = \frac{1}{\sqrt{\mu\gamma}} \leq \frac{\Delta_{min}}{\sqrt{3}\Delta t_n}.$$

From that condition, one obtains

$$\gamma \geq \frac{3}{\mu_{min}} \frac{\Delta t_n^2}{\Delta_{min}^2}, \tag{3.8}$$

which needs to be updated if the time step is increased.

Divergence–free condition

Another important issue for stability is the explicit enforcement of a vanishing divergence for the magnetic induction **b**. Even with the benefits of a staggered grid, which implicitly preserves the flux conditions on current density and magnetic induction fields, it is necessary to explicitly enforce the divergence–free condition. Outlined in more detail by *Wang and Hohmann* [1993] and *Smith* [1996], the enforcement can be regarded as gauge condition to avoid distorting arbitrary gradient fields that can creep into the EM field simulation at later times. This can be seen by taking the divergence of Equation (3.1a), which implies the divergence–free condition for the time derivative of the magnetic induction **b**. By assuming that no magnetic charges exist (*Jackson* [1975], p. 294), Equation (3.3a) follows. However, in the static case Equation (3.1a) reduces to

$$\nabla \times \mathbf{e} = 0.$$

The uniqueness of the magnetic field, previously given by the coupling of Equations (3.1) does not exist anymore, because arbitrary gradient fields can now be added to **b** without violating Equation (3.1b). Thus, in the DC limit the divergence–free condition of **b** is not implied and the presence of numerical noise can cause erroneous gradient fields. In practice, one typically would observe a wrong late time response in the form of a reduced decay rate. In a test simulation, without explicit enforcement of (3.3a), it could be observed that very late time responses approached a DC level.

The enforcement of the divergence–free condition for **b** in the time–stepping algorithm involves computing two field components in a way represented by Equation (3.5). From these two components, the remaining one is then updated using Equation (3.3a). Its FD approximation is obtained at the center of a prism using the six components of the surrounding cell faces as shown in Figure 3.1c. Then the discrete form

$$\begin{aligned}
&\frac{b_x^{n+\frac{1}{2}}(i+1, j+\frac{1}{2}, k+\frac{1}{2}) - b_x^{n+\frac{1}{2}}(i, j+\frac{1}{2}, k+\frac{1}{2})}{\Delta x_i} \\
+&\frac{b_y^{n+\frac{1}{2}}(i+\frac{1}{2}, j+1, k+\frac{1}{2}) - b_y^{n+\frac{1}{2}}(i+\frac{1}{2}, j, k+\frac{1}{2})}{\Delta y_j} \\
+&\frac{b_z^{n+\frac{1}{2}}(i+\frac{1}{2}, j+\frac{1}{2}, k+1) - b_z^{n+\frac{1}{2}}(i+\frac{1}{2}, j+\frac{1}{2}, k)}{\Delta z_k} = 0
\end{aligned} \tag{3.9}$$

is obtained and is rearranged to

$$\begin{aligned} b_z^{n+\frac{1}{2}}(i+\tfrac{1}{2},j+\tfrac{1}{2},k) = {} & b_z^{n+\frac{1}{2}}(i+\tfrac{1}{2},j+\tfrac{1}{2},k+1) \\ & + \Delta z_k \left[\frac{b_x^{n+\frac{1}{2}}(i+1,j+\frac{1}{2},k+\frac{1}{2}) - b_x^{n+\frac{1}{2}}(i,j+\frac{1}{2},k+\frac{1}{2})}{\Delta x_i} \right. \\ & \left. + \frac{b_y^{n+\frac{1}{2}}(i+\frac{1}{2},j+1,k+\frac{1}{2}) - b_y^{n+\frac{1}{2}}(i+\frac{1}{2},j,k+\frac{1}{2})}{\Delta y_j} \right]. \end{aligned} \tag{3.10}$$

It can be seen that this way of updating the vertical fields b_z involves a recursive procedure. For this example, it starts at the lower mesh boundary where $b_z = 0$ and is carried out upwards, i.e. towards the surface boundary.

In order to treat non–causal source fields, the modified time–stepping scheme presented below will be based upon the time derivative of the magnetic induction $\dot{\mathbf{b}}$ (voltage) instead of $\mathbf{b}$. Thus, in contrast to the time–stepping algorithm for causal sources, the condition

$$\nabla \cdot \dot{\mathbf{b}} = 0 \tag{3.11}$$

is enforced. Because voltages are sampled on the same positions as the magnetic fields, the divergence–free condition is realized in the same way as exemplified by (3.10).

Numerical experiments have shown that the explicit enforcement of

$$\nabla \cdot (\nabla \times \mathbf{h}) = \nabla \cdot \mathbf{j} = 0$$

is needed in addition to the condition given by (3.11), which has not yet been fully understood. A possible explanation might be, that time–stepping voltages instead of magnetic fields leads to a lower degree of coupling between Equations (3.1) in a numerical sense. This could be due to the fact that both voltages and electric fields are sampled at the same (integer) time instants.

Like electric fields, the components of $\mathbf{j}$ are sampled on cell edges, thus

$$\begin{aligned} & \frac{j_x^n(i+\frac{1}{2},j,k) - j_x^n(i-\frac{1}{2},j,k)}{\overline{\Delta x}_i} + \frac{j_y^n(i,j+\frac{1}{2},k) - j_y^n(i,j-\frac{1}{2},k)}{\overline{\Delta y}_j} \\ & + \frac{j_z^n(i,j,k+\frac{1}{2}) - j_z^n(i,j,k-\frac{1}{2})}{\overline{\Delta z}_k} = 0 \end{aligned} \tag{3.12}$$

represents the divergence approximation for a given cell (i,j,k) as illustrated in Figure 3.1c. Note that for example the index $(i-\frac{1}{2},j,k)$ denotes the component $j_x(i+\frac{1}{2},j,k)$ of the cell $(i-1,j,k)$.

3.1.4 Boundary conditions

For computational efficiency, the spacings between the grid nodes are enlarged with increasing offset from the source position. This is allowed as the diffusive EM field smoothes gradually with distance from the source [*Oristaglio and Hohmann,* 1984]. The continuity at the subsurface boundaries of the mesh is ensured by simply extending the borders to a sufficient distance from the source and setting its tangential electric and normal magnetic field components to zero. The distance of the mesh boundaries from the source may have to be adapted to the underlying earth model. If the boundaries are too close to the transmitter or receiver positions, one can observe erroneous results due to grid reflection at late times. This problem becomes more severe for very resistive backgrounds, where the diffusing fields face less attenuation than in a more conductive earth.

A critical aspect is the treatment of the earth–air interface, where the tangential electric fields do not vanish. A straightforward approach is realized by simply extending the mesh above the surface grid layer far enough such that the upper mesh boundary satisfies the same conditions as the subsurface boundaries. The grid space above the surface needs to be made very resistive in order to approximate air. However, Equation (3.7) indicates that the air resistivity would require very small time steps to simulate the rapid decay of the fields in air. Both handling a larger mesh and the small time step lead to an increased computation time.

The more efficient alternative involves an upward–continuation boundary condition [*Macnae*, 1984; *Oristaglio and Hohmann*, 1984; *Wang and Hohmann*, 1993] for the air–earth interface. It is based on the validity of the vector Laplacian equation

$$\nabla^2 \mathbf{b} = 0, \tag{3.13}$$

which can be obtained from the vector Helmholtz equation for magnetic fields by assuming the quasi–static case and a vanishing conductivity σ in free space. Equation (3.13) is also valid for voltages and allows to apply the methods for the continuation of potential fields (*Grant and West* [1965], p. 216–220) that are typically used in connection with gravity and magnetic methods [*Militzer and Weber*, 1984]. This involves a 2D spatial Fourier transform of the vertical voltage fields at the surface into the wavenumber domain. The horizontal fields above the surface can then be obtained by continuation of the vertical fields, using the following wavenumber domain equations [*Wang and Hohmann*, 1993]

$$\dot{\mathcal{B}}_x(u,v,z=-h) = -\frac{iu}{\sqrt{u^2+v^2}}\,\mathrm{e}^{-h\sqrt{u^2+v^2}}\,\dot{\mathcal{B}}_z(u,v,z=0), \tag{3.14a}$$

$$\dot{\mathcal{B}}_y(u,v,z=-h) = -\frac{iv}{\sqrt{u^2+v^2}}\,\mathrm{e}^{-h\sqrt{u^2+v^2}}\,\dot{\mathcal{B}}_z(u,v,z=0), \tag{3.14b}$$

where $\dot{\mathcal{B}}_x$, $\dot{\mathcal{B}}_y$ and $\dot{\mathcal{B}}_z$ are the Fourier transforms of the voltages $\dot{b}_x$, $\dot{b}_y$ and $\dot{b}_z$. Equations (3.14) also hold for the magnetic induction. The wavenumber domain variables u and v correspond to the spatial variables x and y, respectively, and h is the height above the surface. This boundary condition only requires a single additional vertical grid level for the air space.

Implementation of the upward–continuation procedure is realized in the following manner. A 2D spatial Fast Fourier Transform (FFT) is used for the transformation of the vertical fields at the surface into the wavenumber domain. The FFT is preceded by a spline interpolation [*Press et al.*, 1992] in order to cast the nonuniform grid spanned by the discrete surface values of $\dot{b}_z$ onto an equidistant grid. After the Fourier transformation, the air layer horizontal fields in the wavenumber domain are obtained by Equations (3.14). Next, an inverse FFT is performed on both $\dot{\mathcal{B}}_x(u,v,z=-h)$ and $\dot{\mathcal{B}}_y(u,v,z=-h)$. Finally, the resulting horizontal fields in the space domain are interpolated back to the original mesh, now sampled at the air grid level. The parallel implementation of this scheme will be described in Section 3.1.6.

3.1.5 Time–stepping of the EM field for non–causal sources

The updating scheme described in Section 3.1.2 could also be employed for the treatment of fields generated by a galvanic grounded–wire source. Such a source causes the presence of a DC electric and magnetic field in the earth before the steady transmitter signal is switched off. The DC electric field can be computed with little computational effort as will be shown below. However, the initialization of the magnetic field would involve a numerically more elaborate solution of a magnetometric resistivity problem [*Edwards and Nabighian*, 1991]. This work focuses on TEM systems that measure the time derivative of the magnetic induction (voltage) instead of magnetic fields. Voltages represent causal fields that are zero before t_0, Therefore, the presented updating scheme is based on voltages in order to avoid calculating the DC magnetic fields. The modifications made for the time–stepping procedure are straightforward and shall be given in vector form.

Field initialization

To initialize the fields, first the DC electric field $\mathbf{e}^{DC}$ in the model and the induced electric field $\mathbf{e}^{ind}$ inside the wire source need to be computed. The latter one is obtained by inverse interpolation of the source distribution $\mathbf{j}^s$ impressed by the transmitter onto the FD grid. Then the field $\mathbf{e}^{ind}$ for the grid nodes that are comprised by the source is obtained from (3.4b), which automatically accounts for arbitrary distributions of σ over the mesh.

Because the DC electric field $\mathbf{e}^{DC}$ is curl free, it is determined by applying the divergence operator to the static form of (3.1b),

$$\nabla \cdot (\sigma \nabla \varphi) = -\nabla \cdot \mathbf{j}^s, \tag{3.15}$$

where $\mathbf{e}^{DC}$ can be expressed as the gradient of a potential field φ. Thus, a 3D Poisson problem which is common in 3D resistivity modeling is solved. Here, a straightforward seven–point discrete approximation to the Poisson operator is used. It is a common way of discretization and involves a center grid cell and its six direct neighbours along the main coordinate axes as outlined in detail in Appendix A.2. This represents a simplified form of the scheme described by *Dey and Morrison* [1979]. A variety of more elaborate schemes exists; for example refer to *Spitzer and Wurmstich* [1999], who give a comprehensible overview and comparison of five different seven–point operators.

Equation (3.15) represents a sparse, diagonally dominant linear system, which is positive definite due to the positivity of σ. Hence, the solution for φ can be obtained by an efficient preconditioned conjugate–gradient solver. The parallel iterative package AZTEC [*Hutchinson et al.*, 1995] is used for this purpose. After computing $\mathbf{e}^{DC}$ from the gradient of φ, the curl of the magnetic field is computed from the static form of (3.1b),

$$\nabla \times \mathbf{h}^{DC} = \sigma \mathbf{e}^{DC} + \mathbf{j}_s.$$

Both the DC fields given by $\mathbf{e}^{DC}$ and $\nabla \times \mathbf{h}^{DC}$ represent the initial fields for the following time–stepping scheme.

Advance of the EM field

First, the voltages are updated from

$$\dot{\mathbf{b}}^n = -\nabla \times \mathbf{e}^n. \tag{3.16}$$

They originate from the decay of the induced electric field $\mathbf{e}^{ind}$ in the source after switch–off. Note that voltages are sampled at the same time instants as electric fields. First, the horizontal components $\dot{b}_x^n$ and $\dot{b}_y^n$ are computed from (3.16). In order to enforce the divergence–free condition for $\dot{\mathbf{b}}^n$, the vertical component $\dot{b}_z^n$ is then calculated using (3.11) with its discrete form similar to (3.9). The recursive update starts from the lower mesh boundary, where $\dot{b}_z = 0$ applies, and is proceeded upwards. Then the horizontal voltages $\dot{b}_x^n$ and $\dot{b}_y^n$ above the surface are calculated by upward–continuation of the fields $\dot{b}_z^n$ at the surface. Now $\dot{\mathbf{h}}^n$ is given by

$$\dot{\mathbf{h}}^n = \dot{\mathbf{b}}^n / \mu.$$

Instead of the magnetic field $\mathbf{h}$, its curl is used as an intermediate quantity in order to update the electric fields. Therefore, the curl of $\dot{\mathbf{h}}^n$ is formed by the components defining the elementary loop around the respective electric field. Afterwards, the central difference approximation

$$\nabla \times \dot{\mathbf{h}}^n = \frac{\nabla \times \mathbf{h}^{n+\frac{1}{2}} - \nabla \times \mathbf{h}^{n-\frac{1}{2}}}{\Delta t_n}$$

is rearranged to

$$\nabla \times \mathbf{h}^{n+\frac{1}{2}} = \nabla \times \mathbf{h}^{n-\frac{1}{2}} + \Delta t_n \cdot \nabla \times \dot{\mathbf{h}}^n \tag{3.17}$$

to update the curl of $\mathbf{h}$ at the time $t_{n+\frac{1}{2}}$. Note that during the first time step at time t_0

$$\nabla \times \mathbf{h}^{-\frac{1}{2}} = \nabla \times \mathbf{h}^{DC}.$$

Again, only the horizontal components are updated from (3.17). To enforce the condition

$$\nabla \cdot (\nabla \times \mathbf{h}) = \nabla \cdot \mathbf{j} = 0,$$

the vertical components of $\mathbf{j}$ are updated from the horizontal components using (3.12) in a similar way as exemplified by (3.9) and (3.10). In contrast to the voltages, the recursive update starts from the top of the mesh, because j_z vanishes at the air grid layer. Finally, the electric field is advanced by

$$\mathbf{e}^{n+1} = \frac{2\gamma - \sigma \Delta t_n}{2\gamma + \sigma \Delta t_n} \mathbf{e}^n + \frac{2\Delta t_n}{2\gamma + \sigma \Delta t_n} \left(\nabla \times \mathbf{h}^{n+\frac{1}{2}} - \mathbf{j}_s^{n+\frac{1}{2}} \right). \tag{3.18}$$

Afterwards, the updating procedure loops back to the calculation of the voltages for the next time step.

3.1.6 Parallel implementation

The realistic simulation of complex 3D structures may require a large number of grid nodes and can quickly lead to the limits of a single processor computer in terms of memory needs and processor speed. To achieve acceptable computation times, the FD scheme has been designed to run on massively parallel machines using the Message Passing Interface (MPI) Standard [*Skjellum et al.*, 1993]. To realize parallelization, the 3D model is subdivided with every individual processor in charge of a 3D subset of the mesh. Therefore, a given number of processors is arranged into a Cartesian topology. This implies that the total number of processors is separable in a way that it amounts to $n_x \times n_y \times n_z$ processors, according to the distribution of processors in the x, y and z direction of the global mesh, respectively. Each processor carries out the field update in its own subset. Across the boundaries of the subsets interprocessor communication is needed as outlined below. As long as the communication is minimal relative to the computation times for the field updates, the solution time can be reduced by a factor that is approximately equal to the number of processors employed. However, this requires that the Cartesian processor topology provides for a load balance. This is realized by creating the mesh subsets such that they are as equal in size as possible. With an unbalanced load, long idle times would otherwise deteriorate the performance of the parallel scheme.

Following *Alumbaugh et al.* [1996], the input data needed by each processor prior to the actual field calculations is split up into local and global data. Local data comprise the model properties, that are assigned to each cell of a 3D mesh subset. To save both memory and disk space, each processor stores only the properties of its own subset. Global data are those variables that each processor needs to know, for example all information about the source and receiver setup. For the later presented inversion based upon this forward simulation algorithm, additional information of that kind needs to be added to the global data set, such as the observed data to be inverted. Global data is read in by a master processor and then distributed, local data is read in individually by each processor.

Parallel time–stepping algorithm

The fact that the elementary electric and magnetic loops on the staggered grid described in Section 3.1.1 are intertwined with each other, indicates that communication between adjacent processors is required during time–stepping. The message passing across processor boundaries introduces the expression 'ghost' for a grid node. The ghost nodes of a processor contain the fields that are needed in order to complete the update of its own fields, yet are calculated by an adjacent processor. This is illustrated in Figure 3.1, where it is assumed for simplification that each processor is assigned to only one grid node of the 3D mesh. During a single time step of the field update, the processor at node (i, j, k) needs to communicate with all six neighbours. The communication scheme is now outlined in the same order as the field update in Section 3.1.5.

One starts with the update of horizontal voltages from the curl of electric fields (Equation 3.16). Figure 3.1b shows that this requires a prior communication with nodes $(i+1, j, k)$,

$(i,j+1,k)$ and $(i,j,k+1)$ in order to complete the two elementary electric loops around $\dot{b}_x$ and $\dot{b}_y$ at node (i,j,k). Each procedure that is referred to as communication or message passing involves a pair of send and receive operations with an adjacent node. For example, in Figure 3.1b consider the electric loop assigned to $\dot{b}_y(i+\frac{1}{2},j,k+\frac{1}{2})$ and the field component $e_z(i+1,j,k+\frac{1}{2})$ assigned to node $(i+1,j,k)$. Node (i,j,k) needs to submit a receive signal to $(i+1,j,k)$ in order to get the ghost value $e_z(i+1,j,k+\frac{1}{2})$. At the same time, node $(i+1,j,k)$ submits a send operation to (i,j,k), because it is in charge of $e_z(i+1,j,k+\frac{1}{2})$. A similar communication with $(i,j,k+1)$ is necessary in order to complete the electric loop around $\dot{b}_y(i+\frac{1}{2},j,k+\frac{1}{2})$. Likewise, the completion of the electric loop around $\dot{b}_x(i,j+\frac{1}{2},k+\frac{1}{2})$ involves message passing with nodes $(i,j+1,k)$ and $(i,j,k+1)$.

The recursive update of the vertical voltage at node (i,j,k) to enforce the divergence–free correction first needs the previously computed horizontal voltages from nodes $(i+1,j,k)$ and $(i,j+1,k)$ (Figure 3.1c). For the actual calculation of $\dot{b}_z(i+\frac{1}{2},j+\frac{1}{2},k)$, the “lower” $\dot{b}_z(i+\frac{1}{2},j+\frac{1}{2},k+1)$ also has to be obtained by a communication with node $(i,j,k+1)$. Note that the performance of the parallel divergence–free enforcement is limited to some extent. Because of the recursive procedure, only the nodes in the same vertical layer given by k can compute $\dot{b}_z$ at the same time.

Afterwards, the upward continuation procedure of the vertical voltage components at the surface layer follows. Its parallel implementation is explained in an extra section below. The following electric field update at node (i,j,k) is preceded by forming the curl of the voltages around the horizontal edges where $e_x(i+\frac{1}{2},j,k)$ and $e_y(i,j+\frac{1}{2},k)$ are sampled. Therefore, message passing according to the stencil shown in Figure 3.1a is carried out. The required voltage values belong to the ghost nodes $(i-1,j,k)$, $(i,j-1,k)$ and $(i,j,k-1)$. Then the horizontal components of the magnetic field curl are updated using Equation 3.17. Afterwards, node $(i-1,j,k)$ passes the x component and node $(i,j-1,k)$ passes the y component of the magnetic field curl to node (i,j,k). This is required for the enforcement of the divergence–free condition for the current density $\mathbf{j}$ as illustrated by Figure 3.1c. Again, it is carried out recursively, now starting from the upper mesh boundary. Similar to the divergence–free correction for voltages, the ghost value $j_z(i,j,k-\frac{1}{2})$ updated previously by the “upper” node $(i,j,k-1)$ needs to be received before node (i,j,k) can compute $j_z(i,j,k+\frac{1}{2})$.

The recursive procedure of the divergence–free corrections suggests that the partitioning of the vertical mesh by n_z processors should not be too fine. Otherwise, the message passing overhead due to the communication of the vertical ghost values might be too large. One can choose the extreme of a pencil structure for the domain decomposition, with no partitioning of the mesh in the vertical direction. However, the optimal decomposition strongly depends on the type of the parallel architecture employed. It is recommended to be evaluated by adequate prior tests.

Parallel upward–continuation

The parallel implementation of the 2D FFT, required by the upward–continuation boundary condition for the vertical voltage values, involves a rather complicated message passing procedure. This is caused by the fact that both the interpolation to an equidistant grid and the

FFT perform on a processor topology that is different to the one given by the domain decomposition into 3D subcubes. Moreover, the topology changes during the upward–continuation process. Therefore, rather than a communication across fixed processor boundaries, several rearrangements of the field distribution among the processors are carried out, which is also referred to as remapping.

The scheme developed here is illustrated in Figure 3.2 for the example of four processors sharing the surface layer, where (a) represents the initial condition. The 2D interpolation to an

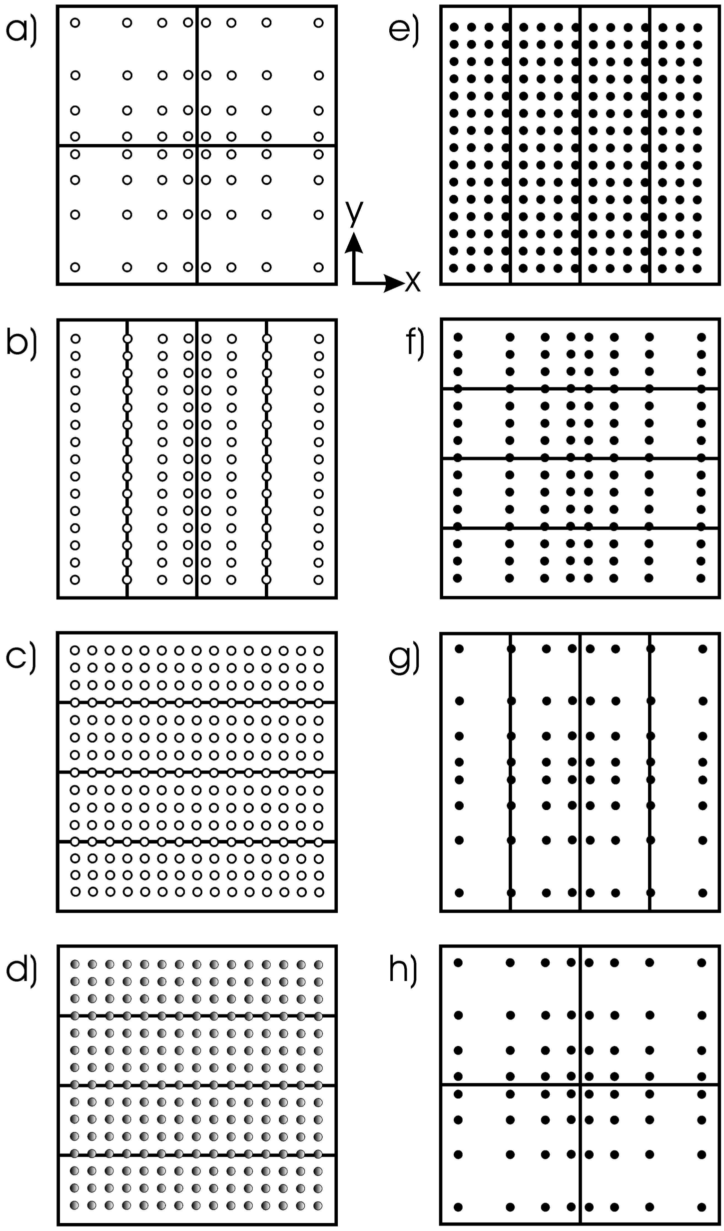

Figure 3.2: Parallel field upward continuation scheme for a distribution of the surface grid layer among four processors. The upward–continuation procedure involves remapping, interpolation, forward and inverse 2D FFT steps carried out along both horizontal dimensions x and y of the surface grid layer. The sequence of steps: (a) Initial distribution. (b) Remap, y–interpolation. (c) Remap, x–interpolation. (d) FFT(x). (e) Remap, FFT(y), upward continuation, FFT^{-1}(y), remap, FFT^{-1}(x). (f) x–interpolation, (g) Remap, y–interpolation. (h) Remap to initial distribution.

equidistant grid spacing is carried out consecutively along both horizontal grid axes. Because of accuracy, all field values along the extension of a grid axis need to be incorporated into the interpolation. For example, at a given point on the y axis, the corresponding processor in charge of casting the non–uniform grid sampling on the x axis into an equidistant sampling needs to know all values on the global x axis. Therefore, the 2D spline interpolation of the surface field values $\dot{b}_z$ to an equidistant FFT grid requires two data remapping steps. First, the original chessboard–like field distribution among the processors is remapped into a striped pattern that allows the equi–sampling in the grid's y direction as shown in (b). Afterwards, the processor topology is changed such that the interpolation can be completed along the x axis (c).

The following 2D FFT from the spatial into the wavenumber domain involves another remap since it is first done in the x direction and afterwards in the y direction (d and e). Now the actual continuation of the wavenumber domain horizontal fields into the air layer is carried out using Equations 3.14. It belongs to the characteristics of a 2D FFT, that its output has a transposed order [*Frigo and Johnson*, 1998]. As a consequence, the horizontal grid axes are interchanged for the fields in the wave–domain. One can take advantage of that by precalculating the grid's wavenumber domain variables from a transposed horizontal grid. Otherwise a further remapping step would be required in order to retain the non–transposed order in the wave–domain.

After calculation of the horizontal fields, the inverse FFT of the horizontal fields is carried out first in the y direction and then in the x direction, thereby again transposing the order of the output and hence restoring the original order. The steps for the interpolation from the equidistant grid back to the original one now proceed in reversed order to the steps (a)–(c). This involves two more remaps as shown by (f)–(h).

Unfortunately, the parallelization of the procedure offers little opportunity to be accelerated due to the deficient scalability of the FFT and a high message passing overhead. Since the FFT dominates the computation time of the upward–continuation procedure, the only significant acceleration can be achieved by using the fact that the TEM field is smoothed gradually in space with increasing time. With a smooth field, the number of equidistant grid nodes and hence the computation time for both FFT and interpolation can be reduced. With the employed FFT algorithm optimized for a number of data points of order 2^n, an appropriate initial regular grid spacing is chosen such that no undersampling occurs. After a predefined time, the spacing is doubled. Based on a series of empirical experiments, it could be found that the time after which the constant grid can be widened depends on the decay rate of the fields. For example, a resistive overburden allows for an earlier change to a coarser FFT grid than a more conductive overburden. For the simulation examples shown in this chapter, the change to a coarser FFT grid was carried out after 2–3 time decades, starting from the initial time step.

3.2 Synthetic data examples

A citation from *Hohmann* (1988) reads as follows: 'The numerous possibilities for theoretical and programming errors make it necessary to compare results computed by different methods before a numerical solution can be considered valid.'[2]

This section demonstrates the accuracy of the numerical solution by a variety of models incorporating different complexities, field configurations and simulation time ranges. The models include horizontal layers, 3D structures and a combination of both. The solutions are referred to as FD solutions and are compared with different kinds of other algorithms. These include both analytical and integral–equation methods [*Newman et al.*, 1986] and the spectral Lanczos decomposition method (SLDM) [*Druskin and Knizhnerman*, 1988]. The latter one is the forward modeling code used by the inversion scheme presented in Chapter 2.

All simulated electric field measurements correspond to the component parallel to the transmitter orientation. The voltages are shown in the form of vertical components. In addition, the first example shows the voltages from the horizontal magnetic component in a direction perpendicular to the transmitter. The employed FD meshes were adapted in size to the different purposes, ranging from a largest grid size of $159 \times 123 \times 71$ to a size of $97 \times 82 \times 46$ nodes. The smallest modeled cell size is 10 m on each edge. Initial time steps are predetermined according to Equation (3.7). A summary of the employed grid sizes and initial time steps will be given at the end of this section.

1) Layered half–space

The first example is typical for the LOTEM method. The horizontal and vertical voltage responses over a four–layered half–space with downwards decreasing resistivities as shown in Figure 3.3a are simulated. Figures 3.3b,c and d show the electric field and vertical and horizontal voltage responses, respectively, in comparison with analytical responses. The fields are generated by a 1 km long grounded wire and are extracted at distances of 500–5000 m broadside to the transmitter. The two solutions demonstrate a very good agreement with each other. In this example, the reflections off the mesh boundaries reach a critical level at times later than 1 s, thereby causing a slight DC offset that can be observed for the electric field solutions at the latest simulated time of 1 s. However, such undesirable effects can be delayed to later times by further expanding the outer mesh boundaries. The solution for the horizontal voltage also shows a very good agreement for the occurence of the sign reversals. The diffusing fields are clearly indicated by a move out in the sign reversal.

---

[2] To be read in the preface of 'Three–dimensional Electromagnetics', SEG, Tulsa.

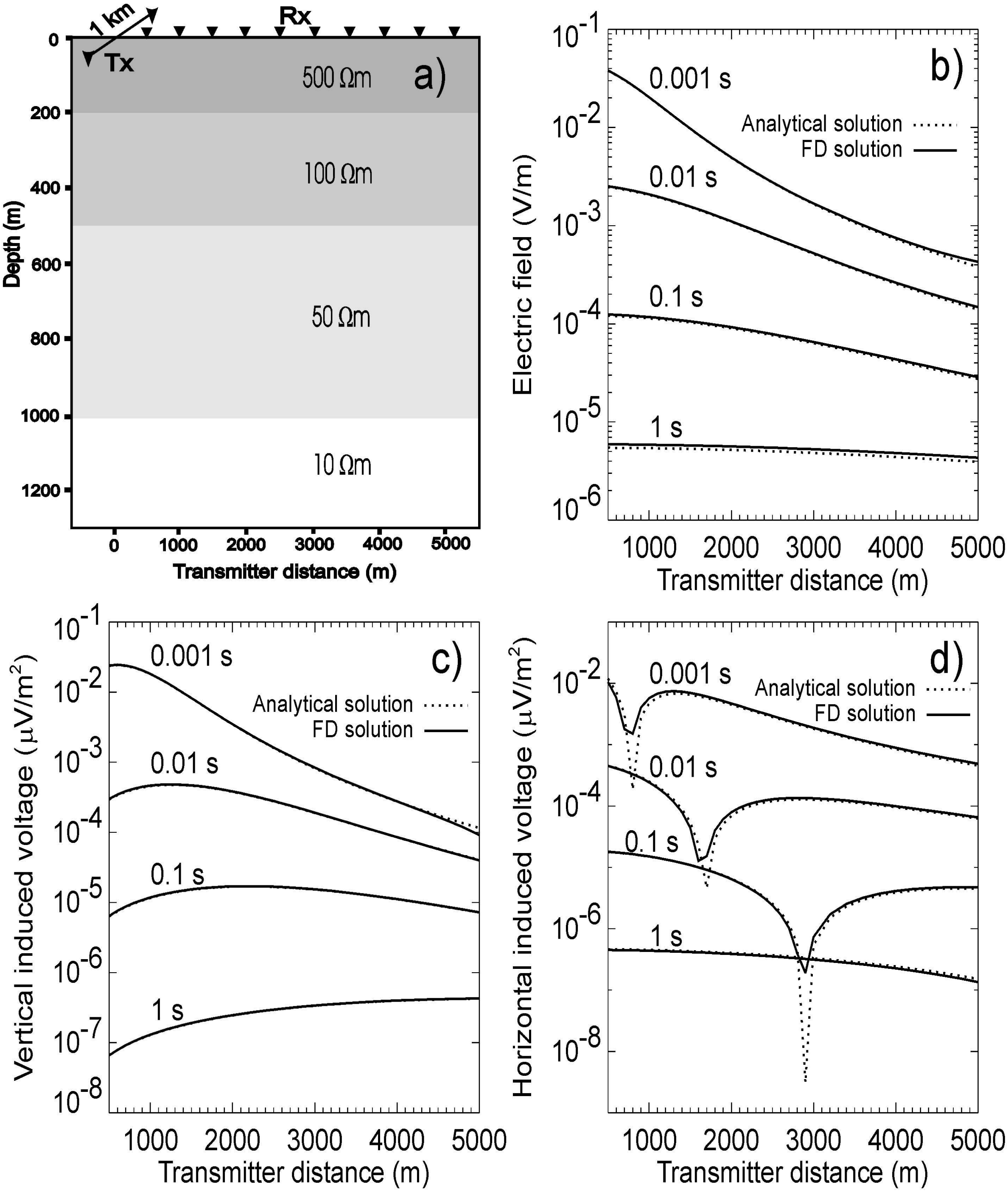

Figure 3.3: *FD solution (solid lines) over a four–layered host in comparison with an analytical solution (dashed lines). (a) Earth model with transmitter–receiver setup. The transmitter is perpendicular to the receiver profile. (b) Electric field response. (c) Vertical voltage response. (d) Horizontal voltage response.*

2) Homogeneous half–space with permeable layer

Next, the solution for a layered half–space with homogeneous resistivity (10 Ωm) and a permeable layer at a depth of 100 m is calculated. The relative magnetic permeability of this layer is 10 and its thickness is 100 m. Similar to the previous example, responses are calculated broadside to the transmitter, which in this example is a 10 m long grounded wire. Figures 3.4a and b show the vertical voltage at an offset of 100 m and 400 m, respectively. The FD solution (solid curves) is compared with an analytical result for the permeable layer (*Hanstein*, pers. comm.) and shows a very good agreement for the smaller offset. For the larger distance an agreement with the analytical solution is reached after 0.7 ms. In addition to the analytical response of the permeable model, the field of a non–permeable half–space (dashed curves) is shown. It demonstrates that the very high magnetic permeability contrast of 10 is necessary in order to obtain a significant influence of the permeable layer. In comparison with real permeabilities measured in the field, this contrast is rather unrealistic.

The early time sign reversal in the FD response in Figure 3.4b is not realistic for this configuration. It is a numerical effect caused by the upward continuation boundary condition. Its occurrence can be explained by the fact that during transmitter current switch–off the FFT carries the rapid field changes in the source simultaneously forward to the receiver. Using a grid with adequately high resistivities to simulate the fields in air, instead of the FFT approach, would not have such an effect.

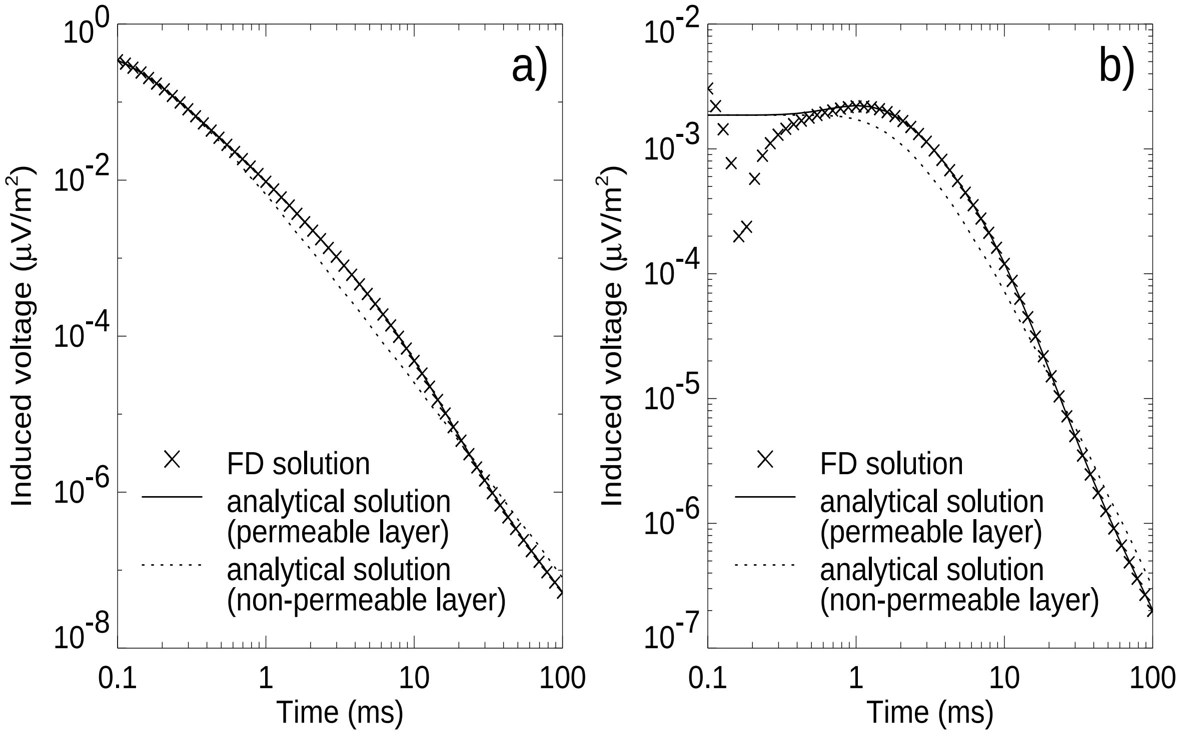

Figure 3.4: *Comparison of the FD vertical voltage (cross symbols) and an analytical (Hanstein, 2003, pers. comm.) solution (solid lines) for a half–space with homogeneous resistivity and a permeable layer (see text for details). Dashed lines show the analytical response over a non–permeable half–space. The transients are calculated for a source–offset of (a) 100 m and (b) 400 m.*

3) Conductive 3D block in a homogeneous half–space

The next example compares the electric field FD responses over a 1 Ωm conductive block in a 200 times more resistive half–space with an IE solution. Figure 3.5a shows a plan view of the field setup and the anomaly that has a size of 100 m along each edge. The upper edge of the block starts at a depth of 100 m. The fields are generated by a 100 m long grounded wire at 150 m distance from the block's center. Results are shown in Figures 3.5b,c and d and correspond to the three receiver positions shown in Figure 3.5a. For all positions, the FD solutions yield an excellent agreement with the IE solutions. Figure 3.5 also shows analytical half–space solutions (dashed lines) to illustrate the effect of the conductive block. The comparison with the 3D response shows that the block causes an amplitude increase at early times and a decrease at later times. This effect is small for the receiver position between transmitter and block ($x = 75$ m), whereas a clearer effect occurs for the other receivers. For this simulation the resistive background required an initial time step of $\Delta t_0 \approx 10^{-7}$ s in order to avoid a distorting wave–like influence of the fictitious displacement current at early times.

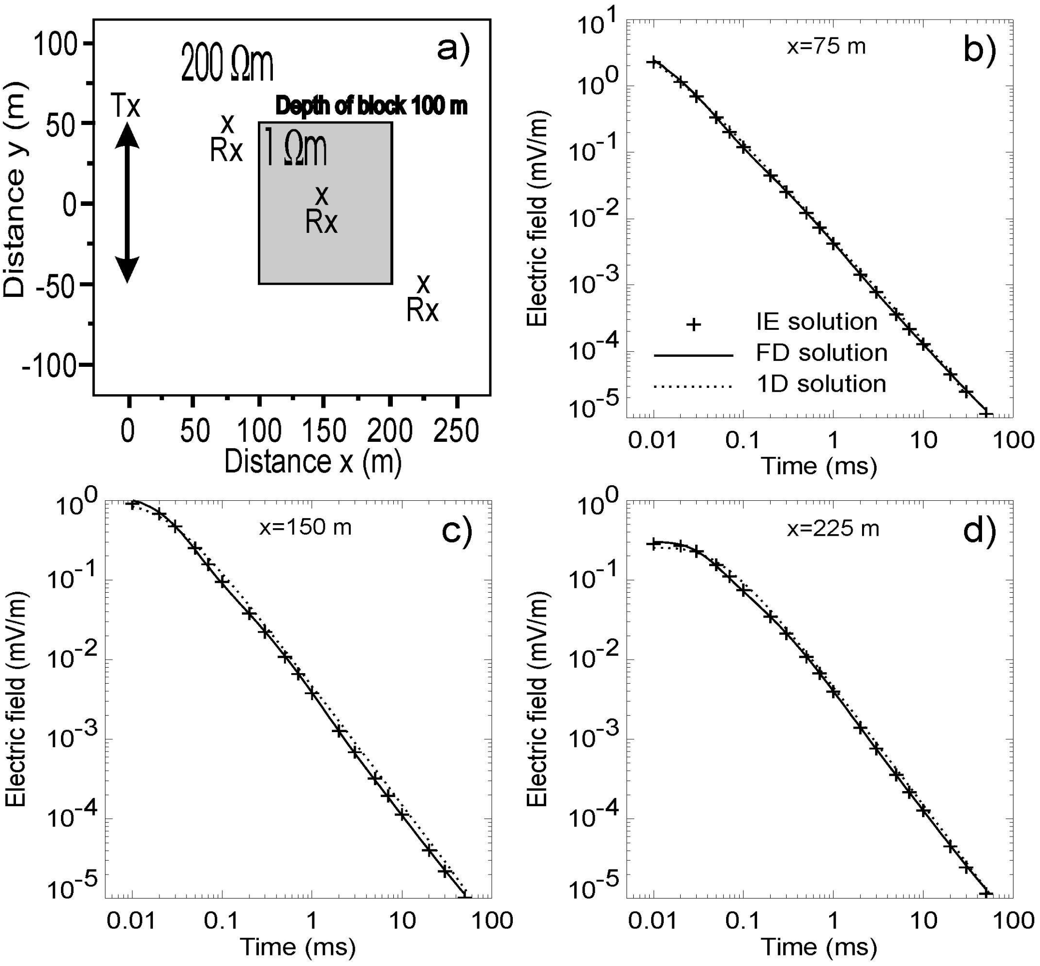

Figure 3.5: FD solution (solid curve) over a homogeneous host with an embedded 3D block in comparison with an IE solution (cross symbols). The block's effect is made visible by the analytical response (dashed curve) over a half–space without block. (a) Earth model with transmitter–receiver setup. Electric field responses are calculated at the x coordinates (b) 75 m, (c) 150 m and (d) 225 m.

4) Complex 3D conductor at a vertical contact

The next synthetic data are calculated for a 3D model similar to an example presented by *Wang and Hohmann* [1993], yet with a higher model complexity. The model section in Figure 3.6a consists of a 50 m thin conductive layer (10 Ωm) at the surface and an underlying laterally divided resistive earth. At the contact of the 100 Ωm and 300 Ωm resistors, a 1 Ωm conductive 3D anomaly varies in steps along the profile direction. This structure, which is 400 m in strike length, reaches a depth of 550 m. Figures 3.6b and c show the electric and vertical voltage field responses, respectively, at arbitrarily chosen locations. For a comparison, the FD responses are shown together with the SLDM solution, because the simulated model complexity would not allow to obtain a solution by using the IE method. In general, the solutions compare well for each receiver location with some discrepancies at the earliest delay times. As observed for both types of responses, early time deviations are largest close to the transmitter. The sign reversal in the electric field response above the right edge of the anomaly ($x = 500$ m) occurs slightly earlier for the SLDM solution, but still good agreement is given at delay times after 1 ms. For this field–setup, a crossover in the voltage only occurs between transmitter and anomaly. Apart from the early time discrepancies at $x = 200$ m, an excellent agreement for the voltages, including the reversal at $x = 200$ m, is achieved over the whole time range.

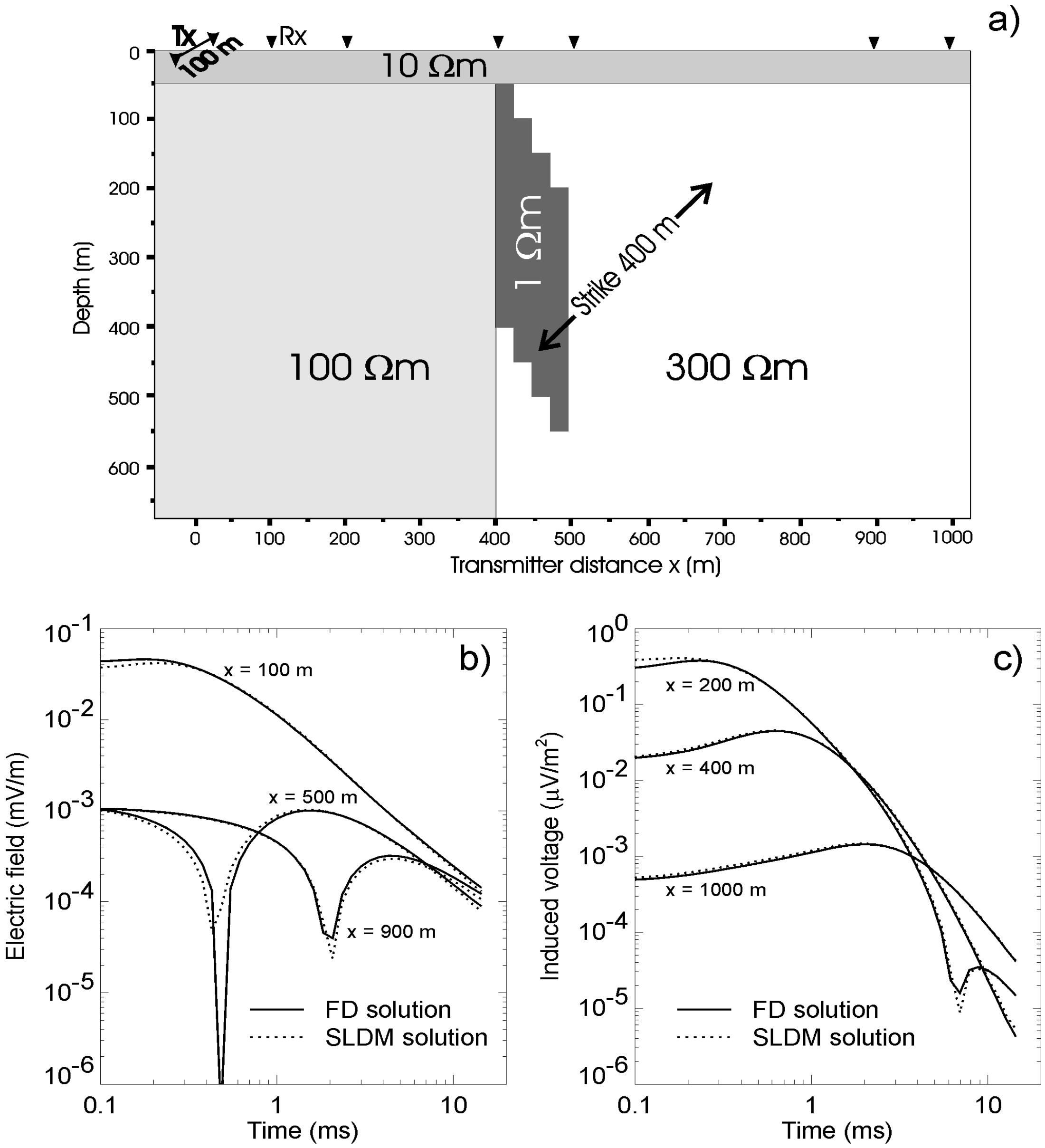

Figure 3.6: *FD solution (solid lines) from a complex 3D anomaly at a vertical contact and a layered overburden in comparison with a SLDM solution (dashed lines). (a) Earth model. The transmitter is perpendicular to the receiver line. (b) Electric field responses at 100 m, 500 m and 900 m distance from the transmitter. (c) Vertical voltage responses at 200 m, 400 m and 1000 m distance from the transmitter.*

5) Resistive reservoir structure in a layered host

In contrast to the previous 3D models, this example involves a more complex resistive anomaly in a layered background. The earth model shown in Figure 3.7a was initially designed by *Hördt et al.* [2000*a*] from a priori well log information and represents a natural underground gas storage site at St. Illiers (near Paris, France). At 140 m depth the 50 Ωm sedimentary overburden is interrupted by a 20 m thick 15 Ωm–layer. The 10 Ωm conductive basement, starting at 310 m depth, encompasses the dome–shaped reservoir with the upper and lower edges at 490 m and 602 m depth, respectively. The reservoir extends 2000 m in the direction perpendicular to the drawing plane, and the shown section does not vary in this direction. A resistivity of 200 Ωm is assigned to the 25 m thick gas–bearing layer. In a sensitivity study, *Hördt et al.* [2000*a*] simulated LOTEM responses over a profile covering the reservoir structure in order to investigate if resistivity variations at the reservoir margins are detectable. With magnetic fields less sensitive to thin resistive structures, the study was based on electric fields in an axial configuration. The 50 m long transmitter is located over the left reservoir edge and points in the profile direction. The receivers record the transmitter–parallel field component.

First, the FD responses shall be compared with the SLDM solution of *Druskin and Knizhnerman* [1988], which is also employed by *Hördt et al.* [2000*a*]. Figure 3.7b shows the inline electric field solutions for four different receiver positions. Although the curve pairs agree qualitatively, some quantitative differences exist. Here, the mesh employed for the SLDM solution consists of $43 \times 43 \times 27$ nodes, which is a rather coarse grid discretization compared to the $127 \times 90 \times 83$ nodes used for the FD solution. Therefore, a better agreement would be achieved using a finer mesh for SLDM. However, it could be observed that a grid refinement in both horizontal dimensions and the more crucial vertical dimension quickly leads to wrong SLDM results at late times. This can be explained by the aspects related to the convergence of SLDM as outlined in Section 2.1.1. The SLDM solution has a slow convergence, because the long time interval ranging from 0.1 ms to 0.3 s causes a large grid aspect ratio and introduces ill–conditioning to the system of equations to be solved [*Druskin et al.*, 1999]. A grid refinement provides for more accurate results, yet increases the FD grid aspect ratio and thus further slows the convergence. Therefore, finding a compromise between the requirements for a stable convergence of SLDM takes place at the expense of accuracy.

For the mentioned sensitivity study, it is important that an algorithm is capable of resolving the effects of small model variations. For simulating a lower amount of gas fill, *Hördt et al.* [2000*a*] changed the resistivities of both left and right reservoir edges to the value of the surrounding layer. In Figure 3.7a the reservoir edges are marked as white blocks. Figure 3.7c shows the FD responses of both original and downsized reservoir for the same transmitter position as before and two different receiver distances. At 1400 m distance, no significant difference in the results occurs, since transmitter and receiver are located above the anomaly in such a way that its edges hardly cause an influence on the fields. However, at 2000 m one observes an altered response, indicating the influence of the right reservoir margin.

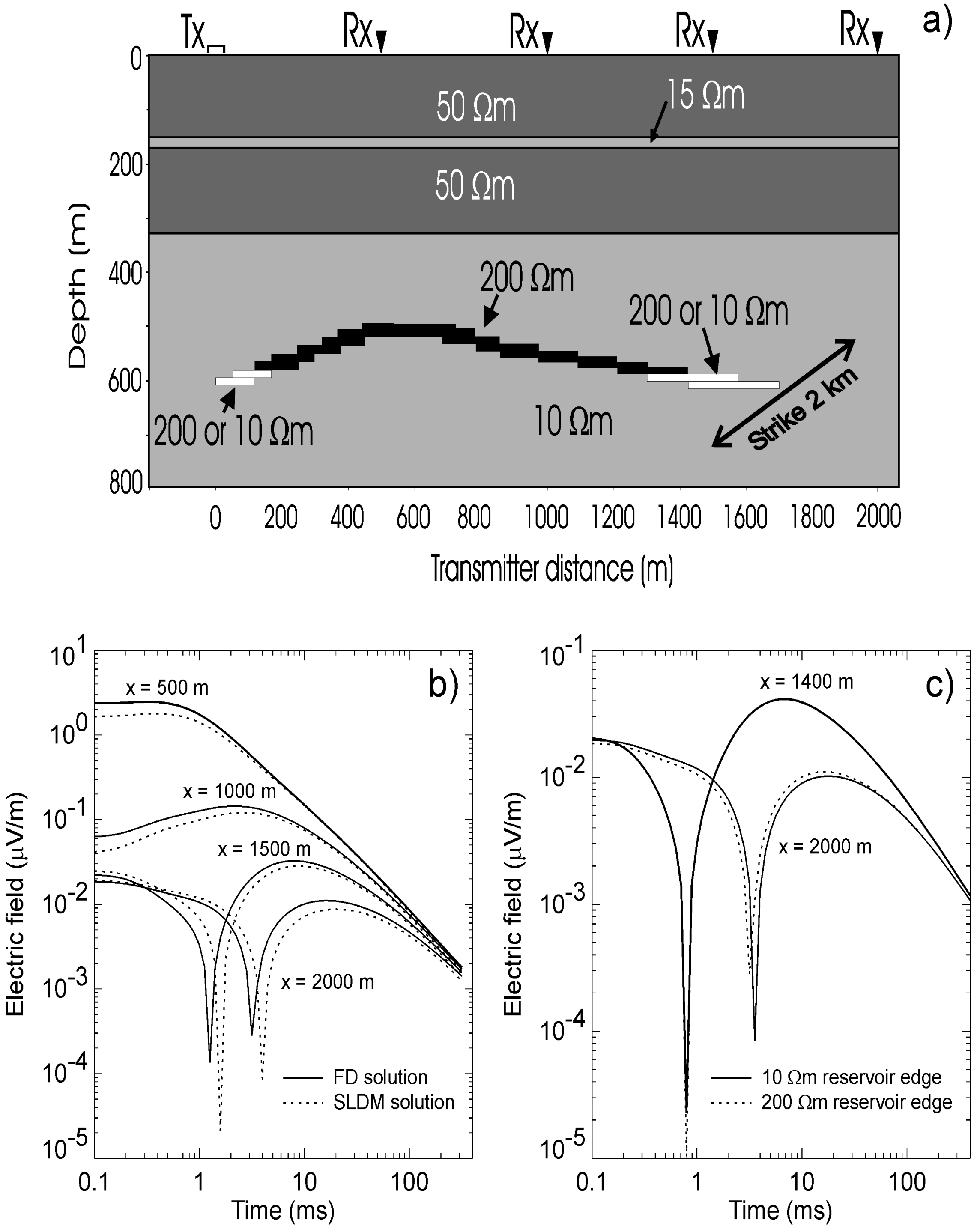

Figure 3.7: *FD simulation of the 3D model from the underground gas storage site at St. Illiers (France) as derived from a priori information [Hördt et al., 2000a]. (a) Section view of the earth model. The transmitter is inline with the receiver profile. (b) Comparison of the electric field FD response (solid lines) with the SLDM solution (dashed lines) at the receiver positions 500 m, 1000 m, 1500 m and 2000 m. (c) Electric field FD response comparisons at 1400 m and 2000 m distance from the transmitter for a downsized reservoir (solid lines) and the full reservoir (dashed lines). To realize the downsized reservoir, the resistivity of the left and right edges (white blocks) is set equal to the resistivity of the surrounding layer.*

3.3 Discussion

A versatile time–stepping scheme to solve the diffusive Maxwell equations for galvanic source configurations has been presented. The parallel code simulates electric field and magnetic induction time derivative responses for 3D models where both conductivity and magnetic permeability are functions of space. Comparisons with analytical, IE and SLDM solutions show that accurate results are obtained over complicated earth models. The gas reservoir example in particular demonstrates the scheme's high degree of accuracy, which is necessary to simulate response differences caused by a small model variation. Compared to the SLDM solution technique, the scheme has the advantage that it provides for better stability in the presence of large resistivity contrasts in the model and late simulation times.

The scheme's accuracy is achieved at the expense of a high computational time demand. This problem is inherent to an explicit time–stepping method and becomes more severe with the simulation of later times. The computation times required by all presented examples are shown in Table 3.1 and exemplify the influence of grid size, initial time step size and latest simulated time on the computational requirements of a solution. All presented simulations were carried out on a SUN$^{\mathrm{TM}}$ Fire 6800 machine, where sometimes not the full processor capacity was available due to heavy machine load. The small number of processors employed for all examples indicates that on larger massively parallel platforms the computation times can be greatly reduced.

Result	FD grid size	Processors $n_x \times n_y \times n_z$	Initial time step Δt_0 (s)	Latest simulation time (s)	Estimated computation time (hrs)
1	$129 \times 111 \times 61$	$3 \times 3 \times 1$	10^{-6}	1	14
2	$123 \times 123 \times 65$	$3 \times 3 \times 1$	10^{-6}	0.1	8
3	$97 \times 82 \times 46$	$3 \times 3 \times 1$	10^{-7}	0.1	4
4	$159 \times 123 \times 71$	$4 \times 3 \times 1$	10^{-7}	0.03	6
5	$127 \times 90 \times 83$	$3 \times 3 \times 1$	10^{-6}	1	15

Table 3.1: *Summary of the estimated computation times required by the presented solutions. The factors that govern the computational effort shared between the $n_x \times n_y \times n_z$ processors are FD grid size, initial time step and latest simulation time.*

Other strategies worth investigating for improving the computational efficiency exist. *Alumbaugh et al.* [1996] mention that a thorough study of the outer grid design is necessary in order to avoid slow convergence of their implicit frequency domain scheme due to large cell aspect ratios. Although not crucial for the stability of the presented method, an adequate grid–stretching scheme could help to minimize the number of grid nodes required for an exact solution. In addition, a material averaging scheme [*Moskow et al.*, 1999] would allow a model parameterization that is in principle independent from the underlying FD grid, thus further relaxing the meshing constraints.

CHAPTER 4

A LARGE–SCALE INVERSION APPROACH USING NON–LINEAR CONJUGATE–GRADIENTS

The solution for the inversion problems presented in Chapter 2 represents a constrained least–squares or Gauss–Newton solution arising by solving a Lagrange multiplier problem in which the error cost functional is minimized subject of a bounded parameter change. This solution belongs to the class of direct methods, which obtain an exact solution (except for roundoff errors) in a finite number of iterations and are adequate for small–scale problems. The inversion problems treated in this chapter, however, are characterized by large data sets, typically needed in order to resolve a finely discretized earth model with a numerous set of unknowns. The number of unknowns may reach as many as several thousands or tens of thousands in real exploration problems. For the solution of such large–scale problems, the Gauss–Newton approach becomes less efficient or even unfeasible, depending on the size of the problem. This owes largely to the fact that for each step of a Gauss–Newton iteration two computationally intensive tasks need to be performed. First, the full Jacobian (sensitivity) matrix of the forward modeling operator needs to be calculated. Second, a complete solution of a linear system on the model space, involving matrix inversion techniques, is required.

More direct and feasible in terms of computational aspects for the minimization of a given cost functional are gradient methods, which belong to the class of iterative methods. In contrast to direct methods, an approximation to the exact solution is carried out successively by a repeated evaluation of the forward modeling operator, thereby not requiring both storage and inversion of the Jacobian. For a given point in the model space, gradient methods only require functional and derivative information in order to evaluate both direction and step length of a model enhancement. The method of steepest descent [*Dennis and Schnabel*, 1996] is the easiest understood and simplest to implement for this purpose. However, it is usually characterized by a poor convergence in the presence of ill–conditioned inverse problems. Described more mathematically by *Meister* [1999], the method often finds itself taking steps towards a minimum of the cost functional in the same direction as earlier steps. A more efficient approach employed here is the method of non–linear conjugate–gradients (NLCG), first proposed by *Fletcher and Reeves* [1964] for non–linear optimization problems and later improved by *Polyak and Ribière* [1969]. The method is related to the method of linear conjugate–gradients (CG) of *Hestenes and Stiefel* [1952], yet with the framework of an iterated, linearized minimum search abandoned. The linear CG method was employed in a pioneering work of *Mackie and Madden* [1993] in order to solve the 3D MT inversion problem. Later, *Rodi and Mackie* [2001] implemented a NLCG scheme for a 2D MT inversion algorithm and *Newman and Alumbaugh* [2000] formulated a 3D MT inverse solution using NLCG.

The relative computational effort for the derivative information required for an iterative reduction of the cost functional can be equated to the calculation of the sensitivity matrix in a Gauss–Newton type solution. Because of the high computation times needed by the explicit time–stepping algorithm for a single forward simulation, a perturbation method as used by SINV becomes not feasible within reasonable computation times. Instead, the gradient information is obtained by a method strongly related to seismic migration techniques, therefore sometimes also referred to as EM migration [*Zhadanov et al.*, 1988].

Classical least–squares methods in principle investigate if any significant change in the parameters substantially alters a significant part of the observable data in order to quantify a model enhancement. Migration techniques attack the problem from a reversed point of view. A given difference between observed and predicted data (residuals) is treated as a source field, also called residual field, and propagated backwards (in reverse time) into the earth model. The field propagated forwards in time is the one producing the predicted data from the current earth model and is referred to as the incident field. For the purpose of inversion of seismic reflection data *Tarantola* [1984] outlined that correlating incident and residual field at each point of the model space enables one to quantify model corrections that minimize the residuals if applied to the current model. In other words, if at a point in the model space there is a model parameter perturbation, there will be an anomalous field which at that point will be correlated with the incident field. In seismic migration the anomalous field is also referred to as diffracted pressure field, and in the context of EM imaging the anomalous field will represent the field due to an anomalous current distribution. The following section will first outline the principles of EM migration in a rather heuristic approach. Important aspects, that is the description of fields excited by point–sources in terms of Green functions and related symmetry properties, will as well be introduced before a more rigorous theoretical treatment is given in the subsequent sections.

4.1 Principles of EM migration

The imaging methods for seismic wavefields are sometimes described by an exploding reflector concept and basically involve the propagation of a field backwards in time and its cross correlation with an incident field [*Claerbout*, 1971; *Loewenthal et al.*, 1976; *Tarantola*, 1984]. Similar to seismic migration, the migrated EM fields originate from that part of the field which is not taken into account by the current earth model, i.e. an assumed model guess. This introduces the data residuals as the difference between the incident or primary field for some given model, where the model is described by a distribution of the conductivities over the 3D space, and the actual observed field produced by the true earth model. The data residuals are treated as the source of a residual field. The flow of the residual field, originating from the surfaces of the observation points, i.e. the receivers, through the earth can be treated as a functional of an anomalous conductivity distribution in the model. To get a further understanding of how the residual field and the incident field is related to such an anomalous conductivity distribution, consider the time–domain integral equation [*Hohmann*, 1988],

$$\mathbf{e}(\mathbf{r},t) = \mathbf{e}_p(\mathbf{r},t) + \int_V \int_0^t \mathcal{G}(\mathbf{r},t|\mathbf{r}',t')\mathbf{j}_a(\mathbf{r}',t')dt'd\mathbf{r}'. \tag{4.1}$$

Illustrated in Figure 4.1, the equation describes the total electric field $\mathbf{e}(\mathbf{r},t)$ at an observation point $\mathbf{r}$ in the 3D space as the sum of a scattered electric field generated by the anomalous currents $\mathbf{j}_a$ in the volume V plus a primary background field $\mathbf{e}_p(\mathbf{r},t)$. *Boerner and West* [1989] indicate that the anomalous conductivity $\delta\sigma_a$ is proportional to a somewhat equivalent electric dipole source distribution. It is parallel to and proportional with the current density $\mathbf{j}_a$ created in the earth at $\mathbf{r}'$ by the external source field, thus

$$\mathbf{j}_a(\mathbf{r}',t) = \delta\sigma_a(\mathbf{r}')\mathbf{e}(\mathbf{r}',t').$$

Describing the scattered electric field at $\mathbf{r}$ due to a conductivity perturbation by means of a “point–source excitation” at $\mathbf{r}'$ introduces $\mathcal{G}(\mathbf{r},t|\mathbf{r}',t')$ as the tensor or dyadic Green’s function [*Felsen and Marcuvitz*, 1973]. In the case of electric fields (magnetic fields will be considered further below), it represents the electric field impulse response at $\mathbf{r},t$ arising from a unit vector force density[1] acting in the direction of the unit vector at $\mathbf{r}',t'$ [*Felsen and Marcuvitz*, 1973]. In practice, the elements of this tensor are obtained by calculating all three cartesian components of the electric field’s impulse response for each cartesian orientation of the unit

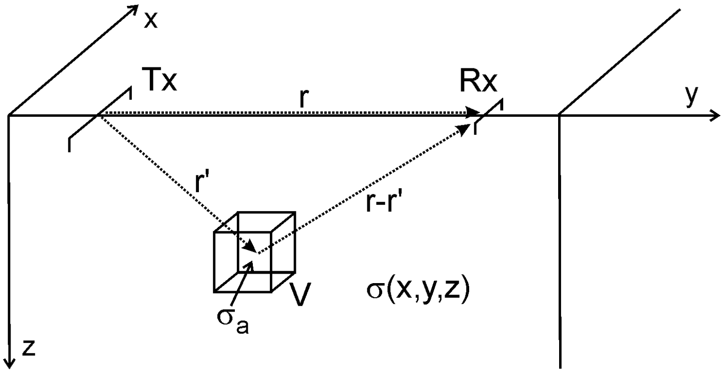

Figure 4.1: *Illustration of the geometry for the reciprocal relationship between a point at* $\mathbf{r}'$ *in the model space and a receiver at* $\mathbf{r}$*. Both the external source (Tx) and the receiver (Rx) are electric dipoles.*

---

[1] A unit vector force density at $\mathbf{r}',t'$ has the space–time form $\mathbf{u}'\delta(\mathbf{r}-\mathbf{r}')\delta(t-t')$, where $\mathbf{u}'$ is a unit vector.

dipole source at $\mathbf{r}',t'$. For example, written in a dyadic form, $\mathbf{e}_y \cdot \mathcal{G}(\mathbf{r},t|\mathbf{r}',t') \cdot \mathbf{e}_x$ represents the electric field impulse response in the y direction at $\mathbf{r},t$ produced by an unit electric dipole source at $\mathbf{r}',t'$ in the x direction.[2] Here, the reciprocity theorem can be applied [*Hohmann*, 1988; *Ward and Hohmann*, 1988]. Formally written as

$$\mathcal{G}(\mathbf{r},\mathbf{r}') = \mathcal{G}(\mathbf{r}',\mathbf{r}),$$

it says that if both the source/receiver positions and the source/receiver components are interchanged, the calculated fields will be the same. Expressed by the example, instead of calculating the y–directed electric field impulse response at $\mathbf{r}$ due to a x–directed electric dipole source at $\mathbf{r}'$, one can reverse the process such that the transmitter operates as a receiver. Thus, the x–directed electric field at $\mathbf{r}'$ caused by an impulsive y–directed electric dipole source at $\mathbf{r}$ is identical.

From Equation (4.1) it can be seen that the primary electric field $\mathbf{e}_p(\mathbf{r}',t')$ would equal the total field in the case of a vanishing anomalous conductivity. The equation can be used to derive the time–domain electromagnetic sensitivities [*Hördt*, 1998], which can be basically identified by the difference between the total and the primary electric field with respect to a model perturbation $\delta\sigma_a$. Assuming a very small perturbation $\delta\sigma_a$ allows to replace the total electric field at $\mathbf{r}'$ with the primary or unperturbed field $\mathbf{e}_p(\mathbf{r}',t')$ [*Hördt*, 1998]. Using this approximation together with the reciprocity relation, Equation (4.1) is rewritten to

$$\frac{\mathbf{e}(\mathbf{r},t) - \mathbf{e}_p(\mathbf{r},t)}{\delta\sigma_a(\mathbf{r}')} = \int_V \int_0^t \mathcal{G}(\mathbf{r}',t'|\mathbf{r},t)\mathbf{e}_p(\mathbf{r}',t')dt'd\mathbf{r}'. \tag{4.2}$$

From a classical point of view, the left–hand side represents a measure for the field variation at $\mathbf{r}$ produced by a change in the model parameter at $\mathbf{r}'$, thus it is the parameter sensitivity. The integral on the right–hand side represents an efficient way of calculating the sensitivities for the whole model domain. It is realized by carrying out a convolution of the background (primary) electric field $\mathbf{e}_p(\mathbf{r}')$ with the electric field impulse response at $\mathbf{r}'$ sourced at $\mathbf{r}$ by an unit electric dipole. The method is efficient, because reciprocity implies that the sensitivity at $\mathbf{r}$ for each image point $\mathbf{r}'$ over the model is obtained by a single convolution.

Viewed from a somewhat reversed point, the convolution integral also represents a way to quantify, for a given earth model, the parameter perturbation at $\mathbf{r}'$ that has to be performed in order to let the difference between total and background field vanish. If now in Equation (4.2) the total electric field $\mathbf{e}$ is replaced by an observed field measured at $\mathbf{r},t$ over an unknown model, and the background field $\mathbf{e}_p$ is replaced by a forward solution of a model guess, one can identify the basic principle of EM migration. In the limit $\delta\sigma_a \to 0$, the equation's left–hand side represents the gradient of the data residual with respect to the perturbation of the model conductivity and thus a means to find a model perturbation that minimizes the data residual.

In the following section it will be shown that the field propagated by $\mathcal{G}(\mathbf{r}',t'|\mathbf{r},t)$ becomes a migrated residual field, because it is sourced by the actual data residuals calculated from an assumed earth model instead of a single impulse signal. The migrated field is also referred to

---

[2] Formally, the tensor $\mathcal{G}$ is dot product multiplied from the right by the unit vector assigned to $\mathbf{e}_x$.

as backpropagated field. It is propagated backwards in time, because its excitation starts with the latest data residuals and continues towards the ones belonging to time zero. This follows from the reciprocity relationship and might clarify a possible confusion arising from the fact that seismic migration is usually addressed by a cross correlation between incident and migrated wavefield, sometimes also referred to as 'downgoing' and 'upgoing' [*Claerbout*, 1971; *Tarantola*, 1984] field, respectively. To be correct, the cross correlation between two fields propagated forwards and backwards in time can be regarded as a convolution of two fields that are both stepped forwards in time, yet with one differing by a time–reversed feeding with its respective source field. For the time–stepping algorithm developed in Chapter 3 there actually exists no major difference between a classical forward simulation or a backpropagation of the EM field. Both kinds of fields employ the same time–stepping scheme. Only the implementation of the source is different.

It can be concluded that the gradients of the data residual, which will be related to an error functional further below, with respect to the model conductivities $\sigma(\mathbf{r}')$ can be efficiently calculated by means of only two field simulations. The correlation of the backpropagated field with the incident field is carried out over the whole inversion domain, thus yielding the gradients at each point $\mathbf{r}'$. The combination with an iterative algorithm for a minimum search of an error functional makes EM migration a powerful imaging technique. Compared to the seismic counterpart, the major difference is that it is carried out on the basis of Maxwell's equations. This will be treated thouroughly in the following section.

4.2 Background: Diffusive Maxwell's equations, Green dyadics and adjoints

The first order Maxwell's equations given previously by Equations (3.1) are first rewritten in the diffusive approximation,

$$\begin{aligned}\nabla\times\mathbf{e}+\mu\frac{\partial\mathbf{h}}{\partial t} &= -\mathbf{j}^m, &\text{(4.3a)}\\ -\nabla\times\mathbf{h}+\sigma\mathbf{e} &= -\mathbf{j}^e, &\text{(4.3b)}\end{aligned}$$

where the electric and magnetic current source fields are now given by $\mathbf{j}^e$ and $\mathbf{j}^m$, respectively. Both types of current source fields will describe the sources of the migrated fields at a later stage. Solution to Equations (4.3) are formally written in terms of the electric and magnetic excitation currents by the integral representations [*Felsen and Marcuvitz*, 1973]

$$\begin{aligned}\mathbf{e}(\mathbf{r},t) &= \int_{V'}\int_0^t \mathcal{G}_{11}(\mathbf{r},t|\mathbf{r}',t')\cdot\mathbf{j}^e(\mathbf{r}',t')dt'd\mathbf{r}'\\ &+ \int_{V'}\int_0^t \frac{\mathcal{G}_{12}(\mathbf{r},t|\mathbf{r}',t')}{\mu(\mathbf{r}')}\cdot\mathbf{j}^m(\mathbf{r}',t')dt'd\mathbf{r}', &\text{(4.4a)}\\ \mathbf{h}(\mathbf{r},t) &= \int_{V'}\int_0^t \mathcal{G}_{21}(\mathbf{r},t|\mathbf{r}',t')\cdot\mathbf{j}^e(\mathbf{r}',t')dt'd\mathbf{r}'\\ &+ \int_{V'}\int_0^t \frac{\mathcal{G}_{22}(\mathbf{r},t|\mathbf{r}',t')}{\mu(\mathbf{r}')}\cdot\mathbf{j}^m(\mathbf{r}',t')dt'd\mathbf{r}'. &\text{(4.4b)}\end{aligned}$$

For the Green dyadics $\mathcal{G}_{ij}(\mathbf{r},t|\mathbf{r}',t')$, causality implies that

$$\mathcal{G}_{ij}(\mathbf{r},t|\mathbf{r}',t') \equiv 0, \quad t \le t'. \tag{4.5}$$

The Green dyadic component $\mathcal{G}_{11}(\mathbf{r},t|\mathbf{r}',t')\cdot\mathbf{u}'$ and $\mathcal{G}_{21}(\mathbf{r},t|\mathbf{r}',t')\cdot\mathbf{u}'$ represent the vector electric and magnetic fields, respectively, at $\mathbf{r},t$, produced by a unit electric current density at $\mathbf{r}',t'$. The excitation acts in the direction of the unit vector $\mathbf{u}'$. Similarly, $\mathcal{G}_{12}(\mathbf{r},t|\mathbf{r}',t')\cdot\mathbf{u}'$ and $\mathcal{G}_{22}(\mathbf{r},t|\mathbf{r}',t')\cdot\mathbf{u}'$ propagate the electric and magnetic response, respectively, of a unit magnetic current density at $\mathbf{r}',t'$ in the direction $\mathbf{u}'$ [*Felsen and Marcuvitz,* 1973]. The four dyadics in Equations (4.4) satisfy the following first–order equations

$$\begin{aligned}
\nabla\times\mathcal{G}_{11}+\mu\frac{\partial\mathcal{G}_{21}}{\partial t} &= 0, &\text{(4.6a)}\\
-\nabla\times\mathcal{G}_{21}+\sigma\mathcal{G}_{11} &= -I\delta(\mathbf{r}-\mathbf{r}')\delta(t-t'), &\text{(4.6b)}\\
\nabla\times\mathcal{G}_{12}+\mu\frac{\partial\mathcal{G}_{22}}{\partial t} &= -I\mu(\mathbf{r})\delta(\mathbf{r}-\mathbf{r}')\delta(t-t'), &\text{(4.6c)}\\
-\nabla\times\mathcal{G}_{22}+\sigma\mathcal{G}_{12} &= 0, &\text{(4.6d)}
\end{aligned}$$

where I denotes the identity dyadic.

The backpropagation of the data residuals involves an adjoint–field problem [*McGillivray and Oldenburg,* 1990; *McGillivray et al.,* 1994]. The adjoint field differs from the original field defined by Equations (4.3) in that it is reversed in both space and time, because an ingoing wave solution rather than the characteristic outgoing wave solution is admitted. As mentioned in the previous section, the excitation of the backpropagated fields takes place at the locations where data errors originate from, these are the receiver positions. Adjoint and original fields are connected by the reciprocity relation for transient EM fields [*Hohmann,* 1988], formally written as

$$\mathcal{G}^{+}_{ij}(\mathbf{r}',t'|\mathbf{r},t) \equiv \tilde{\mathcal{G}}_{ji}(\mathbf{r},t|\mathbf{r}',t'), \tag{4.7}$$

where $\mathcal{G}^{+}_{ij}$ propagates an adjoint field and $\tilde{\mathcal{G}}_{ji}$ represents the transpose of a dyadic [*Wang et al.,* 1994]. The time–reversed field propagation indicates the anti–causality of the adjoint Green dyadics, specifically

$$\mathcal{G}^{+}_{ij}(\mathbf{r},t|\mathbf{r}',t') \equiv 0, \quad t \ge t'. \tag{4.8}$$

The adjoint fields are representable in a form similar to that in Equations (4.4),

$$\begin{aligned}
\mathbf{e}^{+}(\mathbf{r},t) &= \int_V\int_0^t \mathcal{G}^{+}_{11}(\mathbf{r},t|\mathbf{r}',t')\cdot\mathbf{j}^{e}(\mathbf{r}',t')dt'd\mathbf{r}'\\
&+ \int_V\int_0^t \frac{\mathcal{G}^{+}_{12}(\mathbf{r},t|\mathbf{r}',t')}{\mu(\mathbf{r}')}\cdot\mathbf{j}^{m}(\mathbf{r}',t')dt'd\mathbf{r}', &\text{(4.9a)}\\
\mathbf{h}^{+}(\mathbf{r},t) &= \int_V\int_0^t \mathcal{G}^{+}_{21}(\mathbf{r},t|\mathbf{r}',t')\cdot\mathbf{j}^{e}(\mathbf{r}',t')dt'd\mathbf{r}'\\
&+ \int_V\int_0^t \frac{\mathcal{G}^{+}_{22}(\mathbf{r},t|\mathbf{r}',t')}{\mu(\mathbf{r}')}\cdot\mathbf{j}^{m}(\mathbf{r}',t')dt'd\mathbf{r}'. &\text{(4.9b)}
\end{aligned}$$

The reversal of the space–time coordinates for the adjoint fields leads to the following relations corresponding to Equations (4.6),

$$\begin{aligned}
-\nabla \times \mathcal{G}_{11}^{+} - \mu \frac{\partial \mathcal{G}_{21}^{+}}{\partial t} &= 0, && (4.10a)\\
\nabla \times \mathcal{G}_{21}^{+} + \sigma \mathcal{G}_{11}^{+} &= -I\delta(\mathbf{r}-\mathbf{r}')\delta(t-t'), && (4.10b)\\
-\nabla \times \mathcal{G}_{12}^{+} - \mu \frac{\partial \mathcal{G}_{22}^{+}}{\partial t} &= -I\mu(\mathbf{r})\delta(\mathbf{r}-\mathbf{r}')\delta(t-t'), && (4.10c)\\
\nabla \times \mathcal{G}_{22}^{+} + \sigma \mathcal{G}_{12}^{+} &= 0. && (4.10d)
\end{aligned}$$

These equations indicate the principal difference between seismic and EM migration. The migration of seismic wavefields employs the same wave equation as for forward propagation [*Tarantola*, 1984], whereas the backpropagation of diffusive EM fields involves the adjoint Maxwell's equations, where both space and time coordinates are sign–reversed.

Reciprocal connection of the Green dyadics

At this point, it needs to be emphasized that both $\mathcal{G}$ and $\mathcal{G}^{+}$ always propagate the impulse response of a field. Complications with reciprocity arise when $i \neq j$, that is the electric field response due to a magnetic dipole source or vice versa is considered. The reason can be found in the time–domain reciprocity relationship written in terms of the electric and magnetic source moments D and M, respectively [*Ward and Hohmann*, 1988],

$$D = -\mu M \frac{\partial}{\partial t}. \qquad (4.11)$$

Its practical meaning is that the magnetic field impulse response for an electric source is equivalent to the electric field step response for a magnetic source [*Hördt*, 1998]. This is a critical point not taken into account by *Wang et al.* [1994], when deriving the gradient specifications that involve the reciprocal relationship between electric/magnetic responses for magnetic/electric sources. The aspect was not discussed by the authors, because their presented synthetic data inversions required only the dyadic for an electric response due to an electric source type, where no such complications arise. To summarize the reciprocal connection between the four dyadics and its adjoints,

$$\begin{aligned}
\mathcal{G}_{11}^{+}(\mathbf{r}',t'|\mathbf{r},t) &= \tilde{\mathcal{G}}_{11}(\mathbf{r},t|\mathbf{r}',t'), && (4.12a)\\
\mathcal{G}_{12}^{+}(\mathbf{r}',t'|\mathbf{r},t) &= -\mu(\mathbf{r})\frac{\partial}{\partial t}\tilde{\mathcal{G}}_{21}(\mathbf{r},t|\mathbf{r}',t'), && (4.12b)\\
\mu(\mathbf{r}')\frac{\partial}{\partial t'}\mathcal{G}_{21}^{+}(\mathbf{r}',t'|\mathbf{r},t) &= \tilde{\mathcal{G}}_{12}(\mathbf{r},t|\mathbf{r}',t'), && (4.12c)\\
\mu(\mathbf{r}')\mathcal{G}_{22}^{+}(\mathbf{r}',t'|\mathbf{r},t) &= \mu(\mathbf{r})\tilde{\mathcal{G}}_{22}(\mathbf{r},t|\mathbf{r}',t'). && (4.12d)
\end{aligned}$$

To gain a deeper understanding of these reciprocity laws, consider first Equation (4.12a). Each component of this tensor equation describes an equivalency between two electric field components at $\mathbf{r}',t'$ and $\mathbf{r},t$ that arise from two electric dipole sources located at $\mathbf{r}$ and $\mathbf{r}'$ with an impulse excitation at t and t', respectively. A similar explanation for magnetic source and receiver types holds for (4.12d), where the responses need to be scaled by the magnetic permeability at the respective location. Equation (4.12b) equates the time derivative of the magnetic field impulse response that arises from an electric dipole source to the electric field impulse response that arises from a magnetic dipole source. Explanation of Equation (4.12c) is similar to (4.12b), except for a sign change, which is required because the field evolves in reverse time, starting at time t. When (4.12b) is integrated over time t and (4.12c) is integrated over time t', it follows

$$\begin{aligned} {}^{step}\mathcal{G}^{+}_{12}(\mathbf{r}',t'|\mathbf{r},t) &= \mu(\mathbf{r})\,\tilde{\mathcal{G}}_{21}(\mathbf{r},t|\mathbf{r}',t'), && (4.13a)\\ -\mu(\mathbf{r}')\,\mathcal{G}^{+}_{21}(\mathbf{r}',t'|\mathbf{r},t) &= {}^{step}\tilde{\mathcal{G}}_{12}(\mathbf{r},t|\mathbf{r}',t'), && (4.13b) \end{aligned}$$

where

$$\begin{aligned} {}^{step}\mathcal{G}^{+}_{12}(\mathbf{r}',t'|\mathbf{r},t) &= \int_{t}^{t'} \mathcal{G}^{+}_{12}(\mathbf{r}',t'|\mathbf{r},t)dt,\\ {}^{step}\tilde{\mathcal{G}}_{12}(\mathbf{r},t|\mathbf{r}',t') &= \int_{t'}^{t} \tilde{\mathcal{G}}_{12}(\mathbf{r},t|\mathbf{r}',t')dt. \end{aligned}$$

The derivation of (4.13a) from (4.12b) is exemplified in Appendix A.3 in order to clarify the change of the sign.

4.3 Specification of the gradients

As mentioned in the introduction of this chapter, the presented iterative imaging technique is based on information about the gradient of an error functional rather than on direct solutions obtained by matrix inversion methods. With both the idea of EM migration and the formal representation of the EM field by means of Green functions and its adjoints in place, the specifications for an efficient gradient calculation are now derived.

The inverse problem introduced earlier in Section 2.1.2 is first reformulated in terms of another form of the error functional[3]

$$\begin{aligned} \phi(\mathbf{m}) &= \frac{1}{2}\sum_{j}\sum_{i}\int_{0}^{T}[\mathbf{d}^{o}(\mathbf{r}_i,t;\mathbf{s}_j)-\mathbf{d}^{p}(\mathbf{r}_i,t;\mathbf{s}_j)]^2dt\\ &= \frac{1}{2}\sum_{j}\sum_{i}\int_{0}^{T}\delta\mathbf{d}^{o}(\mathbf{r}_i,t;\mathbf{s}_j)\cdot\delta\mathbf{d}^{o}(\mathbf{r}_i,t;\mathbf{s}_j)dt. && (4.14) \end{aligned}$$

The difference $\delta\mathbf{d}^o$ between a set of observed an predicted data $\mathbf{d}^o$ and $\mathbf{d}^p$, respectively, is matched in a least–squares sense, which corresponds to finding a model $\mathbf{m}$ that minimizes ϕ. The summation is carried out for all source positions $\mathbf{s}_j$ and its respective receiver positions $\mathbf{r}_i$. For now, it shall be assumed that all receivers are assigned to a single transmitter. The measurements and its respective predictions are sampled over the time range $t = 0$ to $t = T$, where $t = 0$ denotes the shut–off time of a source at steady state. The error funtional is connected with a model guess by the implicit dependence of the predicted data on $\mathbf{m}$, which may represent a conductivity or magnetic permeability distribution. In this thesis, only electrical conductivities are considered as variable model parameters, thus $\mathbf{m} = \sigma$.

---

[3] For simplicity the formal notation of a vector dot product $\mathbf{a}^T\mathbf{b}$ is neglected.

To obtain the gradient of the error funtional ϕ with respect to the model conductivities, denoted by γ_σ, consider a small perturbation $\delta\sigma$ at the point $\mathbf{r}'$ in model space. The relationship between the gradient and the perturbed quantities is given by *Wang et al.* [1994],

$$\delta\phi = \phi(\sigma+\delta\sigma) - \phi(\sigma) \approx \int_{V'} \gamma_\sigma(\mathbf{r}')\delta\sigma(\mathbf{r}')d\mathbf{r}' \tag{4.15}$$

and can be explained as follows. The gradient γ_σ represents a vector, where each component is assigned to a model cell k with $k = 1,...,M$ and M the total number of model elements belonging to the inversion domain V'. It represents a differential quantity, because there is no cell volume associated with all points of V' where it is calculated. To obtain the change in the error functional $\delta\phi$ with respect to conductivity changes $\delta\sigma$ in a cell, it has to be integrated over the volume of that cell. Equation (4.15) includes the assumption that the error functional is Fréchet differentiable, that is the neglected remainder term of the approximation is of second order in $\delta\sigma$ [*Chave*, 1984; *Boerner and West*, 1989; *Wang et al.*, 1994].

In Equation (4.14), the change in the error functional originates from the change in the predicted data $\delta\mathbf{d}$, hence the perturbed quantity $\delta\phi$ is

$$\begin{aligned}
\delta\phi &= \frac{1}{2}\sum_i \int_0^T \left[\left(\mathbf{d}^o - (\mathbf{d}^p + \delta\mathbf{d})\right)^2 - \left(\mathbf{d}^o - \mathbf{d}^p\right)^2\right] dt \\
&= -\sum_i \int_0^T \left(\delta\mathbf{d}^o \cdot \delta\mathbf{d} - \frac{1}{2}\delta\mathbf{d}\cdot\delta\mathbf{d}\right) dt \\
&\approx -\sum_i \int_0^T \delta\mathbf{d}^o \cdot \delta\mathbf{d}\, dt
\end{aligned} \tag{4.16}$$

Note that the second order term $\delta\mathbf{d}\cdot\delta\mathbf{d}$ is also of second order in $\delta\sigma$ and thus has been neglected. Now the perturbed quantities $\delta\mathbf{d}$ and $\delta\sigma$ will be related to the field solutions given by Equations (4.4). As indicated by Equation (4.1), a scattered field $\delta\mathbf{d}$ can be connected with a model perturbation $\delta\sigma$. In order to obtain the scattered field solution, consider the perturbed quantities

$$\begin{aligned}
\sigma &\rightarrow \sigma + \delta\sigma, \\
\mu &\rightarrow \mu + \delta\mu, \\
\mathbf{e} &\rightarrow \mathbf{e} + \delta\mathbf{e}, \\
\mathbf{h} &\rightarrow \mathbf{h} + \delta\mathbf{h}.
\end{aligned}$$

By rewriting Maxwell's Equations (4.3) using these perturbed quantities and then subtracting the corresponding equations for the non–perturbed state, it follows [*Wang et al.*, 1994]

$$\sigma\delta\mathbf{e} - \nabla\times\delta\mathbf{h} = -\delta\sigma\mathbf{e}, \tag{4.17a}$$

$$\nabla\times\delta\mathbf{e} + \mu\frac{\partial}{\partial t}\delta\mathbf{h} = -\delta\mu\frac{\partial}{\partial t}\mathbf{h}, \tag{4.17b}$$

where second order terms (products of two perturbed quantities) are neglected.

At this point, it has to be distinguished between different data types contained in $\delta\mathbf{d}^o$ and $\delta\mathbf{d}$. These can be electric fields, magnetic fields or the time derivative of magnetic fields (voltages). For causal source fields, *Wang et al.* [1994] show that different gradient specifications result for electric and magnetic fields. In this work, the gradients for electric fields and voltages are derived for the more general case of non–causal source types. It will become clear that the resulting gradients comprise the gradient specifications for causal sources.

4.3.1 Gradient specification for electric field data

A comparison of Equations (4.17) for perturbed fields with the formal field solutions in terms of Green dyadics (Equation 4.4a) yields

$$\begin{aligned}\delta\mathbf{e}(\mathbf{r},t) &= \int_{V'}\int_{-\infty}^{t} \mathcal{G}_{11}(\mathbf{r},t|\mathbf{r}',t')\cdot\mathbf{e}(\mathbf{r}',t')\delta\sigma(\mathbf{r}')dt'd\mathbf{r}' \\ &+ \int_{V'}\int_{-\infty}^{t} \frac{\mathcal{G}_{12}(\mathbf{r},t|\mathbf{r}',t')}{\mu(\mathbf{r}')}\cdot\frac{\partial}{\partial t'}\mathbf{h}(\mathbf{r}',t')\delta\mu(\mathbf{r}')dt'd\mathbf{r}'. \end{aligned} \tag{4.18}$$

From here, the second integral is not taken into account, because it only needs to be considered when perturbations of the magnetic permeability are treated. By setting $\delta\mu(\mathbf{r}') = 0$ the second integral vanishes. Note that the existence of non–causal source fields implies that the lower bound of the time integral is replaced by a value of $t = -\infty$ instead of $t = 0$. Substituting Equation (4.18) into Equation (4.16), where the general variables $\delta\mathbf{d}^o$ and $\delta\mathbf{d}$ for the data residuals and the scattered field, respectively, are replaced by its electric field representations, one obtains

$$\delta\phi = -\sum_i \int_0^T \delta\mathbf{e}^o(\mathbf{r}_i,t)\cdot\int_{V'}\int_{-\infty}^{t} \mathcal{G}_{11}(\mathbf{r}_i,t|\mathbf{r}',t')\cdot\mathbf{e}(\mathbf{r}',t')\delta\sigma(\mathbf{r}')dt'd\mathbf{r}'dt. \tag{4.19}$$

By a comparison of Equation (4.19) with (4.15) it can be seen that the gradient is given by

$$\gamma_\sigma^e(\mathbf{r}') = -\sum_i \int_0^T \delta\mathbf{e}^o(\mathbf{r}_i,t)\cdot\int_{-\infty}^{t} \mathcal{G}_{11}(\mathbf{r}_i,t|\mathbf{r}',t')\cdot\mathbf{e}(\mathbf{r}',t')dt'dt, \tag{4.20}$$

where γ_σ^e indicates that this specification belongs to electric field data. Reverting back to the basic outline of EM migration (Section 4.1), it can be seen that Equation (4.20) in principle contains the convolution that would yield differential sensitivities (with no volume associated with each point) over the model domain $\mathbf{r}'$. Hence, the gradient can simply be evaluated by integrating the product of the data differences $\delta\mathbf{e}^o$ at $\mathbf{r}_i$ and the corresponding sensitivities over the time interval of the observed data. The difference to the integral in Equation (4.2) is that the reciprocal relationship has not yet been applied to (4.20). Therefore, the realization of Equation (4.20) would require one forward solution to compute the fields in the current model and as many solutions as there are image points in the model domain in order to get the sensitivities. This is impractical with a large number of image points. Instead, (4.20) is now turned into a form that establishes the relationship to migration techniques. This involves the treatment of the residuals $\delta\mathbf{e}^o$ as sources of a residual or backpropagated field as can be seen in the following derivation.

First, as clarified in detail in Appendix A.4, the order of time integrations in (4.20) can be reversed to

$$\gamma_\sigma^e(\mathbf{r}') = -\sum_i \int_{-\infty}^{T}\int_{t'}^{T} \delta\mathbf{e}^o(\mathbf{r}_i,t)\,\mathcal{G}_{11}(\mathbf{r}_i,t|\mathbf{r}',t')\cdot\mathbf{e}(\mathbf{r}',t')dt\,dt'. \tag{4.21}$$

Now the reciprocity relationship as given by Equation (4.12a) is applied,

$$\gamma_\sigma(\mathbf{r}') = -\sum_i \int_{-\infty}^{T} \int_{t'}^{T} \mathbf{e}(\mathbf{r}',t')\, \mathcal{G}_{11}^{+}(\mathbf{r}',t'|\mathbf{r}_i,t) \cdot \delta\mathbf{e}^o(\mathbf{r}_i,t)\,dt\,dt'. \tag{4.22}$$

This already indicates that the residual field propagated by the adjoint Green function originates from the receiver positions $\mathbf{r}_i$, which now act as sources with the source excitation given by $\delta\mathbf{e}^o$. In order to avoid confusion between the sources of the residual field at the receivers and the source given by the grounded–wire transmitter, the latter one will be referred to as external or primary source in the following. The incident electric field $\mathbf{e}(\mathbf{r}',t')$ can be placed outside the time integration over t. A further rearrangement of the summation over the source positions of the residual field yields

$$\gamma_\sigma^e(\mathbf{r}') = \int_{-\infty}^{T} \mathbf{e}(\mathbf{r}',t') \cdot \sum_i \int_{T}^{t'} \mathcal{G}_{11}^{+}(\mathbf{r}',t'|\mathbf{r}_i,t) \cdot \delta\mathbf{e}^o(\mathbf{r}_i,t)\,dt\,dt'. \tag{4.23}$$

The inner integral and the summation over the receivers is replaced by

$$\mathbf{e}_b(\mathbf{r}',t'|\delta\mathbf{e}^o) = \sum_i \int_{T}^{t'} \mathcal{G}_{11}^{+}(\mathbf{r}',t'|\mathbf{r}_i,t) \cdot \delta\mathbf{e}^o(\mathbf{r}_i,t)\,dt, \tag{4.24}$$

which represents the residual or backpropagated electric field at $\mathbf{r}',t'$ due to a source excitation quantified by the data residuals $\delta\mathbf{e}^o$ at the receiver positions $\mathbf{r}_i$. The data residuals $\delta\mathbf{e}^o$ can be regarded as electric current sources, radiating from the sensor positions $\mathbf{r}_i$ in reverse time, as indicated by the lower integration boundary T (the time of the latest measurements). The reversal of the time order of propagation for $\mathbf{e}_b$ is also inherent in the anticausal definition of the adjoint Green dyadic in Equation (4.24). The FD algorithm described in Chapter 3 is capable of simulating the field response arising from multiple sources distributed over the model. Thus, only a single simulation is needed for the computation of $\mathbf{e}_b$. Finally, the gradient is specified in the compact form

$$\gamma_\sigma^e(\mathbf{r}') = \int_{-\infty}^{T} \mathbf{e}(\mathbf{r}',t') \cdot \mathbf{e}_b(\mathbf{r}',t'|\delta\mathbf{e}^o)\,dt'. \tag{4.25}$$

In practice, the gradient vector is computed by extracting the incident and the backpropagated field at each of the M cells comprising an inversion domain and carrying out the correlation of the fields at each cell.

A closer view of the backpropagated fields

To further understand the formal specification of the backpropagated field in (4.24), consider Equations (4.9). In fact, the formal adjoint electric field $\mathbf{e}^+$ is directly related to the field $\mathbf{e}_b$ in (4.24). Apart from the volume integration, the only difference is that the electric current source field $\mathbf{j}^e$ is given by the data residuals $\delta\mathbf{e}^o$ distributed over the receiver points $\mathbf{r}_i$. Now the Green dyadic $\mathcal{G}_{12}^{+}$ in (4.9a) indicates that $\mathbf{e}_b$ also has a magnetic part. The magnetic current source field $\mathbf{j}^m$ can be given by either magnetic field or voltage residuals. In the presence of voltage data, the corresponding backpropagated electric field

$$\mathbf{e}_b(\mathbf{r}',t'|\delta\mathbf{v}^o) = \sum_i \int_{T}^{t'} \mathcal{G}_{12}^{+}(\mathbf{r}',t'|\mathbf{r}_i,t) \cdot \delta\mathbf{v}^o(\mathbf{r}_i,t)\,dt \tag{4.26}$$

is sourced by the voltage residuals $\delta\mathbf{v}^o$. Similarly, in the presence of magnetic field data, with the residuals given by $\delta\mathbf{h}^o$, it follows

$$\mathbf{e}_b^{step}(\mathbf{r}',t'|\delta\mathbf{h}^o) = \sum_i \int_T^{t'} \frac{{}^{step}\mathcal{G}_{12}^{+}(\mathbf{r}',t'|\mathbf{r}_i,t)}{\mu(\mathbf{r}_i)} \cdot \delta\mathbf{h}^o(\mathbf{r}_i,t)dt. \tag{4.27}$$

It turns out that the two types of fields in (4.26) and (4.27) are related to each other through a simple time differentiation. This crucial detail results from the reciprocity relationship between electric and magnetic fields discussed in connection with Equations (4.13). Equation (4.27) is involved in the conductivity gradient specification for magnetic field residuals (*Newman*, pers. comm.). For the sake of completeness the backpropagated field types related to the adjoint magnetic field $\mathbf{h}^+$ are specified:

$$\mathbf{h}_b(\mathbf{r}',t'|\delta\mathbf{e}^o) = \sum_i \int_T^{t'} \mathcal{G}_{21}^{+}(\mathbf{r}',t'|\mathbf{r}_i,t) \cdot \delta\mathbf{e}^o(\mathbf{r}_i,t)dt, \tag{4.28a}$$

$$\mathbf{h}_b(\mathbf{r}',t'|\delta\mathbf{v}^o) = \sum_i \int_T^{t'} \mathcal{G}_{22}^{+}(\mathbf{r}',t'|\mathbf{r}_i,t) \cdot \delta\mathbf{v}^o(\mathbf{r}_i,t)dt, \tag{4.28b}$$

$$\mathbf{h}_b(\mathbf{r}',t'|\delta\mathbf{h}^o) = \sum_i \int_T^{t'} \frac{\mathcal{G}_{22}^{+}(\mathbf{r}',t'|\mathbf{r}_i,t)}{\mu(\mathbf{r}_i)} \cdot \delta\mathbf{h}^o(\mathbf{r}_i,t)dt. \tag{4.28c}$$

These fields are involved in the derivation of the gradients for magnetic permeability. This is not further outlined in this work.

Treatment of the non–causal gradient part

In practice, the actual computation of Equation (4.25) would require a backpropagation beyond time $t = 0$ in order to account for the correlation with the non–causal part of the incident field. This would need to be performed until the contribution to the correlation integral vanishes due to a sufficient decay of the backpropagated field. To avoid this significant disadvantage, it is computationally convenient to formally split up the gradient in Equation (4.25) such that

$$\gamma_\sigma^e(\mathbf{r}') = \int_0^T \mathbf{e}(\mathbf{r}',t') \cdot \mathbf{e}_b(\mathbf{r}',t'|\delta\mathbf{e}^o)dt' + \int_{-\infty}^0 \mathbf{e}^{DC}(\mathbf{r}') \cdot \mathbf{e}_b(\mathbf{r}',t'|\delta\mathbf{e}^o)dt', \tag{4.29}$$

where $\mathbf{e}(\mathbf{r}',t') = \mathbf{e}^{DC}(\mathbf{r}')$ for $t' \leq 0$. The second integral is further split up in order to obtain the correct forms for a backpropagation starting at the latest measurement time T,

$$\begin{aligned} \gamma_\sigma^e(\mathbf{r}') &= \int_0^T \mathbf{e}(\mathbf{r}',t') \cdot \mathbf{e}_b(\mathbf{r}',t'|\delta\mathbf{e}^o)dt' \\ &- \mathbf{e}^{DC}(\mathbf{r}') \cdot \int_0^T \mathbf{e}_b(\mathbf{r}',t'|\delta\mathbf{e}^o)dt' + \mathbf{e}^{DC}(\mathbf{r}') \cdot \int_{-\infty}^T \mathbf{e}_b(\mathbf{r}',t'|\delta\mathbf{e}^o)dt'. \end{aligned} \tag{4.30}$$

The constant DC electric field, $\mathbf{e}^{DC}(\mathbf{r}')$ could be brought outside the integration. This field can be determined by solving Maxwells's equations in the steady state limit as described in Section 3.1.5. For reasons mentioned soon, the integral of the last term in Equation (4.30) is related to a backpropagated DC electric field. First, consider the adjoint Maxwell equations, which are satisfied by the backpropagated fields for electric sources,

$$\sigma \mathbf{e}_b + \nabla \times \mathbf{h}_b = -\sum_i \delta \mathbf{e}^o(\mathbf{r}_i, t)\delta(\mathbf{r} - \mathbf{r}_i), \tag{4.31a}$$

$$\nabla \times \mathbf{e}_b + \mu \frac{\partial \mathbf{h}_b}{\partial t} = 0. \tag{4.31b}$$

These equations follow directly from Equations (4.10a,b), (4.24) and (4.28a) and are now integrated from the time range $t = -\infty$ to $t = T$,

$$\sigma \int_{-\infty}^{T} \mathbf{e}_b \, dt + \nabla \times \int_{-\infty}^{T} \mathbf{h}_b \, dt = -\sum_i \int_{-\infty}^{T} \delta \mathbf{e}^o(\mathbf{r}_i, t)\delta(\mathbf{r} - \mathbf{r}_i) dt \tag{4.32a}$$

$$\nabla \times \int_{-\infty}^{T} \mathbf{e}_b \, dt + \mu \int_{-\infty}^{T} \frac{\partial \mathbf{h}_b}{\partial t} dt = 0. \tag{4.32b}$$

Note that the integral from $t = -\infty$ to $t = 0$ vanishes for the source term in Equation (4.32a), because $\delta \mathbf{e}^o(\mathbf{r}_i, t) = 0$ for $t < 0$. Also, $\mathbf{h}_b(T) = 0$ and $\mathbf{h}_b(-\infty) = 0$ and introducing the backpropagated DC electric and magnetic field by

$$\begin{aligned} \mathbf{e}_b^{DC} &= \int_{-\infty}^{T} \mathbf{e}_b \, dt, \\ \mathbf{h}_b^{DC} &= \int_{-\infty}^{T} \mathbf{h}_b \, dt, \end{aligned}$$

one can simplify Equations (4.32) to

$$\sigma \mathbf{e}_b^{DC} + \nabla \times \mathbf{h}_b^{DC} = -\sum_i \int_{0}^{T} \delta \mathbf{e}^o(\mathbf{r}_i, t)\delta(\mathbf{r} - \mathbf{r}_i) dt \tag{4.33a}$$

$$\nabla \times \mathbf{e}_b^{DC} = 0. \tag{4.33b}$$

To avoid confusion, it shall be emphasized that the fields $\mathbf{e}_b^{DC}$ and $\mathbf{h}_b^{DC}$ are causal fields, in contrast to the non–causal DC fields arising from the external source. However, the fact that they are formally backpropagated beyond time zero to the DC state of the incident fields suggests to name them after the incident DC fields.

Similar to the incident DC electric field, the integrated backpropagated electric field can be written as the gradient of a scalar potential φ_b, because $\nabla \times \mathbf{e}_b^{DC} = 0$. Thus $\mathbf{e}_b^{DC}$ is obtained by solving

$$\nabla \cdot (\sigma \nabla \varphi_b) = -\nabla \cdot \sum_i \int_{0}^{T} \delta \mathbf{e}^o(\mathbf{r}_i, t)\delta(\mathbf{r} - \mathbf{r}_i) dt.$$

The equation represents a 3D Poisson problem similar to the one for the incident DC electric field (Equation 3.15), yet with a different source field, given by the data differences integrated over the time interval from 0 to T. It can be solved by the same algorithm employed for the forward case, as outlined in detail in Appendix A.2.

Now the gradient for electric field data is rewritten in the form in which it is actually implemented,

$$\begin{aligned} \gamma_\sigma^e(\mathbf{r}') &= \int_{0}^{T} \mathbf{e}(\mathbf{r}', t') \cdot \mathbf{e}_b(\mathbf{r}', t' | \delta \mathbf{e}^o) dt' \\ &- \mathbf{e}^{DC}(\mathbf{r}') \cdot \int_{0}^{T} \mathbf{e}_b(\mathbf{r}', t' | \delta \mathbf{e}^o) dt' + \mathbf{e}^{DC}(\mathbf{r}') \cdot \mathbf{e}_b^{DC}(\mathbf{r}' | \delta \mathbf{e}^o). \end{aligned} \tag{4.34}$$

Note that this representation reverts back to the causal form, that is only the first integral given by *Wang et al.* [1994], when $\mathbf{e}^{DC}$ vanishes. In addition to the solution of the Poisson problem in order to evaluate the third term, it is also necessary to integrate the backpropagated electric field for the second term. This is not difficult to implement, because the integral $\int_0^T \mathbf{e}_b(\mathbf{r}',t'|\delta\mathbf{e}^o)dt'$ can be calculated as a by–product during backpropagation of the electric field. Nevertheless, this integration could also be eliminated by expressing Equation (4.34) as

$$\gamma_\sigma^e(\mathbf{r}') = -\int_0^T \mathbf{e}^{on}(\mathbf{r}',t')\cdot\mathbf{e}_b(\mathbf{r}',t'|\delta\mathbf{e}^o)dt' + \mathbf{e}^{DC}(\mathbf{r}')\cdot\mathbf{e}_b^{DC}(\mathbf{r}'|\delta\mathbf{e}^o),$$

where $\mathbf{e}^{on}(\mathbf{r}',t') = \mathbf{e}^{DC}(\mathbf{r}') - \mathbf{e}(\mathbf{r}',t')$ represents a causal field generated by a turn–on waveform of the transmitter. However, this way of implementation is less favorable, because subtractive cancellation can lead to a loss of accuracy in $\mathbf{e}^{on}(\mathbf{r}',t')$ at late times (*Newman*, pers. comm.).

4.3.2 Gradient specifications for voltage and combined data

A derivation of the gradient γ_σ^v for voltage data is similar to the gradient for electric fields and is given in detailed form in Appendix A.5. Here, its final form is given,

$$\gamma_\sigma^v(\mathbf{r}') = \int_0^T \mathbf{e}(\mathbf{r}',t')\cdot\mathbf{e}_b(\mathbf{r}',t'|\delta\mathbf{v}^o)dt' - \mathbf{e}^{DC}(\mathbf{r}')\int_0^T \mathbf{e}_b(\mathbf{r}',t'|\delta\mathbf{v}^o)dt', \qquad (4.35)$$

where the corresponding backpropagated electric field has already been defined by (4.26). Compared to the derivation of the gradient for electric field data, the major difference results from using Equation (4.12b) instead of (4.12a) when applying the reciprocity relation. By comparing (4.35) with (4.34), one further notices that no backpropagated DC electric field is required for γ_σ^v. As also outlined in Appendix A.5, this owes to the fact that the voltages are causal, i.e. vanish in the DC state of the primary source.

Consider a TEM measurement, where both electric field and voltage data is recorded. The inspection of (4.34) and (4.35) shows that both can be computed jointly. This is realized by the capability of the FD time–stepping scheme presented in Chapter 3 to superimpose multiple electric and magnetic types of sources. It allows for additional computational efficiencies in the case of both data types present. At this point, the extension of the gradient specification to include multiple primary transmitters shall also be given. The required additional summation over all primary source positions $\mathbf{s}_j$ is straightforward. Finally, the combined gradient is specified as

$$\begin{aligned}\gamma_\sigma^{e+v}(\mathbf{r}') \;&=\; \sum_j\int_0^T \mathbf{e}(\mathbf{r}',t';\mathbf{s}_j)\cdot\mathbf{e}_b(\mathbf{r}',t';\mathbf{s}_j)|\delta\mathbf{e}^o+\delta\mathbf{v}^o)dt' \\ &-\; \sum_j \mathbf{e}^{DC}(\mathbf{r}';\mathbf{s}_j)\cdot\int_0^T \mathbf{e}_b(\mathbf{r}',t';\mathbf{s}_j|\delta\mathbf{e}^o+\delta\mathbf{v}^o)dt' \\ &+\; \sum_j \mathbf{e}^{DC}(\mathbf{r}';\mathbf{s}_j)\cdot\mathbf{e}_b^{DC}(\mathbf{r}';\mathbf{s}_j|\delta\mathbf{e}^o). \qquad (4.36)\end{aligned}$$

For each source positions $\mathbf{s}_j$, the computation of the combined gradient still involves only two simulations, one forward simulation to compute the fields in the current model and one simulation for the backpropagation. However, this procedure needs to be carried out as often as there are primary sources.

4.4 Time–stepping backpropagated fields

The adjoint Maxwell equations for time–stepping the backpropagated fields arising from both electric and voltage data residuals follow from Equations (4.10), (4.24), (4.26), (4.28a) and (4.28b),

$$-\nabla\times\mathbf{e}_b-\mu\frac{\partial\mathbf{h}_b}{\partial t} = -\sum_i \mu(\mathbf{r}_i)\delta\mathbf{v}^o(\mathbf{r}_i,t)\delta(\mathbf{r}-\mathbf{r}_i), \tag{4.37a}$$

$$\nabla\times\mathbf{h}_b+\sigma\mathbf{e}_b-\gamma\frac{\partial\mathbf{e}_b}{\partial t} = -\sum_i \delta\mathbf{e}^o(\mathbf{r}_i,t)\delta(\mathbf{r}-\mathbf{r}_i). \tag{4.37b}$$

Note that the displacement term has also been taken into account in order to realize the DuFort–Frankel scheme explained in Section 3.1.3. As already indicated, the FD algorithm developed in Chapter 3 is employed for both propagation of the incident field forwards in time and backpropagation of the residual field. The incident field only involves electric current source fields impressed by the transmitter, whereas the residual fields arise from both electric field and voltage data residuals sourced at the receiver locations. The length of the source excitation is governed by the time interval covered by the data residuals.

The residual fields are initialized to zero at the time $t=T$ and stepped backwards in time until time zero is reached. Therefore, these fields are causal and the time–stepping scheme described in Section 3.1.2 is employed as no initial DC fields are involved. Consider the FD discretization exemplified by Equation (3.5) for the magnetic induction **b**. The discretization of (4.37a) yields similar expressions for the components of $\mathbf{b}_b$, yet the additional source term needs to be taken into account. In contrast to the forward propagation, the time–reversed propagation of the fields now involves rearranging the discretized form of (4.37a) such that $\mathbf{b}^{n-\frac{1}{2}}$ is updated from $\mathbf{b}^{n+\frac{1}{2}}$, thus

$$\mathbf{b}_b^{n-\frac{1}{2}} = \mathbf{b}_b^{n+\frac{1}{2}} + \Delta t_n\big(\nabla\times\mathbf{e}_b^n - \sum_i \mu(\mathbf{r}_i)\delta\mathbf{v}^o(\mathbf{r}_i)^n\big), \tag{4.38}$$

where the data difference $\delta\mathbf{v}^o$ at the required time t_n is obtained by interpolation. Similarly, discretizing (4.37b) using the same approximation for averages and central differences as explained in Section 3.1.2 yields

$$\mathbf{e}_b^n = \frac{2\gamma-\sigma\Delta t_n}{2\gamma+\sigma\Delta t_n}\mathbf{e}_b^{n+1} - \frac{2\Delta t_n}{2\gamma+\sigma\Delta t_n}\big(\nabla\times\mathbf{h}_b^{n+\frac{1}{2}} + \sum_i \delta\mathbf{e}^o(\mathbf{r}_i)^{n+\frac{1}{2}}\big). \tag{4.39}$$

Equations (4.38) and (4.39) also clarify how the data differences are fed in as magnetic and/or electric source terms at the FD grid positions given by the receivers at $\mathbf{r}_i$. As carried out for the primary source, the distribution of the data differences over the receivers is inversely interpolated onto the FD grid.

Comparing Equation (4.39) with (3.18) shows that the only principal difference is given by the sign of the second term on the right–hand side. Equation (3.18) describes a diffusing field that is decaying in forward time and growing in reverse time [*Wang et al.*, 1994], where a gradually increasing time step can be employed as outlined in Section 3.1.3. Numerical experiments have shown that for backpropagation a decreasing time step is adequate, because the fields revealed more rapid variations towards time zero. To be more specific, the initial time step is chosen such that the EM field retains its diffusive nature at the latest observed time T and the variable time step decreases according to Equation (3.7) as the simulation time decreases, until time zero is reached. The reason is possibly due to the fact that the adjoint Maxwell equations solved by the backpropagated fields describe the concentration of fields, in contrast to the diffusive nature of the fields propagated forwards in time. However, this aspect has not yet been sufficiently investigated.

4.5 Numerical gradient checks

For a numerical verification of the gradients a crosswell measurement configuration is considered. The FD grid used to simulate the underground has a number of $51 \times 39 \times 53$ nodes in the x, y and z direction, respectively. An electric dipole source of unit length is located at the horizontal position $x = 0$ m, $y = 0$ m and the vertical position $z = 0$ m and points into the y direction. The observed data is computed from a 5 Ωm homogeneous fullspace representing the true model. A single receiver is placed at the position $x = 100$ m, $y = 0$ m and $z = 0$ m. The predicted data and thus the data differences $\delta \mathbf{d}^o$ are produced by assuming a 10 Ωm homogeneous fullspace. The data is generated over the time range of 10^{-5} s to 10^{-3} s after the transmitter current switch–off, which is sufficient to cover the decay of the field at the receiver.

The gradient computed by backpropagation of the data differences is compared with the one obtained by a simple perturbation method. From Equation (4.16) it follows for a single component γ_{σ_k} of the gradient vector γ_σ

$$\gamma_{\sigma_k} = \frac{\delta\phi}{\delta\sigma_k} = -\int_0^T \delta\mathbf{d}^o(\mathbf{r},t) \cdot \frac{\delta\mathbf{d}(\mathbf{r},t)}{\delta\sigma_k} dt,$$

where $\delta\sigma_k$ with $k = 1,...,M$ denotes the conductivity perturbation of a single cell k of the model domain. As mentioned before, this involves the calculation of sensitivities. Therefore, each cell conductivity of the 10 Ωm homogeneous fullspace is perturbed by a value of 10 % in order to get the differences $\delta\mathbf{d}$ at the receiver position $\mathbf{r}$ with respect to the model perturbation $\delta\sigma_k$. The grid domain considered for the check comprises the $x - z$ plane through $y = 0$ between source and receiver with a vertical extent of 95 m. This involves 360 grid cells, each one with a size of $5 \times 5 \times 5$ m^3, and thus 360 gradient vector components to be verified.

The first gradient check involves only electric field data. For this check the backpropagation gradient is computed using Equation (4.34). The field component parallel to the transmitter is considered for the data residuals. The result is shown by the percentage difference plot in Figure 4.2a. Only absolute differences of the backpropagation gradient with respect to the perturbation gradient are shown. Away from the transmitter and receiver the differences are mainly below 1 %, thus showing a very good agreement. In the vicinity of both transmitter and receiver one observes the largest deviations with a maximum of 9 % reached near the transmitter. However, this still represents a tolerable difference. Larger deviations are observed when the backpropagated fields are sourced by voltage data as shown in Figure 4.2b. The result compares the gradient computed from Equation (4.35) with the perturbation method. The data residuals are computed from the voltage component that is parallel to the z direction. Differences up to 47 % occur in the vicinity of the receiver, whereas the space between $x = 30$ m and $x = 70$ m is dominated by deviations of only a few percent. The last gradient check involves sourcing the backpropagated fields by a combination of both electric field and voltage data, using Equation (4.36). Comparing the resulting differences in Figure 4.2c with the previous results, the combined data seems to produce an average of the results originating from the separate data sets. Here, a maximum difference of 26 % occurs, again near the receiver.

Better agreement between both types of gradients can be obtaind for all data types by refining the mesh near the receiver. The grid used for the shown results is characterized by a coarsening of the mesh starting beyond the receiver position at $x = 100$ m. Other gradient checks not shown here involved a refinement of the mesh in the vicinity of the receiver. For example, by refining the mesh near the receiver using 5 additional nodes in the x direction, the maximum difference in the gradients for vertical voltage data could be reduced by approximately a factor of two.

Here, the perturbation method was used for obtaining reference values for the backpropagation gradients. As indicated by Equation (4.2), other possibilities exist for computing the sensitivities for each cell and thus the reference values for the gradient. For another way to get the electric field sensitivity at the receiver position $\mathbf{r}$ for a given cell at $\mathbf{r}'$, one can implement Equation (4.2) by placing an electric dipole source of unit length with a source excitation given by the background electric field $\mathbf{e}_p(\mathbf{r}', t')$ at the cell position $\mathbf{r}'$. Here, the background electric field corresponds to the field generated by the external source in a 10 Ωm fullspace. Alternatively, using reciprocity, the electric dipole can be placed at the receiver at $\mathbf{r}$, now emitting an impulse signal. By convolution of the impulse response at $\mathbf{r}'$ with the background electric field, the sensitivity at $\mathbf{r}$ is again obtained. It turned out that the latter method yields better comparisons with the backpropagation gradients than the perturbation method. A reason is given by the fact that the perturbation of a cell conductivity always involves a finite quantity for both cell volume and parameter change, which is not the case with the convolution method. In other words, there exists more similarity between convolution and backpropagation method for computing gradients.

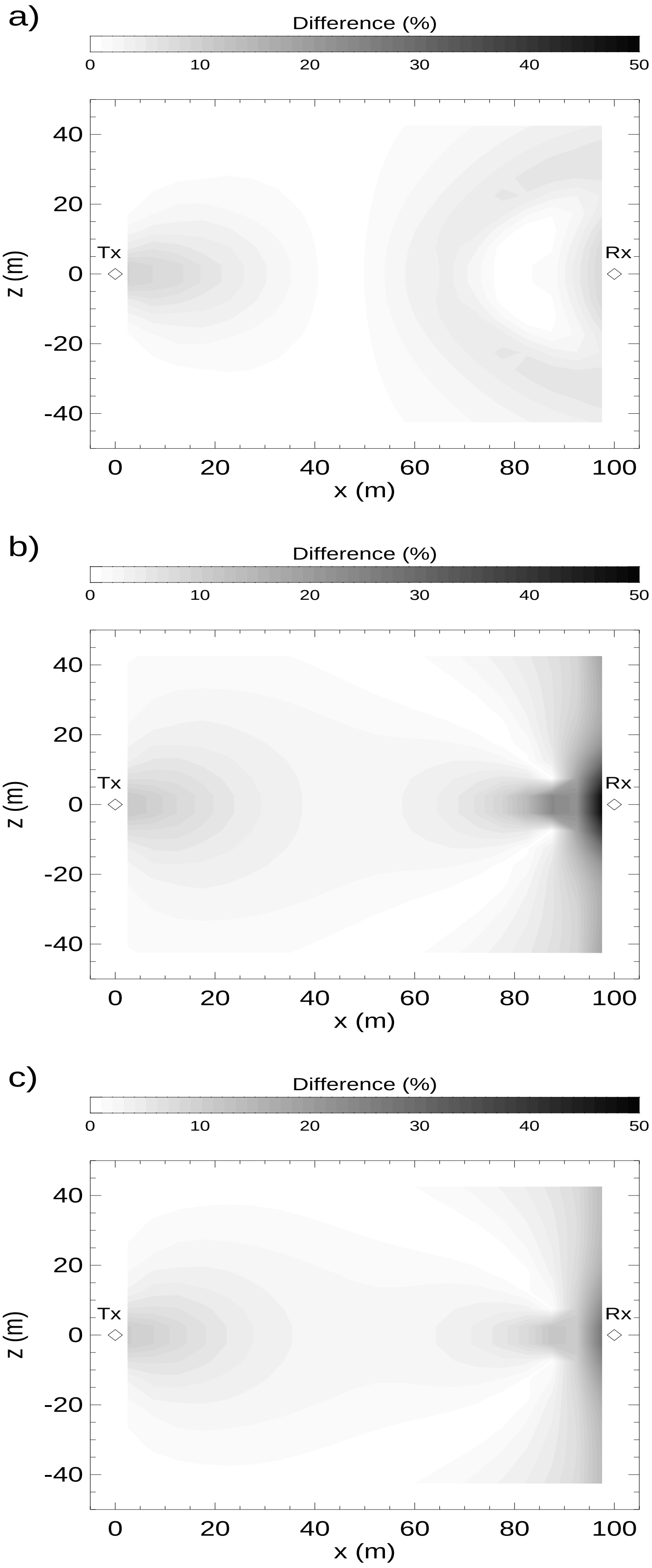

Figure 4.2: *Checks on the gradients by comparison with a perturbation method. The contour plots show the absolute differences in % between gradients computed from perturbation and backpropagation. Panel (a) shows comparisons for electric field data, panel (b) shows the corresponding comparisons for vertical voltage data and panel (c) for a combination of both data types.*

To conclude, although different ways of calculating reference values for the gradients exist, the perturbation method is preferable for verification. In comparison with the described ways of obtaining the gradient by other ways of calculating the sensitivities, the perturbation method is more different to the backpropagation method and hence provides for more independent reference values. Although relatively large differences exist locally for the shown examples involving voltage data, the gradients reveal a good agreement over most of the inspected area. The largest deviations occur close to the transmitter and receiver, where the sensitivities are large as well. This indicates that the perturbation method is probably less exact due to finite volumes associated with the sensitivities computed by cell perturbations. The later shown inversion examples will demonstrate that the accuracy of the gradients is sufficient for a successful minimum search.

4.6 Solution of the inverse problem by a NLCG scheme

So far, an efficient scheme has been constructed that allows to obtain the derivative information needed for a minimum search in the model space. Now an adequate iterative algorithm has to be found that employs the gradient information as efficiently as possible. Although the computational effort for obtaining the gradients is minimized by the migration technique, it will still dominate the inversion algorithm due to the computer–intensive time–stepping of both forward simulation and backpropagation of the fields. Therefore, iterations that do not significantly minimize the error functional need to be avoided. If the method of steepest descent is used for a minimum search and the problem to be solved is ill–conditioned, an unnecessarily high number of gradient computations is likely, because the method of steepest descent does not “remember” the direction of previous steps in the model space. The idea is to construct the search directions such that each direction is taken only once, which leads to the method of conjugate directions.

The principle that makes CG or NLCG superior to the method of steepest descent is that the search directions are constructed by conjugation of the gradient or steepest descent directions. In other words, the iterative search for a minimum of $\phi(\mathbf{m})$ takes place in the course of building a vector set of search directions that are mutually conjugate. In principle, this implies that the vectors of search directions can be transformed[4] to an orthogonal basis of the model space. It would be beyond the scope of this work to further outline the details of CG or NLCG. A more mathematical treatment is given by *Hestenes and Stiefel* [1952], *Fletcher and Reeves* [1964] and *Polyak and Ribière* [1969]. In comparison to the method of steepest descent, the conjugation of the gradients accounts for a better convergence since repeated model updating steps along the same direction do not occur.

The following algorithm flowchart for the iterative NLCG scheme is given by *Newman and Alumbaugh* [2000]. Iteration numbers are denoted by (i). The vector $\mathbf{m}$ represents a point in the model space, here it is the model space defined by the conductivity distribution. The matrices $\mathbf{M}_{(i)}$ and $\mathbf{M}_{(i+1)}$ are related to a preconditioner. The findings of *Rodi and Mackie*

---

[4] The transformation is for example represented by the matrix $\mathbf{A}$, which describes the linear system to be solved by CG. Two vectors $\mathbf{v}_1$ and $\mathbf{v}_2$ are conjugate or A–orthogonal if $\mathbf{v}_1\mathbf{A}\mathbf{v}_2 = 0$.

[2001] showed that convergence rates for the 2D MT inverse problem using NLCG can be significantly improved with preconditioning. However, the presented inversion does not yet involve preconditioning. For the purpose of a NLCG scheme without preconditioning, one can define $\mathbf{M}$ as the identity matrix.

At the first iteration the initial step (1) selects a model estimate and computes the residual $\mathbf{r}_{(i)}$, which is represented by the steepest descent vector or negative gradient of the error functional ϕ at the starting model. Note that the gradient is given by Equation (4.34), (4.35) or (4.36), depending on the data type to be inverted. The first search direction $\mathbf{u}_{(i)}$ is then set to the residual $\mathbf{r}_{(i)}$ in step (2). Step (3) represents a minimum search by a line search procedure, that is finding the value of α that minimizes the error functional for a given model and a search direction $\mathbf{u}_{(i)}$. This is an important procedure for a successful and efficient implementation of NLCG and is described in detail by *Dennis and Schnabel* [1996]. The non–linear line search makes the main difference to the linear CG method. The scheme used here was employed earlier by *Newman and Alumbaugh* [2000]. Basically, the line search algorithm finds a minimum of ϕ by using functional and derivative information at one point $\mathbf{m}_{(i)}$ in the model space and functional information at another point along the search direction $\mathbf{u}_{(i)}$. The additional computational effort required by the line search is thus mainly represented by evaluating ϕ at the second point along the search direction, because the information related to $\mathbf{m}_{(i)}$ is saved from the previous iteration. A quadratic curve is fitted through both points in order to estimate the step to the minimum. With the line search completed, the model update is performed and the new residual is evaluated at the new point $\mathbf{m}_{(i+1)}$ in the model space (step 4). Step (5) serves as a stopping criteria; if not fulfilled, a new search direction, which is conjugate to all previous ones, is determined by step (6) and (7). Both these steps perform the actual conjugation of the search directions. Basically, the procedure can be reduced to a Gram–Schmidt conjugation procedure as outlined more detailed for example by *Shewchuk* [1994] or *Meister* [1999]. With a new conjugate search direction evaluated, the algorithm loops back to the line search procedure in step (3).

```
(1) set $i = 1$, choose initial model $\mathbf{m}_{(i)}$ and compute $\mathbf{r}_{(i)} = -\nabla\phi(\mathbf{m}_{(i)})$.
(2) set $\mathbf{u}_{(i)} = \mathbf{M}_{(i)}^{-1}\mathbf{r}_{(i)}$.
(3) find $\alpha_{(i)}$ that minimizes $\phi(\mathbf{m}_{(i)} + \alpha_{(i)}\mathbf{u}_{(i)})$.
(4) set $\mathbf{m}_{(i+1)} = \mathbf{m}_{(i)} + \alpha_{(i)}\mathbf{u}_{(i)}$ and $\mathbf{r}_{(i+1)} = -\nabla\phi(\mathbf{m}_{(i+1)})$.
(5) stop when $|\mathbf{r}_{(i+1)}|$ is sufficiently small, otherwise go to step (6).
(6) set $\beta_{(i+1)} = (\mathbf{r}_{(i+1)}^T\mathbf{M}_{(i+1)}^{-1}\mathbf{r}_{(i+1)} - \mathbf{r}_{(i+1)}^T\mathbf{M}_{(i)}^{-1}\mathbf{r}_{(i)})/\mathbf{r}_{(i)}^T\mathbf{M}_{(i)}^{-1}\mathbf{r}_{(i)}$.
(7) set $\mathbf{u}_{(i+1)} = \mathbf{M}_{(i+1)}^{-1}\mathbf{r}_{(i+1)} + \beta_{(i+1)}\mathbf{u}_{(i)}$.
(8) set $i = i + 1$ and go to step (3).
```

NLCG algorithm flowchart after Newman and Alumbaugh [2000]

Fortunately, parallel implementation of the NLCG scheme is straightforward. All that is required is global communication amongst the processors to complete the dot products that occur during steps (3) and (6).

4.7 Solution stabilization

4.7.1 Regularization

In contrast to the strongly limited number of model unknowns considered in Chapter 2, the presented large–scale inversion scheme imposes a fine model parameterization, because only reconstructions that do not underparameterize the underground are considered. This may result in many more model parameters than data values and forces the 3D inverse problem to be underdetermined and thus unstable and ill–posed. In an extreme case, the least–squares best–fitting model may possess structure which is rougher than is physically possible. Reliable model estimates are still possible if the inversion is stabilized with regularization. Originally, the general procedure of regularization was introduced by *Tikhonov and Arsenin* [1977] in order to overcome mathematical difficulities in the theory of ill–posed problems. In the context of conductivity imaging, regularization can be seen as penalty for complexity, where excessively complex models are characterized by sharp conductivity variations between neighbouring model elements [*Constable et al.*, 1987; *DeGroot-Hedlin and Constable*, 1990; *Newman*, 1995; *Commer*, 1999]. Regularization thus suppresses solutions that are too rough by imposing an additional constraint on the data fit.

To implement regularization, the error functional of Equation (4.14) is augmented such that

$$\phi(\sigma) = \frac{1}{2}\sum_j \sum_i \int_0^T \delta\mathbf{d}^o(\mathbf{r}_i, t; \mathbf{s}_j) \cdot \delta\mathbf{d}^o(\mathbf{r}_i, t; \mathbf{s}_j)dt + \frac{\lambda}{2}\mathbf{m}^T\mathbf{W}^T\mathbf{W}\mathbf{m}, \tag{4.40}$$

where $\mathbf{W}$ is a regularization matrix. Following *Newman and Alumbaugh* [1997], the regularization is chosen such that $\mathbf{W}$ consists of a FD approximation to the Laplacian operator ∇^2. The tradeoff parameter λ controls the amount of smoothing to be incorporated into the model. Smoothing a solution usually takes place at the expense of an increased data misfit. Therefore, the selection of λ requires special care in order to avoid an unacceptable solution. If it is too small, the resulting model can reveal a physically unreasonable structure despite good data fits. A very smooth model due to a large λ on the other hand shows poor dependence on the data.

In an ideal case, the tradeoff parameter should be decreased gradually after each iteration in order to account for less–resolved model structures at later iterations. However, for a variation of λ during an inversion, it would be necessary to discard the previous search directions and re–initialize the algorithm starting with the steepest descent direction at the current model [*Newman and Alumbaugh*, 1997]. This would annihilate the beneftits of the NLCG scheme by reducing the convergence. Instead, a cooling approach as described by *Newman and Hoversten* [2000] can be chosen. For optimizing λ, one carries out multiple solutions to the inverse problem, starting with a large fixed value. As λ is reduced, the data error, quantified by the first term in Equation (4.40), will decrease. This process of reducing the tradeoff parameter is to be continued until the data error agrees with a target misfit based upon the assumed noise content of the data.

4.7.2 Logarithmic model parameters

In order to constrain the electrical conductivities of the model such that they are positive quantities, a logarithmic transformation as described by *Newman and Alumbaugh* [1997] is employed. It is realized by defining a new model parameter u_k at cell k using the natural logarithm,

$$u_k = \ln(m_k - \tilde{m}_k).$$

The relation allows for the incorporation of a lower bounding constraint given by $\tilde{m}_k$ such that $m_k > \tilde{m}_k$ with $\tilde{m}_k > 0$. The selection of $\tilde{m}_k$ for the cells comprising the inversion domain also represents a means of incorporating a priori model information in an inversion. The effect of this transformation on the component of the gradient, sensitive to the data errors, is to scale it by a factor of $m_k - \tilde{m}_k$. Once u_k is updated in the NLCG iteration, the parameter components that are of interest follow from the expression

$$m_k = \mathrm{e}^{u_k} + \tilde{m}_k.$$

4.8 Synthetic data inversion example

The inversion algorithm is now applied to the same model geometry and transmitter configuration as exemplified earlier in Section 2.2 (Figure 2.1). For this example, the 1 Ωm conductive block is embedded in a 10 Ωm half–space. In contrast to the sparse data covering simulated in Section 2.2, a receiver array of 99 detectors is now simulated at the surface. The spatial distribution of the sensors is shown by Figure 4.3. The SLDM code employed in Chapter 2 is used for data generation. The simulated measurements are noise–free and comprise the transmitter–parallel component of the electric field and the vertical voltage. The transmitter waveform is a shut–off in a step–wise fashion. A total number of 198 transients is inverted, where each one is sampled at 90 delay times over the time range of $t_0 = 0.5$ ms to $T = 70$ ms

No transformation of the inverted data is carried out for this example. However, the different information density at different measurement time stages of a transient is taken into account. A decreasing information density with later times results from the simple fact, that after source switch–off the spatial maximum of the induced fields moves outward from the transmitter location and thus contains the information of an increasingly larger volume. Following *Wang et al.* [1994], a weighting of $\frac{1}{t}$ is introduced into the error functional to compensate for different information density, thus Equation (4.40) changes to

$$\phi(\sigma) = \frac{1}{2}\sum_i \int_0^T \frac{1}{t}\delta\mathbf{d}^o(\mathbf{r}_i,t;\mathbf{s}_j)\cdot\delta\mathbf{d}^o(\mathbf{r}_i,t;\mathbf{s}_j)dt + \frac{\lambda}{2}\mathbf{m}^T\mathbf{W}^T\mathbf{W}\mathbf{m}. \qquad (4.41)$$

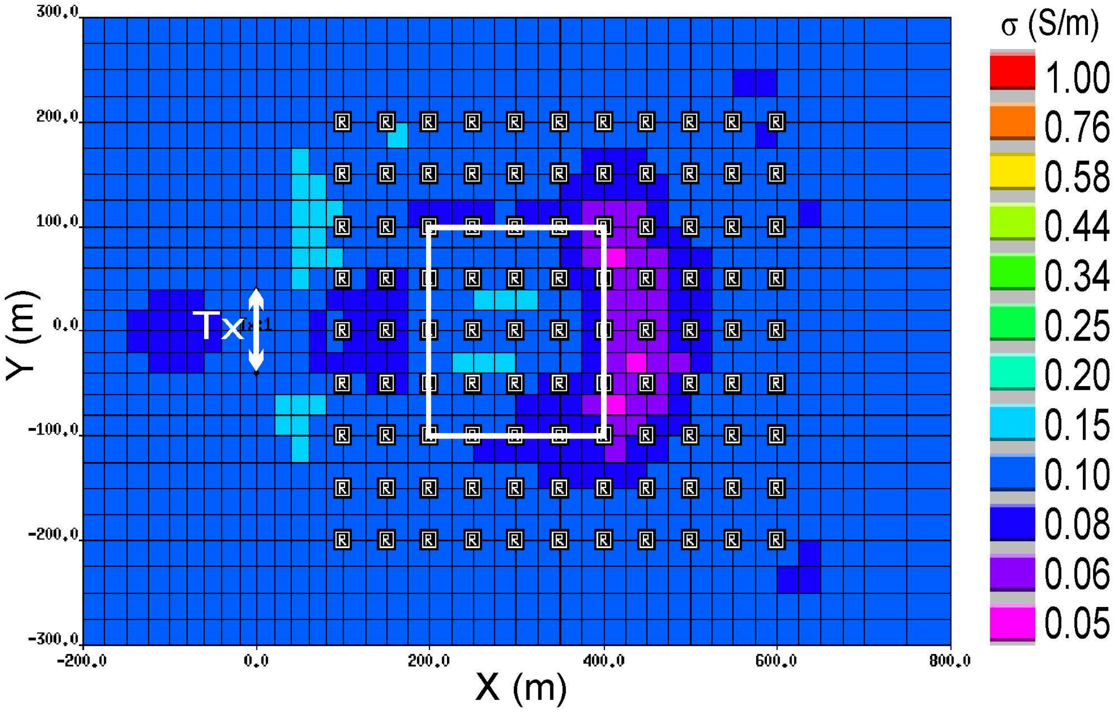

Figure 4.3: *Transmitter and receiver (R) setup of the synthetic inversion example. Also shown is the reconstructed conductivity model at the earth surface after 87 iterations. The white rectangle shows the profile of the conductive block buried in a depth of 60 m.*

Note that no summation over the external sources j is carried out, because only a single transmitter is considered. The weighting by the reciprocal time also carries over to the actual source terms $\delta\mathbf{v}^o(\mathbf{r}_i,t)$ and $\delta\mathbf{e}^o(\mathbf{r}_i,t)$ on the right–hand side of Equations (4.37) for the backpropagated fields. The weighting is equivalent to integrating over logarithmic time.

In order to more easily quantify the data misfit, each component $\delta d^o(t)$ of a data difference vector in Equation (4.41) is weighted by a value of 5 % of the corresponding original data value $d^o(t)$. It was further found to be advantageous to normalize Equation (4.41) by the sum of the integrations over the logarithmic time interval of each source–receiver pair (*Newman*, pers. comm.). Therefore, the goodness of fit of the model predictions $d^p(t)$ to the actual data values $d^o(t)$ is assessed with the following normalized error functional

$$\phi_{data} = \frac{\sum_i \int_{\ln t_0}^{\ln T} \left(d^o(t) - d^p(t)\right)^2 d(\ln t)}{\sum_i \int_{\ln t_0}^{\ln T} d(\ln t)}, \tag{4.42}$$

where the earliest measurable delay time t_0 is always above zero. This way of normalizing the error functional originates from the general assumption, that the information content of a transient is determined by the time at which the signal decays to noise level. Over fitting data in the presence of noise can thus be avoided; for example fitting the normalized data error ϕ_{data} to one implies that the observations of this example are matched to about 5 %, on average, assuming that the error is Gaussian and normally distributed. However, this type of noise assumption does not consider late time noise, which is usually non–Gaussian.

Because of the premature implementation state of the algorithm's backpropagation part, the treatment of the air–earth interface is carried out by simply extending the mesh upwards instead of using a 2D FFT for field–continuation. The inversion involves a 3D grid of size $95 \times 88 \times 64$ nodes, where 19 out of the 64 vertical nodes cover the air space. Although computation times become larger without the FFT approach for treating the air–earth interface, this way of describing the air space would also allow to incorporate topography in the modeling. The extension of the model space is from -5000 m to 5000 m in all Cartesian directions, where the air–earth interface is at $z = 0$ m. The inversion domain is limited to the whole subsurface space of the grid, thus comprising a total number of 376200 model unknowns. The starting conductivity of 10 Ωm is assigned to each grid cell. Using an initial time step of $\Delta t_0 = 10^{-6}$ s, the air layer can be approximated by a 5000 Ωm resistive half–space above the surface. It is essential that this approximation is validated before an inversion. It has been carried out by means of comparisons with analytical half–space responses.

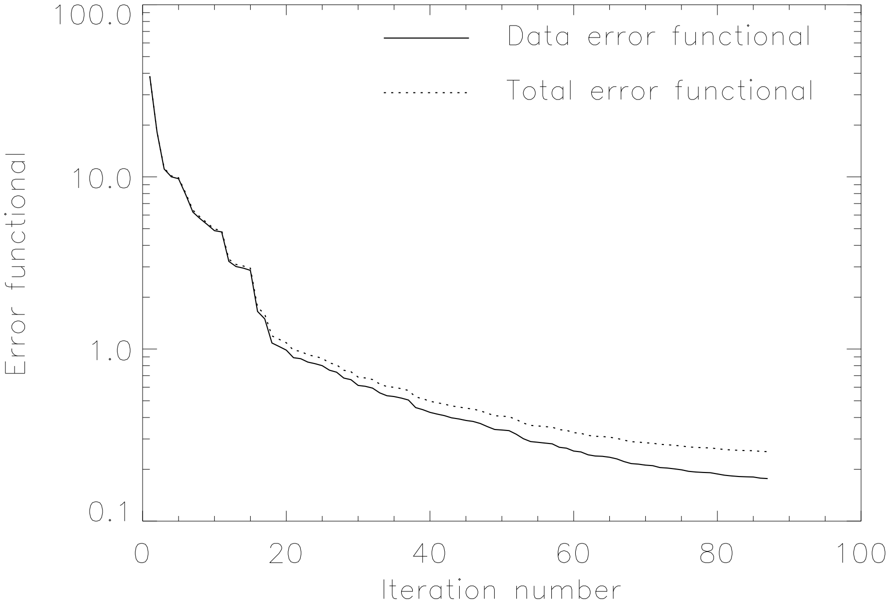

Figure 4.4: *The total normalized (dashed line) error functional is plotted against the inversion iterations. The solid curve corresponds to the data error component of the normalized error functional.*

A total number of 87 iterations was carried out using 336 processors on the supercomputer "ASCI Red"[5] operated by the Sandia National Laboratory (New Mexico, USA) (*Newman*, pers. comm.). Each iteration required approximately 5 hours of computation time. As shown by the solid line in Figure 4.4, the data part ϕ_{data} of the normalized error functional could be decreased from an initial value of 38 to 0.2. The dashed line shows the total error functional, which also includes the regularization part. During the inversion the tradeoff parameter λ (Equation 4.41) was fixed to a value of one. The data error initially drops rapidly. After approximately 20 iterations the rate of decrease in the error slows considerably.

---

[5] Accelerated Strategic Computing Initiative, see http://www.sandia.gov/ASCI/Red/ for further information about the parallel architecture.

Figure 4.5 shows the evolution of the model after 10, 30, 50 and 70 iterations. The left side shows the corresponding images in a $x-y$ section at a depth of 100 m below the surface. Note, that the white rectangle indicates the true edges of the anomaly. It can be seen that the rapid error decrease during the first 10 iterations comes along with rather small changes of the starting model. After 30 iterations, where the error functional is already below a value of one, the anomaly starts to appear in the form of a few cells with conductivity values close to one. The following iterations involve more significant changes towards the true model, whereas the error of the data fit reaches convergence. After 70 iterations both predicted data curves are in very good agreement with the synthetic data. *Wang et al.* [1994] also observed the contrasting pattern of an initially rapid data misfit decrease and an increasing model enhancement starting at later iterations. They concluded that this observation can be ascribed to the dominating response of the background medium. The size of the reconstructed conductive anomaly, exceeding the dimensions of the true block in each of the shown intermediate results, indicates the non–uniqueness of the solution.

The final result after 87 iterations is shown by Figure 4.6. Both the $x-z$ cross section (a), which bisects the point $y=0$, and the $y-z$ cross section (b) through $x=300$ clearly indicate the top of the conductive anomaly. Moreover, the reconstructed conductivity within the top part of the imaged body approaches the true value of 1 S/m. However, the images estimate the block's vertical extent to be smaller than the true case, which is shown by the white rectangles. Similarly, the horizontal cross section (c) is characterized by a concentration of cells that show the true conductivities of 1 S/m in the center of the rectangle outlined by the original block. Across the edges of the true model, the regularization drives the inversion to a smoothed out image. In Figure 4.3, which shows the inversion result at the surface ($z=0$), a resistive artefact can be observed to the right of the body. It is however spatially limited to the first grid layer.

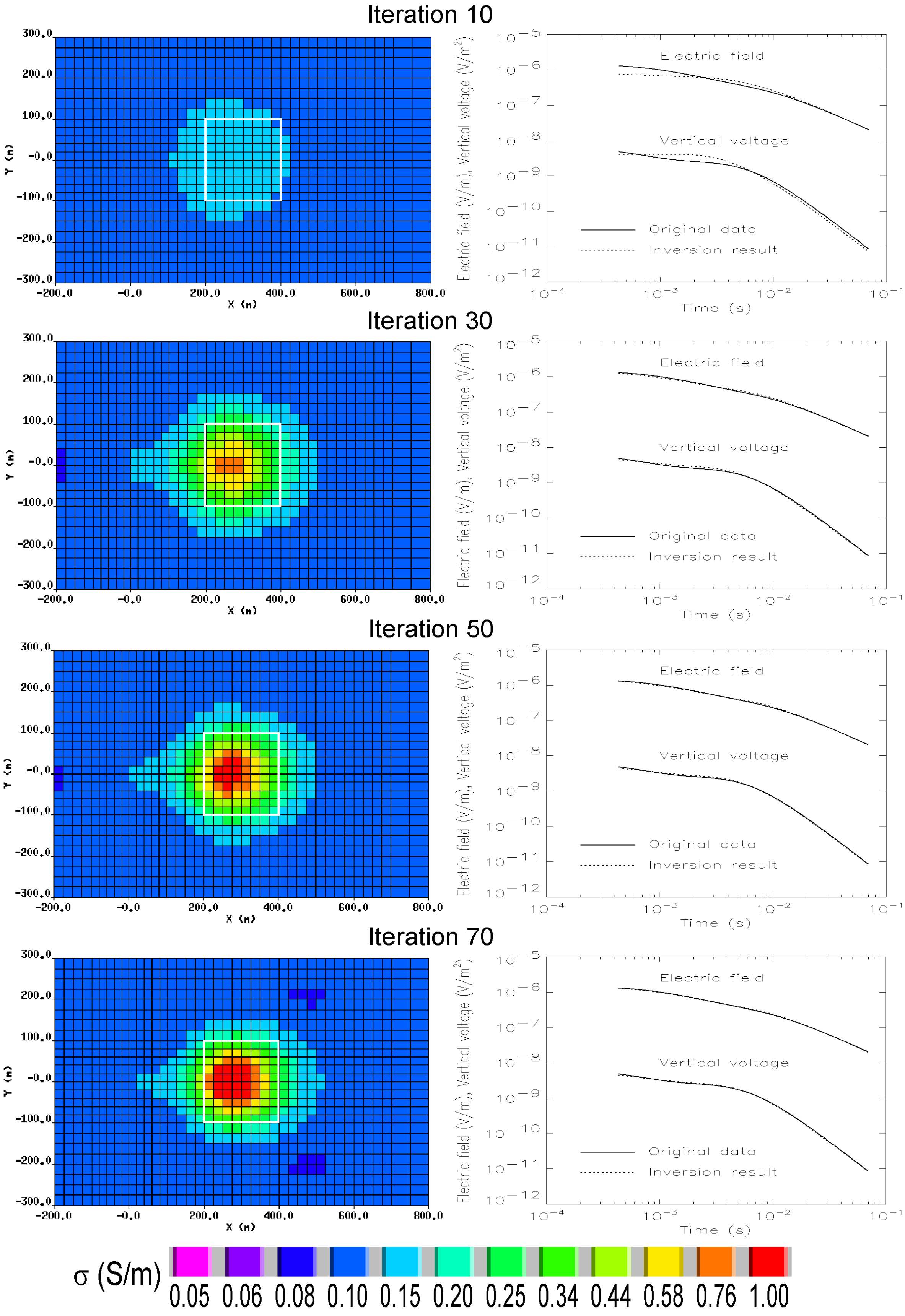

Figure 4.5: *Reconstructed models in a horizontal plane view at z=100 m (left side) and data fit for both electric field and vertical voltage data (right side) after 10, 30, 50 and 70 iterations. The shown data corresponds to the receiver position at x=500 m and y=0 m. The true location of the conductive block is indicated by the white rectangle.*

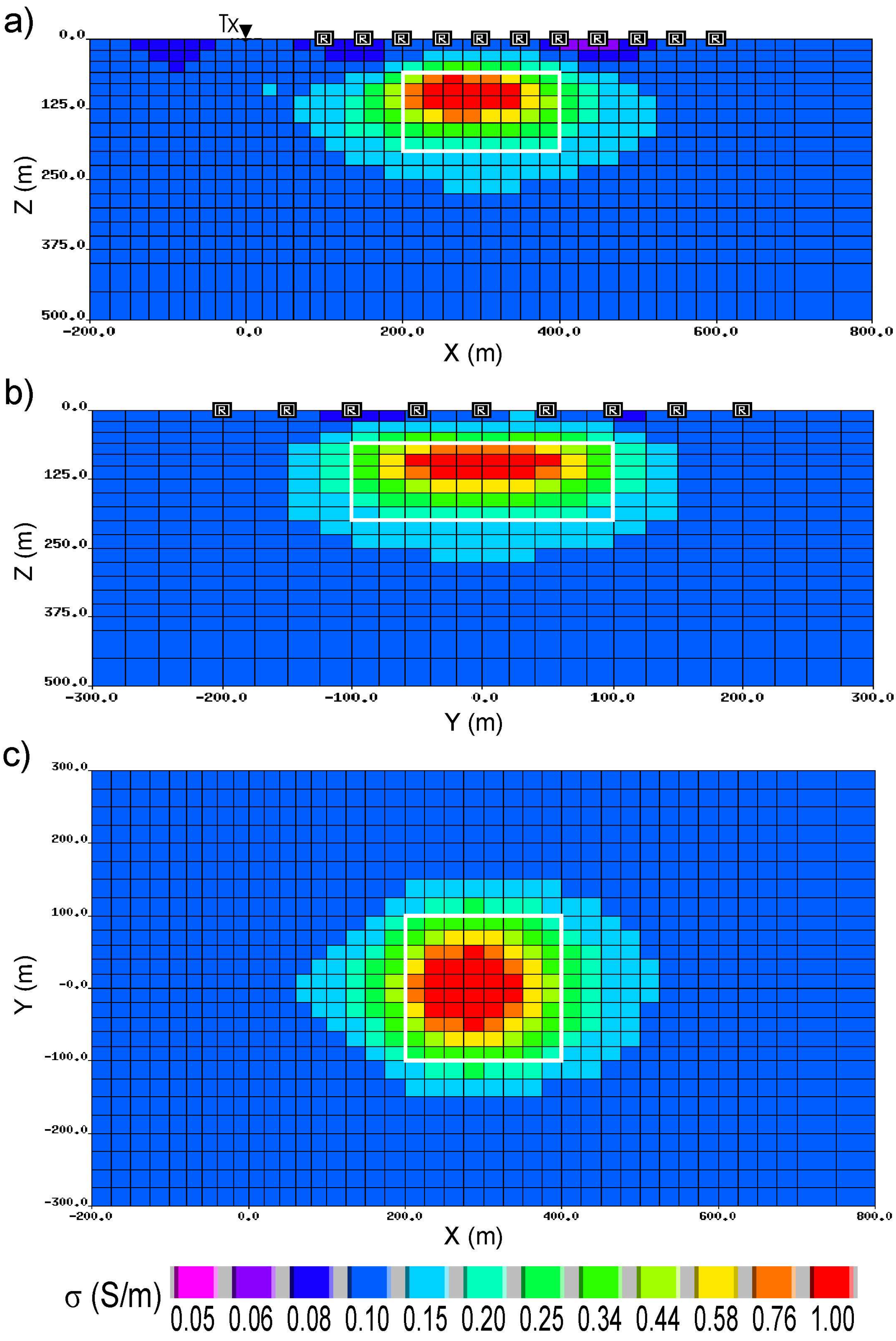

Figure 4.6: *Reconstructed model after 87 iterations. In each plot the actual location of the conductive block is indicated by a white rectangle. (a) The x–z cross section bisects the transmitter at y=0 m. (b) The y–z cross section is located at x=300 m. (c) The x–y plane of the reconstructed model at 100 m depth.*

4.9 Discussion

A theory for the inversion of 3D TEM fields arising from non–causal sources is provided. The scheme employs the concept of migration or backpropagation to efficiently evaluate the gradients of the error functional in model space. Electric field and voltage data types are treated. An attractive feature of the algorithm used for the field simulation is that the number of receivers assigned to a transmitter does not make an impact on the time needed for the gradient computation. However, the total computation time is proportional to the number of external sources generating a data set to be inverted.

A successful demonstration of the EM migration scheme is given for a 3D exploration problem. The 3D images obtained after 87 iterations are generally good, because the conductive anomaly can be reconstructed to a satisfying degree. Deviations from the true model shape result from a smoothed out image, caused by the regularization of the solution. However, a regularized solution is preferable. Without stabilizing conditions, the solution of an ill–posed inverse problem may be characterized by large oscillations and thus unrealistic models. Although smooth models are not necessarily closer to the truth than any other model which fits the data, they give at least lower bounds on the amount of structure required. Furthermore, a smooth reconstruction, obtained from a homogeneous starting model, gives an indication of the resolving power of the TEM method, because the generally poor resolution of diffusive fields does not allow to distinguish between sharp or smooth contrasts.

The use of more powerful optimization strategies are likely to be beneficial in the 3D TEM inverse problem. The gradient search method used for the iterative solution process limits the amount of forward modeling overhead, but this comes at the expense of a slow convergence. While direct Newton methods will converge in far fewer iterations, the time required per inversion iteration can be prohibitively expensive. A more promising approach would be reducing the number of iterations needed for the gradient search. Such improvements in the efficiency of the NLCG algorithm can be made by preconditioning (e.g. *Newman and Alumbaugh* [2000]; *Rodi and Mackie* [2001]). The effectiveness of a preconditioner arises from “steering” the gradient vector into a more productive search direction, which in fact is the Newton direction, thereby reducing the total number of iterations in an inversion.

CHAPTER 5

COMPARATIVE CONCLUSIONS

This work has presented two approaches for the inversion of TEM fields. The first approach presented in Chapter 2, referred to as SINV in the following, solves small–scale inversion problems. It provides solutions for as many model unknowns as typical for unconstrained least–squares inversions. The main field of application is the refinement of an a priori known model by means of an inversion. Both the Marquardt inversion and the employed SLDM forward modeling code are fully developed and well proven tools that were combined to a stable inversion for simple 3D models. Therefore, the scheme is a rather methodical than theoretical innovation in the field of EM inversion. Because of its low computational needs, SINV represents a reasonable alternative to a large–scale 3D inversion. With a parallel computing platform available, the computation times for the shown inversions ranged from only 2 to 4 hours.

The large–scale approach presented in Chapter 4 is capable of inverting for finely discretized 3D models including several hundred thousand unknowns. It is thus capable of imaging the underground without prior information needed. For brevity, the inversion method shall be referred to as TEMINV[1] in the following. The scheme uses techniques known from the migration of seismic wavefields and adapted to diffusive TEM fields. This innovative way of taking advantage of the reciprocal relationships of EM fields minimizes the computational effort for obtaining the gradient information for a minimum search. The propagation of both original and adjoint fields is accomplished by means of a parallel explicit time–stepping algorithm. For the case of real exploration problems the high computation times needed for time–stepping the fields cause the imaging scheme still to be on the verge of feasability. To become a routinely used tool for the analysis of TEM data, computation times still have to be decreased significantly. Nevertheless, the theoretical development of the gradient specifications provides a deep insight into the adjoint field formulation and its reciprocal connection

---

[1] The code name of the algorithm stands for “Transient ElectroMagnetic INVersion”.

with the original EM field.

With regard to the number of model unknowns, TEMINV allows for arbitrarily complicated models, although some limitation is also given by the regularization of the solution using smoothing constraints. Apart from the computational overhead, the method is much easier to handle in practice than SINV, because there is no requirement of defining adequate model parameters prior to an inversion. It was demonstrated by the synthetic data example in Chapter 4 that an earth model can be reconstructed from a homogeneous model. On the other hand, the limitation of SINV to invert for models with a lower degree of complexity is somewhat compensated by the capability that the scheme can be easily adapted to different inversion problems. This requires that the underground structures of interest are known in advance to such an extent that definition of the model parameters is possible. In surveys where TEM methods are employed to refine the image of a target, which appears to be the majority of cases, there usually exist different kinds of prior structural knowledge. Hence, the constraint of a low complexity becomes a significant disadvantage not until no a priori information is available and a model turns out to be too rich in structure. An example has been given by the inversion of the Kaliadem data in the case history (Section 2.3.5). Here, the model of a conductive block in a homogeneous host seems to be not suitable because of a too great simplification of the real situation.

The limited number of model unknowns is critical in a way that the solutions are highly dependent upon the model parameterization and the prior assumptions about the geology. Finding a model based on an assumed geological structure, which produces an adequate fit to the data, may tempt one to believe that features appearing in the model are necessary rather than consistent with the data. Fitting simple 3D models is therefore a delicate balance between suppressing significant structure by allowing too few degrees of freedom and introducing spurious structure by excessive or umimportant parameters. While it cannot be proven that a solution represents a global minimum, its significance can at least be substantiated by testing if convergence to the same solution is reached from different starting models. This might involve several inversion attempts, yet can be easily accomplished due to the low computational requirements of SINV. After all, it holds for both inversion methods as a matter of course that it is important to pay attention to the question of how physically realistic a solution appears.

An outstanding difference between the methods is the feasibility in the presence of insufficient field data. In the shown synthetic data inversion example of Chapter 4 the dense array of receivers over the conductive anomaly is necessary in order to provide a sufficient resolution of the large inversion domain. Here, the limitation to only one or a few profiles of measurements would strongly increase the non–uniqueness problem. Inverting field data from a sparse sensor distribution using TEMINV would only be feasible by adequately limiting the spatial extent of the inversion domain. The low–parameterized model approach of SINV addresses this problem, however at the expense of prior information to be known.

The case history in Chapter 2 represents a typical example for a TEM survey, where the sparse distribution of the measurements would prohibit the resolution of a finely parameterized model due to excessive ambiguity. Numerous other examples exist in the geophysical literature. Often only one or a few profiles crossing an a priori known target are measured in order to refine or complement the model of the structure. For example, *Taylor et al.* [1992] characterize a local groundwater system in an arid alluvial environment in Nevada (USA) by a TEM survey with an in–loop configuration. The survey was conducted in order to define the location of faults and clay rich areas. Its existence had been known by structural geologic mapping and previous drilling. Rapid lateral changes were identified by apparent resistivity pseudo–sections derived from 1D modeling results. The results show that a multi–dimensional inversion approach would be appropriate for a data analysis without the possible errors caused by the 1D interpretation. Similar to the fault model of Merapi's southern flank shown in the case history, a 2D model parameterization involving layered sections separated by faults is suggested by the known structural and stratigraphic information. In addition to the layer parameters, one could imagine the location of the faults as being variable as well.

Another example was shown by *Hördt et al.* [2000*b*], where 2D forward modeling was carried out in order to interpret data of a LOTEM survey in the Odenwald area (Germany). Among several attempts, one model includes a conductive dyke embedded in a homogeneous half–space and placed under the receiver spread to explain sign reversals in the voltage transients. The data fit achieved by such a simple 2D earth model could probably be improved to some extent by the SINV method as has been demonstrated by the inversion of the Kaliadem profile data.

A 2D inversion approach using SINV has recently been carried out by *Scholl et al.* [2002] in order to conduct a preliminary resolution study for a LOTEM survey over the Dead Sea transform fault (Jordan). Here, the method was successfully applied to invert synthetic data for a 2D fault model with a local anomaly included. The proper types of model parameters were created using a 2D resistivity model of the fault structure derived from MT interpretation results [*DESERT Group*, 2000].

Several important steps are taken in the analysis of the LOTEM field data from Merapi volcano and contribute significantly to the further development of techniques for the multi–dimensional interpretation of TEM data. First, as the author is not aware of successful 3D inversion attempts with real LOTEM field data in the geophysical literature, it shall be emphasized that for the first time a combined LOTEM data set could be inverted for a 3D model. Regarding the simple model parameterization, good data fits were achieved. Another innovation represents the inclusion of horizontal magnetic field time derivative data in the inverted data sets. It is still typical for TEM measurements to focus on the time derivative of the vertical magnetic field component, because it is easy to measure in the field.

A challenging task was given by the topographic conditions of the survey terrain, causing strong effects on some components of the combined data set. The fast forward solution provided by SLDM allowed to incorporate topography into the model without significant influence on the computation time. Modeling topography using the FD solution presented in Chapter 3 is feasible, yet requires appropriately small time steps due to the high resistivities needed to approximate air. Unfortunately, this leads to even more increased computation times when employing TEMINV. On the other hand, finding a grid discretization that causes no instabilities due to high resistivity contrasts does not require such an elaborate preparatory work as has been carried out in order to ensure convergence of SLDM.

This work has put an emphasis on the treatment of non–causal source fields arising from galvanic types of transmitters. Nevertheless, the adaption to the inversion of causal TEM fields using SINV is straightforward, because the employed SLDM code is also capable of simulating loop sources. Furthermore, the scheme could be expanded for the capacity of inverting for unknowns involving magnetic permeability. The SLDM code offers the possibility of modeling varying magnetic permeabilities, although it is not optimized for this purpose (*Hördt*, pers. comm.). Other codes capable of modeling magnetic properties could instead be combined with the SINV scheme.

Chapter 4 revealed that the treatment of causal source fields is contained in the more general non–causal case. The current implementation state of TEMINV is actually capable of recognizing the type of a source and switch to the computation of the DC part of the gradient if required. Imaging magnetic permeability distributions has not yet been realized, but the theory of the magnetic permeability gradient specifications has been given by *Newman* (pers. comm.).

As a final conclusion, it can be stated that SINV is currently more practicable for the inversion of field data, because of its modest computational requirements. However, the migration technique used by TEMINV is more state–of–the–art. Migration has become a routinely used technique for the analysis of seismic data. It has also given rise to tomography methods as for example applied in medical imaging (e.g. *Devaney* [1989]). With the development of faster computers, a stronger trend towards EM forward modeling and inversion schemes capable of treating large sets of parameters is likely to follow.

VERGLEICHENDE SCHLUSSFOLGERUNGEN

In dieser Arbeit wurden zwei Inversionsverfahren für die Inversion von TEM Daten vorgestellt. Die erste Methode, im folgenden SINV genannt, löst kleinskalige Inversionsprobleme, die sich durch eine für klassische "least–squares"–Probleme typische Modellparameteranzahl auszeichnen. Das stabile Marquardt–Verfahren wurde mit einem bewährten 3D Simulationscode zu einer 3D Inversion für einfache Modellstrukturen kombiniert. Das Verfahren stellt eher eine methodische als eine theoretische Neuerung auf dem Gebiet der EM Inversion dar. Es bietet ein Werkzeug, womit ein im Vorfeld bekanntes Modell durch Inversion verfeinert werden kann. Aufgrund des geringen Rechenzeitbedarfs stellt SINV eine Alternative zu aufwendigeren großskaligen Verfahren dar. Für die in dieser Arbeit gezeigten Inversionen genügten dank der Verwendung eines Parallelrechners Rechenzeiten von 2 bis 4 Stunden.

Das in Kapitel 4 vorgestellte Verfahren für großskalige Probleme, im folgenden mit TEMINV bezeichnet, ist für Modellansätze geeignet, die mehrere 100000 Unbekannte beinhalten. Es ist dazu geeignet, ohne Einbezug von Vorinformationen ein Erdmodell zu erstellen. Hier werden Techniken, die von der Migration seismischer Wellenfelder bekannt sind, auf diffusive EM Felder angewandt, was die Lösung der adjungierten Maxwell Gleichungen beinhaltet. Ähnlich wie bei seismischer Migration, lassen sich die Gradienten des Fehlerfunktionals der Datenanpasssung effizient durch Korrelation der Primärfelder mit den adjungierten Feldern errechnen. Die Berechnung beider Felder durch ein explizites Finite–Differenzen Zeitschrittverfahren ist sehr zeitaufwendig. Für einen routinemäßigen Einsatz müssen daher die durch das Verfahren beanspruchten Rechenzeiten vermindert werden. Dennoch bietet die hier vorgestellte Theorie des Verfahrens einen tiefen Einblick in den Formalismus der Adjungierten Feldgleichungen, sowie ihre Verknüpfung mit den Primärfeldern über das Reziprozitätsgesetz.

Im Hinblick auf die Zahl der Unbekannten erlaubt TEMINV hochkomplexe Modelle, obwohl eine gewisse Einschränkung durch die Glättungsbedingung vorhanden ist. Abgesehen vom Rechenzeitbedarf ist TEMINV insofern benutzerfreundlicher als SINV, da die Modellparameter nicht auf das Inversionsproblem abgestimmt werden müssen. In Kapitel 4 wurde demonstriert, dass eine Anomalie von einem homogenen Startmodell ausgehend rekonstruiert werden kann. Die für SINV geltende Modellbeschränkung wird teilweise dadurch kompensiert, dass die Methode leicht an ein Inversionsproblem angepasst werden kann. Das erfordert allerdings ausreichende Vorinformationen, um eine geeignete Modellparametrisierung zu finden. Ich bin davon überzeugt, dass das kein wesentlicher Nachteil ist, wenn eine TEM Messung über einer bereits bekannten Struktur mit dem Ziel der Modellverbesserung durchgeführt wird. Nur für den Fall ohne Vorinformationen und wenn sich die Leitfähigkeitsverteilung des Untergrundes als zu komplex herausstellt, ist das Verfahren ungeeignet. Ein Beispiel zeigte die Inversion der Kaliadem Daten. Hier scheint das Modell eines leitfähigen Blocks in einem homogenen Halbraum eine zu starke Vereinfachung der realen Situation zu sein.

Die eingeschränkte Parameteranzahl ist insofern kritisch, dass eine Lösung stark von der Art der Modellparametrisierung und den damit zusammenhängenden Annahmen über die zugrundeliegende Geologie abhängt. Eine geeignete Datenanpassung kann zu einer Überbewertung von Modellstrukturen, die auf Vorinformationen basieren, verleiten. Hier muß stets beachtet werden, wieviel Struktur für eine Datenanpassung tatsächlich vonnöten ist. Die Definition der Art der Unbekannten bedarf daher besonderer Aufmerksamkeit. Einerseits unterdrückt eine zu geringe Zahl von Freiheitsgraden signifikante Strukturen, im anderen Falle enstehen unechte Modellstrukturen durch unwichtige Parameter. Es kann zwar nicht bewiesen werden, ob eine Lösung ein globales Minimum darstellt, aber dennoch kann zumindest ihre Aussagekraft untermauert werden. Das geschieht durch Testen, ob verschiedene Startmodelle zu dieser Lösung führen. Mehrere Inversionsansätze sind dazu erforderlich, was aber aufgrund des geringen Rechenzeitbedarfs von SINV kein Hindernis darstellt. Vor allem soll nicht unerwähnt bleiben, dass es für beide Inversionsverfahren selbstverständlich wichtig ist, zu überprüfen wie realistisch eine Lösung generell erscheint.

Ein wesentlicher Unterschied zwischen beiden Verfahren ist ihre Einsatzmöglichkeit bei einer geringen Zahl von Messdaten. Für die Inversion der synthetischen Daten in Kapitel 4 war das dichte Netz von Empfängern notwendig, um eine ausreichende Auflösung der Anomalie zu gewährleisten. Hier würde die Beschränkung auf ein oder wenige Profile das Problem der Nichteindeutigkeit der Lösung stark erhöhen. Abhilfe würde hier lediglich eine entsprechende Verkleinerung des durch die Inversion veränderbaren Modellraums schaffen. Der Ansatz mit wenigen aber flexiblen Modellparametern macht SINV in diesem Punkt geeigneter, allerdings erfordert er Vorinformationen.

Das Fallbeispiel in Kapitel 2 präsentiert ein typisches Beispiel einer TEM Messung mit einer geringen Anzahl von Stationen. Die Datenabdeckung würde hier wegen des Problems der Nichteindeutigkeit die Auflösung eines durch sehr viele Unbekannte diskretisierten Modells verbieten. Eine Vielzahl weiterer Beispiele findet sich in der geophysikalischen Literatur. Oft werden nur wenige Profile über einer bereits bekannten Struktur gemessen, um eine Modellverfeinerung zu erreichen. Ein Beispiel findet sich bei *Taylor et al.* [1992]. Hier dienten TEM Messungen mit einer Central–Loop Konfiguration der Grundwassererkundung in einem durch trockene vulkanische Ablagerungen charakterisierten Gebiet in Nevada (USA). Die Messung hatte das Ziel der Lokalisierung von Verwerfungen und lehmreichen Strukturen, worüber Vorinformationen durch geologische Kartierungen und Bohrungen existierten. Starke laterale Widerstandsänderungen konnten durch Pseudosektionen von 1D Modellergebnissen ausgemacht werden. Die Ergebnisse zeigen, dass sich eine mehrdimensionale Inversion für eine Datenanalyse anbieten würde, um Fehler durch 1D Annahmen zu vermeiden. Ähnlich zu dem in Abschnitt 2.3.5 gezeigten Verwerfungsmodell der Südflanke des Merapi scheint ein 2D Modell mit durch Verwerfungen getrennten Schichtfolgen naheliegend. Zusätzlich zu den Schichtparametern bieten sich als weitere Freiheitsgrade die Positionen der Verwerfungen an.

Ein weiteres Beispiel ergibt sich bei der von *Hördt et al.* [2000*b*] beschriebenen Datenauswertung einer LOTEM Messung im Odenwald (Süddeutschland). Unter mehreren 2D Modellansätzen wurde ein leitfähiger Block in einem homogenen Halbraum modelliert, um Vorzeichenwechsel in der zeitlichen Ableitung der magnetischen Vertikalfelder zu erklären. Ähnlich wie es bei der Inversion der Daten des Kaliadem Profils demonstriert wurde, bietet sich hier SINV für eine eventuelle Modellverbesserung im Sinne einer besseren Datenanpassung an.

Die Methode SINV wurde bereits von *Scholl et al.* [2002] für eine 2D Inversion eingesetzt.

Die Rechnungen dienten einer Auflösungsstudie für LOTEM Messungen über einem Spaltensystem am Toten Meer (Jordanien) im Rahmen des DESERT Projekts [*DESERT Group*, 2000]. Dabei wurden synthetische Daten eines geschichteten 2D Modells mit Verwerfung und zusätzlicher Anomalie erfolgreich invertiert. Die entsprechenden Modellparameter wurden anhand von Vorinformationen durch 2D MT Modellergebnisse erzeugt.

Mehrere wichtige Schritte zur Weiterentwicklung mehrdimensionaler Interpretationsverfahren für TEM Daten werden im Rahmen des Fallbeispiels in Kapitel 2 ausgeführt. Zunächst soll betont werden, dass zum erstem Mal eine erfolgreiche 3D Inversion von LOTEM Daten durchgeführt wurde. Unter Berücksichtigung der eingeschränkten Modellparametrisierung konnte eine relativ gute Datenanpassung erreicht werden. Eine weitere Neuerung stellt das Einbeziehen der Daten von horizontalen Magnetfeldern dar. Typischerweise liegt bei TEM Messungen ein Schwerpunkt auf der Aufzeichnung vertikaler Magnetfelder bzw. ihrer zeitlichen Ableitung, da diese im Feld einfacher zu messen sind.

Eine Herausforderung bestand aus der Berücksichtigung der topographischen Gegebenheiten des Messgebiets am Merapi. Einige Daten zeigten dadurch starke Effekte. Der benutzte SLDM Simulationscode erlaubt die Modellierung von Topographie ohne bedeutenden zusätzlichen Rechenaufwand. Die in Kapitel 3 vorgestellte FD Simulationsmethode erlaubt ebenfalls die Modellierung von Geländestrukturen. Allerdings erfordert die Approximation des Luftraums mit einem entsprechend hohen Widerstand sehr kleine Zeitschritte. Das würde zur weiteren Steigerung des ohnehin großen Rechenzeitbedarfs von TEMINV für eine Dateninversion beitragen. Ein Vorteil gegenüber SINV ist jedoch, dass sich das explizite Zeitschrittverfahren zur Feldsimulation bei Vorhandensein großer Leitfähigkeitskontraste stabiler verhält. Die im Vorfeld einer Inversion mit SINV durchgeführten Stabilitätstests für die Gitterdiskretisierung, wie im Fallbeispiel gezeigt, erübrigen sich für das Verfahren TEMINV.

Diese Arbeit behandelt schwerpunktmäßig die durch galvanisch gekoppelte Quellen erzeugten akausalen EM Felder. Die Methode SINV kann ohne weiteres auf die Inversion kausaler Felder angepasst werden, da der SLDM Code auch induktiv gekoppelte Sender simulieren kann. Darüberhinaus kann die Methode für die Auflösung von Strukturen mit variablen magnetischen Permeabilitäten erweitert werden. Der SLDM Code unterstützt die Modellierung von Permeabilitätsvariationen, ist dafür allerdings nicht optimiert (*Hördt*, pers. Komm.). Zu diesem Zweck könnten jedoch andere Modellierungsprogramme mit dieser Fähigkeit herangezogen werden.

Im Kapitel 4 wurde gezeigt, dass die Behandlung kausaler EM Felder bei der Gradientenberechnung im allgemeineren akausalen Fall enthalten ist. Die gegenwärtige Programmversion von TEMINV erlaubt die automatische Erkennung des Sendertyps und berechnet gegebenenfalls die durch die Gleichstromkomponente verursachten Anteile der Gradienten. Die Berücksichtigung von Permeabilitätsvariationen in der Inversion wurde noch nicht realisiert. Die dafür notwendige Theorie mit einer Spezifikation der entsprechenden Gradienten zeigen *Newman und Commer* [2003].

Abschließend ist zu bemerken, dass sich das Verfahren SINV gegenwärtig durch größere Praktikabilität auszeichnet, was im geringen Rechenaufwand begründet ist. Allerdings stellt TEMINV mit dem EM Migrationsverfahren die modernere Methode dar. Migration ist eine routinemässig eingesetzte Technik zur Analyse seismischer Daten. Ebenso basieren darauf tomographische Techniken, die z.B. in der Medizin angewandt werden (siehe z.B. *Devaney* [1989]). Mit der Entwicklung leistungsfähigerer Computer wird sich der Trend weiter in Richtung von großskaligen Simulationen und Inversionsverfahren bewegen.

APPENDIX A

ADDITIONAL NOTES AND DERIVATIONS

A.1 Stability condition for the DuFort–Frankel method

The application of the DuFort–Frankel method in the time–stepping algorithm is carried out by introducing a hyperbolic displacement term into the parabolic diffusion equation. This term (see Equation 3.1b) is artificial, because it is applied to the quasistatic case, where displacement currents can be neglected. Its magnitude can be much larger than the real displacement current in a medium without polarization effects. For example, consider a minimum grid spacing of 25 m, a time step of 1 μs and the magnetic permeability in vacuum. According to Equation (3.8), a value of $\gamma \approx 3.8 \cdot 10^{-9}$ results which is 430 times larger than the real permittivity in vacuum. In fact, this does not matter as long as the velocity of the fictitious wavefield is kept slower than the diffusive fields simulated in the FD grid. This is achieved by restricting the size of the time steps such that the domination of diffusion is retained. Following the analysis given by *Oristaglio and Hohmann* [1984] and *Adhidjaja and Hohmann* [1989], it is demonstrated here that the DuFort–Frankel method is unconditionally stable. Furthermore, a derivation of Equation (3.7) is given.

Because a wavefield is considered, one starts with the wave equation for the electric field in a source–free whole–space. For simplicity, its scalar form is given, approximating the situation in a FD grid along one of the Cartesian coordinates,

$$\nabla^2 e - \mu_0 \varepsilon_0 \frac{\partial^2 e}{\partial t^2} - \mu_0 \sigma \frac{\partial e}{\partial t} = 0, \tag{A.1}$$

where permittivity and permeability of vacuum are assumed. This equation is easily obtained from Equations (3.1). The wave equation is satisfied by the general Green function in a whole–space given by *Ward and Hohmann* [1988],

$$\mathcal{G}(r,t) = \frac{1}{4\pi r}\left\{ \mathrm{e}^{-a\frac{r}{c}}\delta(t-\frac{r}{c}) + \frac{a\frac{r}{c}\mathrm{e}^{-at}}{\sqrt{t^2-\frac{r^2}{c^2}}} I_1\left(a\sqrt{t^2-\frac{r^2}{c^2}}\right) u(t-\frac{r}{c})\right\}, \tag{A.2}$$

where $a = \frac{\sigma}{2\varepsilon_0}$, δ is a delta function, $c^2 = \frac{1}{\varepsilon_0\mu_0}$, $I_1(z)$ is the modified Bessel function of the first kind, and $u(t-\frac{r}{c})$ is the Heavyside step function. In the case of low frequencies or late times, where displacement currents can be neglected, Equation (A.1) changes to

$$\nabla^2 e - \mu_0\sigma\frac{\partial e}{\partial t} = 0. \tag{A.3}$$

The corresponding Green function associated with the diffusion equation is also given by *Ward and Hohmann* [1988],

$$\mathcal{G}(r,t) = \frac{\sqrt{\mu_0\sigma}}{8\pi^{\frac{3}{2}}t^{\frac{3}{2}}}\mathrm{e}^{\frac{-\mu_0\sigma r^2}{4t}}u(t). \tag{A.4}$$

From setting the derivative of (A.4) with respect to time to zero, it follows that the maximum of the signal propagated by $\mathcal{G}$ at a given distance r occurs at the time

$$t = \frac{\mu_0\sigma r^2}{6}.$$

The time interval for diffusion on a 3D numerical grid with a spacing Δ is thus given by

$$\Delta t = \frac{\mu_0\sigma\Delta^2}{6}, \tag{A.5}$$

which is called the grid diffusion time. Now consider the time–staggering of the electric field $e = e^n(i,j,k)$ at a time t_n and a grid cell (i,j,k) of a uniform mesh with the grid spacing Δ. To realize Equation (A.3) using a classical Euler scheme involves approximating the time derivative by the simple forward difference

$$\left(\frac{\partial e}{\partial t}\right)^n \approx \frac{e^{n+1}-e^n}{\Delta t}.$$

It can be shown that the maximum time step Δt of the Euler scheme is given by the grid diffusion time [*Oristaglio and Hohmann*, 1984]. This, however, is too restrictive because it does not allow to address the smoothing of fields due to the fast decay of high frequency modes in a field. For example, if an earth model includes low conductivities for the host rock of a conductive target, the time step has to be set accordingly without being able to account for the larger time steps allowed by the conductive target at later times.

The DuFort–Frankel method represents an improvement, because it allows to take into account the slowing down of the diffusion rate at larger distances from the source by gradually increasing the time step with progressing time. To relate the diffusion rate to the time of the advancing field, the case when (A.2) and (A.4) agree asymptotically is first considered, given by *Oristaglio and Hohmann* [1984],

$$\sqrt{t^2-\frac{r^2}{c^2}} \gg \frac{2\varepsilon_0}{\sigma},$$

or

$$t \gg \frac{2\varepsilon_0}{\sigma}, \tag{A.6}$$

which is always satisfied in the TEM case.

The actual implementation of the DuFort–Frankel method in the time–stepping scheme is in principle realized by using central differences instead of forward differences, specifically

$$e^n = \frac{e^{n+1} + e^{n-1}}{2}$$

for the electric field at t_n and

$$\left(\frac{\partial e}{\partial t}\right)^n = \frac{e^{n+1} - e^{n-1}}{2\Delta t},$$

for its time derivative. The usage of central differences for the time–stepping scheme leads to the leap–frog method. Note that in Section 3.1.2 the leap–frog scheme is realized by using intermediate time instances for sampling the magnetic fields between the integer instances of electric fields. Now the separate terms of the diffusion Equation (A.3) are discretized to

$$\begin{aligned} \nabla^2 e = & \Big[e^n(i+1,j,k) + e^n(i-1,j,k) + e^n(i,j+1,k) + e^n(i,j-1,k) \\ & + e^n(i,j,k+1) + e^n(i,j,k-1) - 6\frac{e^{n+1}+e^{n-1}}{2} \Big] \frac{1}{\Delta^2}, \\ \mu_0\sigma\frac{\partial e}{\partial t} = & \, \mu_0\sigma\frac{e^{n+1} - e^{n-1}}{2\Delta t}, \end{aligned}$$

where $e = e^n(i,j,k)$ and $e^{n\pm1} = e^{n\pm1}(i,j,k)$. Using the Taylor series expansion for the time coordinates

$$e^{n\pm1} \approx e \pm \Delta t\frac{\partial e}{\partial t} + \frac{\Delta t^2}{2}\frac{\partial^2 e}{\partial t^2},$$

and a similar one for space coordinates, for example

$$e(i\pm1,j,k) \approx e \pm \Delta\frac{\partial e}{\partial x} + \frac{\Delta^2}{2}\frac{\partial^2 e}{\partial x^2},$$

yields [*Adhidjaja and Hohmann*, 1989]

$$\nabla^2 e - 3\frac{\Delta t^2}{\Delta^2}\frac{\partial^2 e}{\partial t^2} - \mu_0\sigma\frac{\partial e}{\partial t} = 0. \tag{A.7}$$

This equation is hyperbolic and its stability is governed by the Courant–Friedrichs–Levy (CFL) criterion for the wave velocity c (e.g. *Richtmeyr and Morton* [1967]),

$$c \leq \frac{\Delta}{\sqrt{3}\Delta t}.$$

Equation (A.7) approximates a wave equation in which the wave speed is exactly $\frac{\Delta}{\sqrt{3}\Delta t}$, thereby automatically satisfying the CFL condition. This is referred to as the unconditional stability of the DuFort–Frankel method. Changing the time step or the grid spacing translates into approximating a field with a different wave velocity. Therefore, care must be taken to avoid that the wave–like solutions dominate the diffusive behaviour by limiting the time step.

A limiting condition can now be found by rearranging the CFL criterion to

$$\gamma \geq \frac{3}{\mu_0}\frac{\Delta t^2}{\Delta^2}, \tag{A.8}$$

where the permittivity ε_0 was replaced by the artificial γ. Substituting (A.8) into (A.6), one obtains the condition which insures both the CFL criterion as well as the domination of diffusion of the time–staggered fields,

$$\Delta t \ll \sqrt{\frac{\mu_0 \sigma t}{6}}\Delta.$$

For the case of a non–homogeneous model and a non–uniform mesh one has to take into account the minimum values for magnetic permeability, conductivity and grid spacing.

A.2 Numerical solution of the 3D Poisson problem

The numerical procedure of solving for the 3D potential distribution φ originating from a current distribution $\mathbf{j}^s$ inside or at the surface of an arbitrary conductivity distribution σ is presented. This 3D Poisson problem is given by

$$\nabla \cdot (\sigma \nabla \varphi) = -\nabla \cdot \mathbf{j}^s.$$

The boundary conditions of this problem are given by assuming a vanishing total potential at the outer mesh boundaries (Dirichlet condition). In the case of a half–space, Neumann boundary conditions are applied at the air–earth interface by setting

$$\sigma \frac{\partial \varphi}{\partial z} = j_z = 0.$$

Consider a FD grid with a number of $I \times J \times K$ grid cells in the x, y and z direction, respectively. Illustrated in Figure A.1, for a given node (i, j, k) the discrete approximation of the left–hand side of the Poisson equation leads to a seven–point scheme, because the center cell and its six direct neighbours along the main coordinate axes are involved. The potential $\varphi(i, j, k)$ is constant over the cell. The multiplication of its spatial derivative with the cell conductivity requires the incorporation of directional conductivities, which are obtained by the averaging scheme described in Section 3.1.1. For reasons of simplification, the directional conductivities are indexed by integer numbers, for example $\sigma_x(i+\frac{1}{2}, j, k) = \sigma_x(i, j, k)$ and $\sigma_x(i-\frac{1}{2}, j, k) = \sigma_x(i-1, j, k)$.

Discretizing the left–hand side of the Poisson equation, one gets

$$\begin{aligned}
&\nabla \cdot (\sigma \nabla \varphi) = \\
&\left[\sigma_x(i,j,k)\frac{\varphi(i+1,j,k)-\varphi(i,j,k)}{\Delta x_i} - \sigma_x(i-1,j,k)\frac{\varphi(i,j,k)-\varphi(i-1,j,k)}{\Delta x_{i-1}}\right]\frac{1}{\overline{\overline{\Delta x}}_i} \\
+&\left[\sigma_y(i,j,k)\frac{\varphi(i,j+1,k)-\varphi(i,j,k)}{\Delta y_j} - \sigma_y(i,j-1,k)\frac{\varphi(i,j,k)-\varphi(i,j-1,k)}{\Delta y_{j-1}}\right]\frac{1}{\overline{\overline{\Delta y}}_j} \\
+&\left[\sigma_z(i,j,k)\frac{\varphi(i,j,k+1)-\varphi(i,j,k)}{\Delta z_k} - \sigma_z(i,j,k-1)\frac{\varphi(i,j,k)-\varphi(i,j,k-1)}{\Delta z_{k-1}}\right]\frac{1}{\overline{\overline{\Delta z}}_k},
\end{aligned}$$

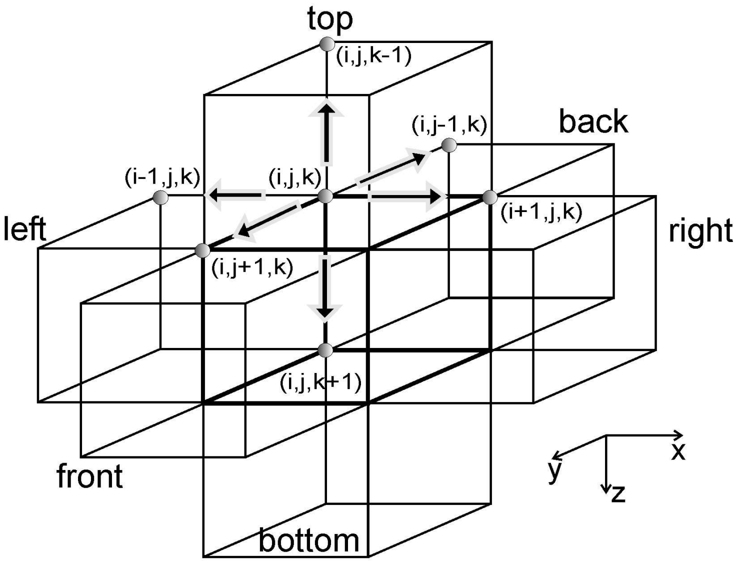

Figure A.1: *Discretization of the Poisson operator by a seven–point scheme for a grid node (i,j,k) of the 3D mesh. A potential is assigned to each of the seven nodes. The arrows illustrate the discretization of the right–hand side of the Poisson equation, involving the current density components of the six surrounding edges.*

which can be rearranged to

$$
\begin{aligned}
&\nabla\cdot(\sigma\nabla\varphi) = \\
&\quad \frac{\sigma_x(i,j,k)}{\Delta x_i\overline{\Delta x}_i}\varphi(i+1,j,k)+\frac{\sigma_x(i-1,j,k)}{\Delta x_{i-1}\overline{\Delta x}_i}\varphi(i-1,j,k)+\frac{\sigma_y(i,j,k)}{\Delta y_j\overline{\Delta y}_j}\varphi(i,j+1,k)\\
&+\frac{\sigma_y(i,j-1,k)}{\Delta y_{j-1}\overline{\Delta y}_j}\varphi(i,j-1,k)+\frac{\sigma_z(i,j,k)}{\Delta z_k\overline{\Delta z}_k}\varphi(i,j,k+1)+\frac{\sigma_z(i,j,k-1)}{\Delta z_{k-1}\overline{\Delta z}_k}\varphi(i,j,k-1)\\
&-\left[\frac{\sigma_x(i,j,k)}{\Delta x_i\overline{\Delta x}_i}+\frac{\sigma_x(i-1,j,k)}{\Delta x_{i-1}\overline{\Delta x}_i}+\frac{\sigma_y(i,j,k)}{\Delta y_j\overline{\Delta y}_j}+\frac{\sigma_y(i,j-1,k)}{\Delta y_{j-1}\overline{\Delta y}_j}+\frac{\sigma_z(i,j,k)}{\Delta z_k\overline{\Delta z}_k}+\frac{\sigma_z(i,j,k-1)}{\Delta z_{k-1}\overline{\Delta z}_k}\right]\\
&\cdot\varphi(i,j,k).
\end{aligned}
$$

In the case of a half–space, the terms involving $\sigma_z(i,j,k-1)$ vanish at the air–earth interface. Now the discrete form of the left–hand side is rewritten by assigning coefficients to each of the seven cell potentials, keeping the same order of the terms,

$$
\begin{aligned}
\nabla\cdot(\sigma\nabla\varphi) =& c_{right}\varphi(i+1,j,k)+c_{left}\varphi(i-1,j,k)+c_{front}\varphi(i,j+1,k)\\
&+c_{back}\varphi(i,j-1,k)+c_{bottom}\varphi(i,j,k+1)+c_{top}\varphi(i,j,k-1)\\
&-[c_{right}+c_{left}+c_{front}+c_{back}+c_{bottom}+c_{top}]\cdot\varphi(i,j,k),
\end{aligned}
\tag{A.9}
$$

where the coefficients are named according to the positions of the corresponding cell potentials in Figure A.1. The difference representation in Equation (A.9) is obtained for each node of the 3D mesh, once the appropriate coefficients are computed using the proper boundary conditions. Together with the right–hand side of the Poisson equation, the sets of difference equations for each node are then assembled into a matrix form

$$\mathbf{C}\varphi = \mathbf{b}, \tag{A.10}$$

where φ now denotes the unknown solution vector of the total potential at all nodes. Thus, the size of φ is given by the total number of cells IJK. The matrix **C** has the size $IJK \times IJK$ and is called the capacitance matrix [*Dey and Morrison*, 1979]. It is a function only of the geometry and the physical property distribution in the grid. The right–hand side vector **b** in (A.10) is given by the divergence of the external source current density $\mathbf{j}^s$. Its FD discretization is straightforward as shown by Equation (3.12).

According to *Dey and Morrison* [1979], **C** has the properties that it is symmetric, diagonally dominant, sparse and banded with only six nonzero codiagonals. Furthermore, it is positive definite. The system of equations given by (A.10) can thus be solved easily by a CG solver. The parallel iterative library AZTEC [*Hutchinson et al.*, 1995] has been employed for the solution. It provides for preconditioning and efficient storage schemes in order to address the sparse nature of the capacitance matrix.

A.3 Reciprocity relationship for electric and magnetic fields

Integration of Equation (4.12b) involving the time t yields

$$\int_t^{t'} \mathcal{G}_{12}^{+}(\mathbf{r}',t'|\mathbf{r},t)dt = -\mu(\mathbf{r}) \int_t^{t'} \frac{\partial}{\partial t} \tilde{\mathcal{G}}_{21}(\mathbf{r},t|\mathbf{r}',t')dt$$

Due to the time integration, the left–hand side of this equation can be identified as the electric field step response arising from a magnetic dipole source. Carrying out the integration of the right–hand side, it can be written

$$\begin{aligned} {}^{step}\mathcal{G}_{12}^{+}(\mathbf{r}',t'|\mathbf{r},t) &= -\mu(\mathbf{r})\,\tilde{\mathcal{G}}_{21}(\mathbf{r},t|\mathbf{r}',t')|_t^{t'} \\ &= -\mu(\mathbf{r})\,\tilde{\mathcal{G}}_{21}(\mathbf{r},t'|\mathbf{r}',t') + \mu(\mathbf{r})\,\tilde{\mathcal{G}}_{21}(\mathbf{r},t|\mathbf{r}',t'), \end{aligned}$$

where the first term on the right–hand side vanishes due to the causality of the Green dyadic, given by Equation (4.5). The remaining term leads to the relationship

$${}^{step}\mathcal{G}_{12}^{+}(\mathbf{r}',t'|\mathbf{r},t) = \mu(\mathbf{r})\,\tilde{\mathcal{G}}_{21}(\mathbf{r},t|\mathbf{r}',t'),$$

given before by Equation (4.13a). The same steps are carried out in order to obtain Equation (4.13b) from (4.12c). Here, the time integration needs to be done with respect to t' instead of t, leading to the different sign in (4.13b).

A.4 Integration order of the gradient

The reversal of the order of time integration in Equation (4.21) is clarified. If Equation (4.20) is rewritten such that it is emphasized that the integration variables dt and dt' belong to the outer and inner integral, respectively, one gets

$$\gamma_\sigma^e(\mathbf{r}') = -\int_0^T dt\delta\mathbf{e}^o(\mathbf{r}_i,t) \cdot \int_{-\infty}^{t} dt'\,\mathcal{G}(\mathbf{r}_i,t|\mathbf{r}',t') \cdot \mathbf{e}(\mathbf{r}',t'),$$

where the summation over i has been neglected. Because of the causility of the Green function,

$$\mathcal{G}(\mathbf{r},t|\mathbf{r}',t') \equiv 0, \quad t \le t',$$

the upper integration boundary of the inner integral can be changed from t to T, thus

$$\gamma^e_\sigma(\mathbf{r}') = -\int_0^T dt \int_{-\infty}^T dt' \delta\mathbf{e}^o(\mathbf{r}_i,t)\, \mathcal{G}(\mathbf{r}_i,t|\mathbf{r}',t') \cdot \mathbf{e}(\mathbf{r}',t'),$$

where $\delta\mathbf{e}^o(\mathbf{r}_i,t)$ could be brought into the inner integral, because it is zero for the time $t = -\infty$ to $t = 0$. This is also the reason why one can exchange the order of integration to

$$\gamma^e_\sigma(\mathbf{r}') = -\int_{-\infty}^T dt' \int_0^T dt \delta\mathbf{e}^o(\mathbf{r}_i,t)\, \mathcal{G}(\mathbf{r}_i,t|\mathbf{r}',t') \cdot \mathbf{e}(\mathbf{r}',t').$$

Again, due to the causality of $\mathcal{G}$, the inner integration from $t = 0$ to $t = t'$ vanishes, hence one can write

$$\gamma^e_\sigma(\mathbf{r}') = -\int_{-\infty}^T dt' \int_{t'}^T dt \delta\mathbf{e}^o(\mathbf{r}_i,t)\, \mathcal{G}(\mathbf{r}_i,t|\mathbf{r}',t') \cdot \mathbf{e}(\mathbf{r}',t'),$$

which leads to Equation (4.21).

A.5 Gradient specification for voltage type data

For the derivation of the gradients for voltage type data, one starts with Maxwell's Equations (4.17) for the perturbed state of the fields. These are differentiated with respect to time,

$$\begin{aligned} \sigma\frac{\partial}{\partial t}\delta\mathbf{e} - \nabla\times\frac{\partial}{\partial t}\delta\mathbf{h} &= -\delta\sigma\frac{\partial}{\partial t}\mathbf{e}, \\ \nabla\times\frac{\partial}{\partial t}\delta\mathbf{e} + \mu\frac{\partial^2}{\partial t^2}\delta\mathbf{h} &= -\delta\mu\frac{\partial^2}{\partial t^2}\mathbf{h}. \end{aligned}$$

Now a formal expression for the magnetic field time derivative is obtained from the time derivative form of Equation (4.4b),

$$\begin{aligned} \frac{\partial}{\partial t}\delta\mathbf{h}(\mathbf{r},t) &= \int_{V'}\int_0^t \mathcal{G}_{21}(\mathbf{r},t|\mathbf{r}',t') \cdot \frac{\partial}{\partial t'}\mathbf{e}(\mathbf{r}',t')\delta\sigma(\mathbf{r}')dt'd\mathbf{r}' \\ &+ \int_{V'}\int_0^t \frac{\mathcal{G}_{22}(\mathbf{r},t|\mathbf{r}',t')}{\mu(\mathbf{r}')} \cdot \frac{\partial^2}{\partial t'^2}\mathbf{h}(\mathbf{r}',t')\delta\mu(\mathbf{r}')dt'd\mathbf{r}'. \end{aligned} \tag{A.12}$$

Only conductivity variations are considered, hence the second term vanishes by setting $\delta\mu(\mathbf{r}')$ to zero. The time integration starts from time $t = 0$, because of the vanishing time derivative of the constant DC electric field before that time. In contrast to the non–causal electric fields, the magnetic field time derivative and thus the voltage is a causal field. In order to obtain the correct expression for the voltage, i.e. the negative of the magnetic induction time derivative, Equation (A.12) is scaled accordingly by the magnetic permeability of the model point where the voltages are sampled, thus

$$\delta\mathbf{v}(\mathbf{r},t) = \int_{V'}\int_0^t -\mu(\mathbf{r})\, \mathcal{G}_{21}(\mathbf{r},t|\mathbf{r}',t') \cdot \frac{\partial}{\partial t'}\mathbf{e}(\mathbf{r}',t')\delta\sigma(\mathbf{r}')dt'd\mathbf{r}'.$$

For better readability the volume integration shall now be omitted. An integration by parts yields

$$\begin{aligned} \delta\mathbf{v}(\mathbf{r},t) &= -\mu(\mathbf{r})\mathcal{G}_{21}(\mathbf{r},t|\mathbf{r}',t')\cdot\mathbf{e}(\mathbf{r}',t')\delta\sigma(\mathbf{r}')|_0^t \\ &+ \int_0^t \mu(\mathbf{r})\frac{\partial}{\partial t'}\mathcal{G}_{21}(\mathbf{r},t|\mathbf{r}',t')\cdot\mathbf{e}(\mathbf{r}',t')\delta\sigma(\mathbf{r}')dt'. \end{aligned}$$

Causality implies that the Green function of the first term becomes zero for the integration boundary t, thus

$$\begin{aligned} \delta\mathbf{v}(\mathbf{r},t) &= -\mu(\mathbf{r})\int_0^t \frac{\partial}{\partial t'}\mathcal{G}_{21}(\mathbf{r},t|\mathbf{r}',t')\cdot\mathbf{e}^{DC}(\mathbf{r}')\delta\sigma(\mathbf{r}')dt' \\ &+ \int_0^t \mu(\mathbf{r})\frac{\partial}{\partial t'}\mathcal{G}_{21}(\mathbf{r},t|\mathbf{r}',t')\cdot\mathbf{e}(\mathbf{r}',t')\delta\sigma(\mathbf{r}')dt' \\ &= \int_0^t \mu(\mathbf{r})\frac{\partial}{\partial t'}\mathcal{G}_{21}(\mathbf{r},t|\mathbf{r}',t')\cdot\{\mathbf{e}(\mathbf{r}',t')-\mathbf{e}^{DC}(\mathbf{r}')\}\delta\sigma(\mathbf{r}')dt'. \end{aligned}$$

Using the identity $\frac{\partial}{\partial t'}\mathcal{G}_{21} = -\frac{\partial}{\partial t}\mathcal{G}_{21}$ and inserting the volume integration again, it follows

$$\delta\mathbf{v}(\mathbf{r},t) = \int_{V'}\int_0^t -\mu(\mathbf{r})\frac{\partial}{\partial t}\mathcal{G}_{21}(\mathbf{r},t|\mathbf{r}',t')\cdot\{\mathbf{e}(\mathbf{r}',t')-\mathbf{e}^{DC}(\mathbf{r}')\}\delta\sigma(\mathbf{r}')dt'dr'. \tag{A.13}$$

Now a similar development as discussed in Section 4.3.1 for the electric field gradients can be made. From Equations (4.16) and (A.13), one can express the gradient for voltage data as

$$\begin{aligned} \gamma_\sigma^v(\mathbf{r}') &= \sum_i \int_0^T \delta\mathbf{v}^o(\mathbf{r}_i,t)\cdot\int_0^t \mu(\mathbf{r}_i)\frac{\partial}{\partial t}\mathcal{G}_{21}(\mathbf{r}_i,t|\mathbf{r}',t')\cdot\{\mathbf{e}(\mathbf{r}',t')-\mathbf{e}^{DC}(\mathbf{r}')\}dt'dt \\ &= \sum_i \int_0^T\int_{t'}^T \delta\mathbf{v}^o(\mathbf{r}_i,t)\mu(\mathbf{r}_i)\frac{\partial}{\partial t}\mathcal{G}_{21}(\mathbf{r}_i,t|\mathbf{r}',t')\cdot\{\mathbf{e}(\mathbf{r}',t')-\mathbf{e}^{DC}(\mathbf{r}')\}dtdt' \\ &= -\sum_i \int_0^T\int_{t'}^T \{\mathbf{e}(\mathbf{r}',t')-\mathbf{e}^{DC}(\mathbf{r}')\}\mathcal{G}_{12}^{+}(\mathbf{r}',t'|\mathbf{r}_i,t)\cdot\delta\mathbf{v}^o(\mathbf{r}_i,t)dtdt' \\ &= \int_0^T \{\mathbf{e}(\mathbf{r}',t')-\mathbf{e}^{DC}(\mathbf{r}')\}\cdot\sum_i\int_T^{t'} \mathcal{G}_{12}^{+}(\mathbf{r}',t'|\mathbf{r}_i,t)\cdot\delta\mathbf{v}^o(\mathbf{r}_i,t)dtdt' \\ &= \int_0^T \mathbf{e}(\mathbf{r}',t')\cdot\mathbf{e}_b(\mathbf{r}',t'|\delta\mathbf{v}^o)dt' - \mathbf{e}^{DC}(\mathbf{r}')\int_0^T \mathbf{e}_b(\mathbf{r}',t'|\delta\mathbf{v}^o)dt'. \end{aligned}$$

Note the application of the reciprocity relationship (4.12b) in this derivation. The backpropagated electric field arising from voltage data has previously been defined by Equation (4.26),

$$\mathbf{e}_b(\mathbf{r}',t'|\delta\mathbf{v}^o) = \sum_i\int_T^{t'} \mathcal{G}_{12}^{+}(\mathbf{r}',t'|\mathbf{r}_i,t)\cdot\delta\mathbf{v}^o(\mathbf{r}_i,t)dt.$$

Bibliography

Adhidjaja, J. I. and G. H. Hohmann, A finite-difference algorithm for the transient electromagnetic response of a three-dimensional body, *Geophys. J. Int.*, *98*, 233–242, 1989.

Alford, R. M., K. R. Kelly and D. M. Boore, Accuracy of finite–difference modeling of the acoustic wave equation, *Geophysics*, *39*, 834–841, 1974.

Alumbaugh, D. L., G. A. Newman, L. Prevost and J. N. Shadid, Three-dimensional wideband electromagnetic modeling on massively parallel computers, *Radio Science*, *31*, 1–23, 1996.

Anderson, W. L., Adaptive non–linear least–squares solution for constrained or unconstrained minimization problems (Subprogram NLSOL), Open–File Report 82–68, USGS, 1982.

Beauducel, F. and F. H. Cornet, Collection and three-dimensional modeling of GPS and tilt data at Merapi volcano, Java, *J. Geophys. Res.*, *104*, (B1), 725–736, 1999.

Berthommier, P., *Etude volcanologique du Merapi (Centre Java): Téphrostratigraphic et Chronologie – produits éruptifs*, Dissertation, Université Blaise Pascal, 1990.

Blohm, M., P. Hoekstra and R. Blohm, Utility and limitations of 1–D inversions of time–domain EM data over strong 2–D structures, in *61st Ann. Internat. Mtg. and Exp., Soc. Expl. Geophys., Expanded abstracts*, 410–411, 1991.

Boerner, D. E. and G. F. West, A spatial and spectral analysis of the electromagnetic sensitivity in a layered earth, *Geophys. J. Int.*, *98*, 11–21, 1989.

Camus, G., A. Gourgaud and P.-C. Mossand-Berthommier, Merapi (Central Java, Indonesia): An outline of the structural and magmatological evolution, with a special emphasis to the major pyroclastic events, *J. Volc. Geother. Res.*, *100*, 139–163, 2000.

Chave, A. D., The Fréchet Derivatives of Electromagnetic Induction, *J. Geophys. Res.*, *89*, 3373–3380, 1984.

Chen, J., A. Raiche, F. Sugeng and J. Macnae, Inversion of airborne electromagnetic data, in *68th Ann. Internat. Mtg, Soc. Expl. Geophys., Expanded Abstracts*, 756–759, SEG, 1998.

Claerbout, J. F., Toward a unified theory of reflector mapping, *Geophysics*, *36*, 467–481, 1971.

Commer, M., Ein spezielles Verfahren der eindimensionalen kombinierten Inversion von Long–Offset Transient Electromagnetic (LOTEM) – und Magnetotellurik (MT) – Daten, Diplomarbeit, Univ. zu Köln, Inst. für Geophys. und Meteo., February 1999.

Commer, M., S. L. Helwig and B. Tezkan, Untersuchungen zur Struktur des Vulkans Merapi (Zentral Java, Indonesien) mit transient elektromagnetischen Tiefensondierungen, Abschlussbericht für das DFG–Projekt MERAPI, Teilprojekt LOTEM HO 1506/8–1, Univ. zu Köln, Inst. für Geophys. und Meteo., 2003.

Constable, S. C., R. L. Parker and C. G. Constable, Occam's inversion: A practical algorithm for generating smooth models from electromagnetic sounding data, *Geophysics*, *52*, 289–300, 1987.

de Beer, J. H., C. L. le Roux, T. Hanstein and K. M. Strack, Direct current resistivity and LOTEM model for the deep structure of the northern edge of the Kaapvapl craton, South Africa, *Phys. Earth Planet. Inter.*, *66*, 51–61, 1991.

DeGroot-Hedlin, C. and S. C. Constable, Occam's inversion to generate smooth, two-dimensional models from magnetotelluric data, *Geophysics*, *55*, 1613–1624, 1990.

Dennis, J. E. and R. B. Schnabel, *Numerical Methods for Unconstrained Optimization and Nonlinear Equations*, Soc. Industrial appl. Math., Philadelphia, 1996.

DESERT Group, Multinational geoscientific research effort kicks off in the Middle East, *EOS*, *81*, 616–617, 2000.

Devaney, A. J., The limited–view problem in diffraction tomography, *Inverse Problems*, *5*, 510–523, 1989.

Dey, A. and H. F. Morrison, Resistivity modeling for arbitrarily shaped three–dimensional structures, *Geophysics*, *44*, 753–780, 1979.

Druskin, V. L. and L. A. Knizhnerman, A spectral semi-discrete method for the numerical solution of 3D-nonstationary problems in electrical prospecting, *Physics of the solid Earth*, *24*, 641–648, 1988.

Druskin, V. and L. Knizhnerman, Spectral approach to solving three–dimensional Maxwell's diffusion equations in the time and frequency domains, *Radio Science*, *29*, 937–953, 1994.

Druskin, V. L., L. A. Knizhnerman and P. Lee, New spectral Lanczos decomposition method for induction modeling in arbitrary 3–D geometry, *Geophysics*, *64*, 701–706, 1999.

DuFort, E. C. and S. P. Frankel, Stability conditions in the numerical treatment of parabolic differential equations, *Math. tables and other aids to comput. (former title of Math. Comput.), 7*, 135–152, 1953.

Eaton, P. A., 3D electromagnetic inversion using integral equations, *Geophys. Prospect., 37*, 407–426, 1989.

Eaton, P. A. and G. W. Hohmann, A rapid inversion technique for transient electromagnetic soundings, *Phys. Earth Planet. Inter., 53*, 384–404, 1989.

Edwards, R. N. and M. N. Nabighian, The Magnetometric Resistivity Method, in *Electromagentic Methods in Applied Geophysics*, edited by M. N. Nabighian, Vol. 2, 47–104, Soc. Expl. Geophys., 1991.

Ellis, R. G., Inversion of airborne electromagnetic data, in *68th Ann. Internat. Mtg, Soc. Expl. Geophys., Expanded Abstracts*, 2016–2019, SEG, 1998.

Ellis, R. G., Smooth 3D Inversion of Airborne Transient Electromagnetic Data using the TFQMR–FFT Fast Integral Equation Method, in *2nd International Symposium on Three-Dimensional Electromagnetics*, Salt Lake City, Utah, USA, 1999.

Farquarson, C. G. and D. W. Oldenburg, Inversion of time–domain electromagnetic data for a horizontally layered earth, *Geophys. J. Int., 114*, 433–442, 1993.

Felsen, L. B. and N. Marcuvitz, *Radiation and Scattering of Waves*, Prentice–Hall, Englewood Cliffs, N. J., 1973.

Fitterman, D. V. and M. T. Stewart, Transient electromagnetic sounding for groundwater, *Geophysics, 51*, 995–1005, 1986.

Fletcher, R. and C. M. Reeves, Function minimization by conjugate gradients, *Comp. J., 7*, 149–154, 1964.

Friedel, S., I. Brunner, F. Jacobs and C. Rücker, New results from DC resistivity imaging along the flanks of Merapi Volcano, in *Decade-Volcanoes under Investigation*, edited by J. Zschau and M. Westerhaus, Vol. IV/2000, 23–29, Dt. Geophys. Gesellschaft, 2000.

Frigo, M. and S. G. Johnson, FFTW: An adaptive software architecture for the FFT, in *1998 ICASSP conference proceedings*, 1381–1384, 1998.

Frischknecht, F. C., V. F. Labson, B. R. Spies and W. L. Anderson, Profiling Methods Using Small Sources, in *Electromagnetic Methods in Applied Geophysics*, edited by M. N. Nabighian, Vol. 2, Chapter 3, Soc. Expl. Geophys., 1991.

Fullagar, P. K. and D. W. Oldenburg, Inversion of horizontal loop electromagnetic soundings, *Geophysics, 49*, 150–164, 1984.

Gerstenecker, C., G. Läufer, B. Snitil and B. Wrobel, Digital elevation models for Mount Merapi, in *Decade-Volcanoes under Investigation*, edited by J. Zschau and M. Westerhaus, Vol. III/1998, 65–68, Dt. Geophys. Gesellschaft, 1998.

Goldman, M. M. and C. H. Stoyer, Finite–difference calculations of the transient field of an axially symmetric earth for vertical magnetic dipole excitation, *Geophysics*, *48*, 953–963, 1983.

Goldman, M., L. Tabarovsky and M. Rabinovich, On the influence of 3-D structures in the interpretation of transient electromagnetic sounding data, *Geophysics*, *59*, 889–901, 1994.

Grant, F. and G. F. West, *Interpretation theory in applied gepophysics*, McGraw-Hill, New York, 1965.

Haak, V., Das elektrische Abbild des Vulkans Merapi auf Java ermittelt durch das Meßverfahren Magnetotellurik, DFG Bericht, GFZ Potsdam, 1998.

Hanstein, T., Iterative und parametrisierte Dekonvolution für LOTEM Daten, in *Protokoll über das 14. Kolloquium Elektromagnetische Tiefenforschung*, edited by V. Haak and H. Rodemann, 163–172, Dt. Geophys. Gesellschaft, 1992.

Helwig, S. L., M. Goldman and A. Hördt, Multidimensional interpretation of TDEM data collected for mineral exploration in Israel, in *56th Ann. Int. Mtg. Eur. Assoc. explor. Geophys., Expanded Abstracts*, EAGE, Zeist, 1994.

Hestenes, M. R. and E. Stiefel, Methods of Conjugate Gradients for Solving Linear Systems, *J. Res. Nat. Bur. Standards*, *49*, 409–436, 1952.

Hoffmann-Rothe, A., A. Müller, O. Ritter and V. Haak, Magnetotelluric survey at Merapi Volcano and across Java, Indonesia, in *Decade-Volcanoes under Investigation*, edited by J. Zschau and M. Westerhaus, Vol. III/1998, 47–52, Dt. Geophys. Gesellschaft, 1998.

Hohmann, G. W., Numerical modeling for electromagnetic methods of geophysics, in *Electromagnetic Methods in Applied Geophysics*, edited by M. N. Nabighian, Vol. 1, Chapter 5, 313–363, Soc. Expl. Geophys., 1988.

Hördt, A., Ein Verfahren zur 'Joint Inversion' angewandt auf 'Long Offset Electromagnetics' (LOTEM) und Magnetotellurik (MT), Diplomarbeit, Univ. zu Köln, Inst. für Geophys. und Meteo., 1989.

Hördt, A., *Interpretation transient elektromagnetischer Tiefensondierungen für anisotrop horizontal geschichtete und für dreidimensionale Leitfähigkeitsstrukturen*, Dissertation, Univ. zu Köln, Inst. für Geophys. und Meteo., 1992.

Hördt, A., Calculation of electromagnetic sensitivities in the time domain, *Geophys. J. Int.*, *133*, 713–720, 1998.

Hördt, A. and M. Müller, Understanding LOTEM data from mountainous terrain, *Geophysics*, *65*, 1113–1123, 2000.

Hördt, A., V. L. Druskin and L. A. Knizhnerman, Interpretation of 3-D effects on long-offset transient electromagnetic (LOTEM) soundings in the Münsterland area/Germany, *Geophysics*, *57*, 1127–1137, 1992.

Hördt, A., P. Andrieux, F. M. Neubauer, H. Rüter and K. Vozoff, A first attempt at monitoring underground gas storage by means of time-lapse multichannel transient electromagnetics, *Geophys. Prospect.*, *48*, 489–509, 2000*a*.

Hördt, A., S. Dautel, B. Tezkan and H. Thern, Interpretation of long-offset transient electromagnetic data from the Odenwald area, Germany, using two-dimensional modelling, *Geophys. J. Int.*, *140*, 577–586, 2000*b*.

Huang, H. and G. J. Palacky, Damped least–squares inversion of time–domain airborne EM data based on singular value decomposition, *Geophys. Prospect.*, *39*, 827–844, 1991.

Hutchinson, S. A., J. N. Shadid and R. S. Tuminaro, Aztec User's Guide: Version 1.1, Technical Report, SAND95-1559, Sandia National Laboratories, NM, USA, 1995.

Jackson, D. D., Interpretation of inaccurate, insufficient and inconsistent data, *Geophys. J. R. astr. Soc.*, *28*, 97–109, 1972.

Jackson, J. D., *Classical Electrodynamics*, John Wiley & Sons, Inc., 2. Auflage, 1975.

Jones, A. G. and I. Dumas, Electromagnetic images of a volcanic zone, *Phys. Earth Planet. Inter.*, *81*, 289–314, 1993.

Jupp, D. L. B. and K. Vozoff, Stable iterative methods for the inversion of geophysical data, *Geophys. J. R. astr. Soc.*, *42*, 957–976, 1975.

Kalscheuer, T., Die zweidimensionale Interpretation der LOTEM (Long Offset Transient Electromagnetics)-Daten vom Südhang des Vulkans Merapi in Indonesien (in Vorbereitung), Diplomarbeit, Univ. zu Köln, Inst. für Geophys. und Meteo., 2003.

Kauahikaua, J., D. B. Jackson and C. J. Zablocki, Resistivity structure to a depth of 5 km benaeth Kilauea volcano, Hawaii from large-loop-source electromagnetic measurements (0.004–8 Hz), *J. Geophys. Res.*, *91*, 8267–8283, 1986.

Koch, O., Transient–elektromagnetische Messungen zur Erkundung einer Leitfähigkeitsanomalie am Vulkan Merapi in Indonesien, Diplomarbeit, Univ. zu Köln, Inst. für Geophys. und Meteo., 2003.

Kriegshäuser, B., Einige Aspekte der 3D Interpretation von LOTEM Daten, Diplomarbeit, Univ. zu Köln, Inst. für Geophys. und Meteo., December 1991.

Lanczos, C., Linear Systems in self–adjoint form, *Am. math. Monthly*, *65*, 665–679, 1958.

Lee, K. H. and G. Xie, A new approach to imaging with low–frequency electromagnetic fields, *Geophysics*, *58*, 780–796, 1993.

Lénat, J. F., Geoelectrical methods in volcano monitoring, in *Monitoring active volcanoes*, edited by B. McGuire, C. Kilburn, and J. Murray, 248–274, UCL Press, 1995.

Levenberg, K., A method for the solution of certain nonlinear problems in least squares, *Quarterly of Applied Mathematics*, *2*, 164–168, 1944.

Lienert, B. R., An electromagnetic study of Maui's last active volcano, *Geophysics*, *56*, 972–982, 1991.

Lines, L. R. and S. Treitel, Tutorial: A review of least-squares inversion and its application to geophysical problems, *Geophys. Prospect.*, *32*, 159–186, 1984.

Loewenthal, D., L. Lu, R. Robertson and J. W. C. Sherwood, The wave equation applied to migration, *Geophys. Prospect.*, *24*, 380–399, 1976.

Lu, X., M. J. Unsworth and J. Booker, Rapid relaxation inversion of CSAMT data, *Geophys. J. Int.*, *138*, 381–392, 1999.

Mackie, R. L. and T. R. Madden, Three-dimensional magnetotelluric inversion using conjugate gradients, *Geophys. J. Int.*, *115*, 215–229, 1993.

Macnae, J. C., Survey design for multicomponent electromagnetic systems, *Geophysics*, *49*, 265–273, 1984.

Macnae, J. and Y. Lamontagne, Imaging quasi–layered conductive structures by simple processing of transient electromagnetic data, *Geophysics*, *52*, 545–554, 1987.

Madden, R. and R. L. Mackie, Three-Dimensional Magnetotelluric Modeling and Inversion, *Proceedings of the IEEE*, *77*, 318–333, 1989.

Marquardt, D. W., An algorithm for least-squares estimation of non-linear parameters, *SIAM J.*, *11*, 431–441, 1963.

Matthes, S., *Mineralogie*, Springer, Berlin, 1990.

McGillivray, P. R. and D. W. Oldenburg, Methods for calculating Fréchet derivatives and sensitivities for the non-linear inverse problem: A comparative study, *Geophys. Prospect.*, *38*, 499–524, 1990.

McGillivray, P. R. et al., Calculating of sensitivities for the frequency-domain electromagnetic problem, *Geophys. J. Int.*, *116*, 1–4, 1994.

Meister, A., *Numerik linearer Gleichungssysteme - Eine Einführung in moderne Verfahren*, Vieweg, Braunschweig/Wiesbaden, 1999.

Meju, M. A., *Geophysical Data Analysis: Understanding Inverse Problem Theory and Practice*, 6, Society of Exploration Geophysicists, Tulsa, 1994.

Militzer, H. and F. Weber, *Angewandte Geophysik*, Vol. 1, Springer, 1984.

Mills, T., P. Hoekstra, M. Blohm and L. Evans, Time domain electromagnetic soundings for mapping sea–water intrusion in Monterey County, California, *Groundwater*, *26*, 771–782, 1988.

Mitsuhata, Y., T. Uchida and H. Amano, 2.5-D inversion of frequency–domain electromagnetic data generated by a grounded–wire source, *Geophysics*, *67*, 1753–1768, 2002.

Moskow, S., V. Druskin, T. Habashy, P. Lee and S. Davydychewa, A finite difference scheme for elliptic equations with rough coefficients using a cartesian grid nonconforming to interfaces, *SIAM J. Numerical Analysis*, *36*, 442–464, 1999.

Müller, A., Identification of good electric conductors below Merapi Volcano (Central Java) by magnetotellurics, in *DGG–Mitteilungen, Sonderband*, Vol. Addendum to IV/2000, Dt. Geophys. Gesellschaft, 2000*a*.

Müller, M., *Elektromagnetik an Vulkanen*, Dissertation, Univ. zu Köln, Inst. für Geophys. und Meteo., 2000*b*.

Müller, M., A. Hördt and F. M. Neubauer, Internal structure of Mount Merapi, Indonesia, derived from long–offset transient electromagnetic data, *J. Geophys. Res.*, *107*, ECV 2–1 – ECV 2–14, 2002.

Nabighian, M. N. and J. C. Macnae, Time Domain Electromagnetic Prospecting Methods, in *Electromagnetic Methods in Applied Geophysics*, edited by M. N. Nabighian, Vol. 2, Chapter 6, Soc. Expl. Geophys., 1991.

Nekut, A. G., Direct inversion of time–domain electromagnetic data, *Geophysics*, *52*, 1431–1435, 1987.

Newhall, C. G., S. Bronto, B. Alloway, N. G. Banks, I. Bahar and M. A. D. Marmol, 10000 years of explosive eruptions of Merapi Volcano, Central Java: Archaeological and modern implications, *J. Volc. Geother. Res.*, *100*, 9–50, 2000.

Newman, G. A., Deep transient electromagnetic soundings with a grounded source over near-surface conductors, *Geophys. J. Int.*, *98*, 587–601, 1989.

Newman, G., Crosswell electromagnetic inversion using integral and differential equations, *Geophysics*, *60*, 899–911, 1995.

Newman, G. and D. L. Alumbaugh, Three–dimensional massively parallel electromagnetic inversion – I. Theory, *Geophys. J. Int.*, *128*, 345–354, 1997.

Newman, G. A. and D. L. Alumbaugh, Three–dimensional magnetotelluric inversion using non–linear conjugate gradients, *Geophys. J. Int.*, *140*, 410–424, 2000.

Newman, G. A. and G. M. Hoversten, Solution strategies for two- and three-dimensional electromagnetic inverse problems, *Inverse Problems*, *16*, 1357–1375, 2000.

Newman, G. A., G. W. Hohmann and W. L. Anderson, Transient electromagnetic response of a three-dimensional body in a layered earth, *Geophysics*, *51*, 1608–1627, 1986.

Newman, G. A., W. L. Anderson and G. W. Hohmann, Interpretation of transient electromagnetic soundings over three–dimensional structure for the central–loop configuration, *Geophys. J. R. astr. Soc.*, *89*, 889–914, 1987.

Oristaglio, M. L. and G. W. Hohmann, Diffusion of electromagnetic fields into a two-dimensional earth: A finite-difference approach, *Geophysics*, *49*, 870–894, 1984.

Palacky, G. J., Tutorial: Research, application and publications in electrical and electromagnetic methods, *Geophys. Prospect.*, *31*, 861–872, 1983.

Pellerin, L. and D. L. Alumbaugh, Tools for electromagnetic investigation of the shallow subsurface, *The Leading Edge*, *16*, 1631–1638, 1997.

Pellerin, L. and G. W. Hohmann, Three–Dimensional Inversion of Electromagnetic Data, in *63rd Ann. Internat. Mtg., Soc. Expl. Geophys., Expanded abstracts*, 360–363, Salt Lake City, Utah, 1993.

Petrat, L., Zweidimensionale Inversion von Long Offset Transient Electromagnetics-Daten, Diplomarbeit, Univ. zu Köln, Inst. für Geophys. und Meteo., January 1996.

Petry, H., Transient elektromagnetische Tiefensondierungen — Modellrechnungen und Inversion, Diplomarbeit, Univ. zu Köln, Inst. für Geophys. und Meteo., 1987.

Polyak, E. and G. Ribière, Note sur la convergence des méthods conjugées, *Rev. Fr. Inr. Rech. Oper.*, *16*, 35–43, 1969.

Press, W. H., W. T. Vetterling, S. A. Teukolsy and B. Flannery, *Numerical Recipes in Fortran*, Cambridge University Press, 1992.

Raiche, A. P., D. L. B. Jupp, H. Rutter and K. Vozoff, The joint use of coincident loop transient electromagnetic and Schlumberger sounding to layered structures, *Geophysics*, *50*, 1618–1627, 1985.

Ratdomopurbo, A. and G. Poupinet, Monitoring a temporal change of seismic velocity in a volcano: application to the 1992 eruption of Mt. Merapi (Indonesia), *Geophys. Res. Lett.*, *22*, 775–778, 1995.

Rebscher, D., M. Westerhaus, A. Körner, W. Welle, Subandriyo, A. Brodscholl, H.-J. Kümpel and J. Zschau, Indonesian–German Multiparameter Stations at Merapi Volcano, in *Decade-Volcanoes under Investigation*, edited by B. Buttkus, S. Greinwald, and J. Ostwald, Vol. IV/2000, 93–102, Dt. Geophys. Gesellschaft, 2000.

Richtmeyr, R. D. and K. W. Morton, *Difference methods for initial value problems*, Methods in Geochemistry and Geophysics, Bd. 30, John Wiley and Sons, New York, 1967.

Ritter, O., A. Hoffmann-Rothe, A. Müller, S. Dwipa, E. M. Arsadi, A. Mahfi, I. Nurnusanto, S. Byrdina, F. Echternacht and V. Haak, A magnetotelluric profile across Central Java, Indonesia, *Geophys. Res. Lett.*, *25*, 4265–4268, 1998.

Rodi, W. and R. L. Mackie, Nonlinear conjugate gradients algorithm for 2-D magnetotelluric inversion, *Geophysics*, *66*, 174–187, 2001.

Ryan, M. P., Elasticity and contractancy of Hawaiian olivine tholeiite and its role in the stability and structural evolution of subcaldera magma reservoirs and rift systems, in *US Geological Survey Professional Paper 1350, Volcanism in Hawaii*, edited by R. W. Decker, T. L. Wright, and P. H. Stauffer, 1395–1447, Washington DC, US Government Printing Office, 1987.

Sarma, D. G., V. M. Maru and G. Varadarajan, An improved pulse transient airborne electromagnetic system for locating good conductors, *Geophysics*, *41*, 287–299, 1976.

Schneider, T., Zeitlich optimierte Sensitivitätsberechnung für Long-Offset Transient Electromagnetics (LOTEM) unter Verwendung des Reziprozitätgesetzes, Diplomarbeit, Univ. zu Köln, Inst. für Geophys. und Meteo., 2000.

Scholl, C., Die Periodizität von Sendesignalen bei Long-Offset Transient Electromagnetics, Diplomarbeit, Univ. zu Köln, Inst. für Geophys. und Meteo., 2001.

Scholl, C., M. Commer, S. L. Helwig and R. Martin, LOTEM 3D Inversionen auf kleinen Linux–Clustern, in *62. Jahrestagung der Dt. Geophysik. Gesellsch. (Hannover), Tagungsband*, 45–46, Dt. Geophys. Gesellschaft, 2002.

Setiawan, A., *Modeling of Gravity Changes on Merapi Volcano Observed Between 1997–2000*, Dissertation, Tech. Univ. Darmstadt, 2002.

Shewchuk, J. R., An Introduction to the Conjugate Gradient Method Without the Agonizing Pain, Tutorial, School of Computer Science, Carnegie Mellon Univ., Pittsburgh, 1994.

Siswowidjoyo, S., I. Suryo and I. Yokoyama, Magma eruption rates of Merapi volcano, Central Java, Indonesia, during one century (1890–1992), *Bull. Volcanol.*, *57*, 111–116, 1995.

Skjellum, A., N. E. Doss and P. V. Bangalore, Writing libraries in MPI, in *Proceedings of the Scalable Parallel Libraries Conference*, edited by A. Skjellum and D. Reese, 166–173, IEEE Comput. Sci. Press, 1993.

Smith, J. T., Conservative modeling of 3-D electromagnetic fields, Part II: Biconjugate gradient solution and an accelerator, *Geophysics*, *61*, 1319–1324, 1996.

Spies, B. R., Recent developments in the use of surface electical methods for oil and gas exploration in the Soviet Union, *Geophysics*, *48*, 1102–1112, 1983.

Spies, B. R. and F. C. Frischknecht, Electromagnetic Sounding, in *Electromagentic Methods in Applied Geophysics*, edited by M. N. Nabighian, Vol. 2, Chapter 5, Soc. Expl. Geophys., 1991.

Spitzer, K. and B. Wurmstich, Speed and Accuracy in 3-D Resistivity Modeling, in *Three–Dimensional Electromagnetics*, edited by M. Oristaglio, 161–176, Soc. Explor. Geophys., 1999.

Stahl, U., Horizontale Magnetfeldkomponenten und Magnetfeldsensoren der long-offset transient electromagnetics (LOTEM)-Methode, Diplomarbeit, University of Cologne, 1999.

Stewart, M. T., Evaluation of electromagnetic methods for rapid mapping of salt–water interfaces in coastal aquifers, *Groundwater*, *20*, 538–545, 1982.

Strack, K. M., *Exploration with Deep Transient Electromagnetics*, Elsevier, Amsterdam, 1992.

Strack, K. M., T. Hanstein, K. LeBrocq, D. C. Moss and K. Vozoff, Case histories of long–offset transient electromagnetics (LOTEM) in hydrocarbon prospective areas, *First Break*, *7*, 467–477, 1989.

Supriadi, S., D. Sutarno, L. Hendrajaya and D. Santoso, Controlled–source audiomagnetotellurics (CSAMT) surveys at Merapi volcano, in *DGG–Mitteilungen*, Dt. Geophys. Gesellschaft, 2000.

Tabarovsky, L. A. and M. B. Rabinovich, Mathematical modeling of transient electromagnetic fields in quasi–three–dimensional models, VINITI, N6264–B88 (in Russian), 1988.

Tarantola, A., Inversion of seismic reflection data in the acoustic approximation, *Geophysics*, *49*, 1259–1266, 1984.

Taylor, K., M. Widmer and M. Chesley, Use of transient electromagnetic to define local hydrogeology in an arid alluvial environment, *Geophysics*, *57*, 343–352, 1992.

Tezkan, B., Effects of a pipeline on LOTEM measurements: Summary of pipeline modeling, Internal report, Univ. zu Köln, Inst. für Geophys. und Meteo., 1993.

Thern, H., T. Hanstein and A. Hördt, LOTEM im Odenwald – auch hier ein Krustenleiter?, in *Protokoll über das 16. Kolloquium Elektromagnetische Tiefenforschung*, edited by K. Bahr and A. Junge, 341–350, Dt. Geophys. Gesellschaft, 1996.

Tikhonov, A. N. and V. Y. Arsenin, *Solutions of Ill-posed Problems*, Wiley, New York, 1977.

Torres-Verdin, C. and T. M. Habashy, Rapid 2.5-dimensional forward modeling and inversion via a new nonlinear scattering approximation, *Radio Science*, *29*, 1051–1079, 1994.

Unsworth, M. and D. Oldenburg, Subspace inversion of electromagnetic data: application to mid-ocean-ridge exploration, *Geophys. J. Int.*, *123*, 161–168, 1995.

Unsworth, M. J., X. Lu and M. D. Watts, CSAMT exploration at Sellafield: Characterization of potential radioactive waste disposal site, *Geophysics*, *65*, 1070–1079, 2000.

Vozoff, K. and D. L. B. Jupp, Joint Inversion of Geophysical Data, *Geophys. J. R. astr. Soc.*, *42*, 977–991, 1975.

Wang, T. and G. W. Hohmann, A finite-difference, time-domain solution for three-dimensional electromagnetic modeling, *Geophysics*, *58*, 797–809, 1993.

Wang, T., M. Oristaglio, A. Tripp and G. Hohmann, Inversion of diffusive transient elctromagnetic data by a conjugate–gradient method, *Radio Science*, *29*, 1143–1156, 1994.

Ward, S. H. and G. W. Hohmann, Electromagnetic theory for geophysical applications, in *Electromagnetic methods in applied geophysics*, edited by M. N. Nabighian, Vol. 1, Chapter 4, 131–311, Soc. Expl. Geophys., 1988.

Wassermann, J., M. Ohrnberger, F. Scherbaum et al., Continuous measurements at Merapi Volcano (Java, Indonesia) using a network of small-scale seismograph arrays, in *Decade-Volcanoes under Investigation*, edited by J. Zschau and M. Westerhaus, Vol. III/1998, 81–82, Dt. Geophys. Gesellschaft, 1998.

Westerhaus, M., D. Rebscher, W. Welle, A. Pfaff, A. Körner and M. Nandaka, Deformation measurements at the flanks of Merapi Volcano, in *Decade-Volcanoes under Investigation*, edited by J. Zschau and M. Westerhaus, Vol. III/1998, 93–100, Dt. Geophys. Gesellschaft, 1998.

Xie, G. and J. Li, A new algorithm for 3-D nonlinear electromagnetic inversion, in *Three-dimensional electromagnetics*, edited by M. Oristaglio, B. Spies, and M. R. Cooper, 193–207, SEG, 1999.

Yee, K. S., Numerical solution of initial boundary problems involving Maxwell's equations in isotropic media, *IEEE Trans. Ant. Prop.*, *AP–14,* 302–309, 1966.

Zhadanov, M. S., V. U. Matusevich and M. A. Frenkel, *Seismic and Electromagnetic Migration (in Russian)*, Nauka, Moscow, 1988.

Zhdanov, M. S. and M. A. Frenkel, The solution of inverse problems on the basis of the analytical continuation of the transient electromagnetic fields in the reverse time, *J. Geomagn. Geoelectr.*, *35*, 747–765, 1983.

Zhdanov, M. S. and O. Portniaguine, Time–domain electromagnetic migration in the solution of inverse problems, *Geophys. J. Int.*, *131*, 293–309, 1997.

Zhdanov, M. S., D. A. Pavlov and R. G. Ellis, Localized S–inversion of time-domain electromagnetic data, *Geophysics*, *67*, 1115–1125, 2002.

Zimmer, M. and J. Erzinger, Geochemical monitoring on Merapi Volcano, Indonesia, in *Decade-Volcanoes under Investigation*, edited by J. Zschau and M. Westerhaus, Vol. III/1998, 89–92, Dt. Geophys. Gesellschaft, 1998.

Zschau, J., R. Sukhyar, M. A. Purbawinata, B. Lühr and M. Westerhaus, Project MERAPI — Interdisciplinary Research at a High-Risk Volcano, in *Decade-Volcanoes under Investigation*, edited by J. Zschau and M. Westerhaus, Vol. III, 3–8, Dt. Geophys. Gesellschaft, 1998.

Acknowledgments

The author would like to thank Prof. Bülent Tezkan and Priv. Doz. Andreas Hördt for being the doctoral thesis supervisor and providing advice and support during the whole time of this work. Also many thanks to Prof. Klaus Spitzer for appraising this thesis. Valuable additional assistance was given by Prof. Fritz M. Neubauer and Stefan Helwig.

The author is especially grateful to Gregory A. Newman for a highly productive cooperation during his several visits at the University of Cologne. Despite a variety of tough theoretical and numerical obstacles to be overcome, the teamwork on the large–scale inversion project was always a pleasure. A deeper understanding of many related subjects such as large–scale optimization could be gained during countless blackboard discussions. After all, the project has shown that ‘no pain no gain’ (*Newman*, pers. comm.) holds.

Part of this work was carried out during an internship at the Geophysical Technology Department, Sandia National Laboratories (New Mexico, USA), following the invitation of Marianne C. Walck and Gregory A. Newman. Sandia is a multi–program laboratory operated by the Sandia Corporation, a Lockheed Martin Company, for the United States Department of Energy under Contract DE–AC04–94AL85000. Financial support during the internship was provided by a short–term scholarship granted by the German Academic Exchange Service (DAAD). Again thanks to Gregory A. Newman and especially his wife Susan Wells for helping to get to know the New Mexican way of life.

The author gratefully acknowledges funding of the surveys at Merapi by the German Science Foundation (DFG) through the research programme ’LOTEM at Merapi’ (project HO1506/8-1). The field work was undertaken with the help of Stefan Helwig, Tilman Hanstein, Andreas Hördt, Carsten Scholl, Roland Blaschek, Olaf Koch, Roland Martin and Jörn Lange from the University of Cologne and many students from the Institut Teknologi Bandung (ITB). Continuous support during survey organization was given by Arnold Brodscholl (Volcanological Technology Research Center, Yogyakarta), Supriadi (University of Semarang), Prof. L. Hendrajaya (ITB), D. Sutarno (ITB) and Umar Fauzi (ITB).

The Regional Computing Centre of the University of Cologne (RRZK) supplied much of the computing time. Personal technical advice during usage of the parallel computers was given by Volker Winkelmann (RRZK).

The author expresses his gratitude to Andreas Hördt, Stefan Helwig, Annika Steuer, Carsten Scholl, Tim Seher and Cathrin Klitzsch for their critical reviews, which improved the manuscript. The folks of the Aussenstelle Explorationsgeophysik always guaranteed a refreshing working atmosphere. The friends and roommates Walter Heibey and Jörg von Oertzen were more than helpful during the work.

At last, thanks to Ursula Commer for all support. In the hope that he is able to receive this message, sincere thanks to Hans Commer.

Ich versichere, dass ich die von mir vorgelegte Dissertation selbständig angefertigt, die benutzten Quellen und Hilfsmittel vollständig angegeben und die Stellen der Arbeit - einschließlich Abbildungen und Tabellen -, die anderen Werken im Wortlaut oder dem Sinn nach entnommen sind, in jedem Einzelfall als Entlehnung kenntlich gemacht habe; dass diese Dissertation noch keiner anderen Fakultät oder Universität zur Prüfung vorgelegen hat; dass sie - abgesehen von unten angegebenen Teilpublikationen - noch nicht veröffentlicht worden ist sowie, dass ich eine solche Veröffentlichung vor Abschluß des Promotionsverfahrens nicht vornehmen werde. Die Bestimmungen dieser Promotionsordnung sind mir bekannt. Die von mir vorgelegte Dissertation ist von Prof. B. Tezkan betreut worden.

Köln, September 2003

Teilpublikationen

1. **Commer, M., A. Hördt and S. L. Helwig**, 3–D inversion of LOTEM data under strong boundary conditions, in *Protokoll über das 19. Kolloquium elektromagnetische Tiefensondierung*, herausgegeben von A. Hördt und J. B. Stoll, Dt. Geophys. Gesellsch., 2001.

2. **Commer, M., S. L. Helwig, A. Hördt, C. Scholl and B. Tezkan**, Three–dimensional constrained inversion of LOTEM data from Mount Merapi, Indonesia, including topography, *submitted to Geophysics*, 2003.

3. **Commer, M. and G. A. Newman**, A parallel finite–difference approach for three–dimensional transient electromagnetic modeling with non–causal sources, *submitted to Geophysics*, 2003.

4. **Commer, M., S. L. Helwig and B. Tezkan**, Untersuchungen zur Struktur des Vulkans Merapi (Zentral Java, Indonesien) mit transient elektromagnetischen Tiefensondierungen, Abschlussbericht für das DFG–Projekt MERAPI, Teilprojekt LOTEM HO 1506/8–1, Universität zu Köln, Inst. f. Geophys. u. Meteo., 2003.

5. **Newman, G. A. and M. Commer**, Three dimensional transient electromagnetic inversion: Problem formulation and method of solution, *submitted to Geophys. J. Int.*, 2003.